Analyse et modélisation de transformations de phase par précipitation dans des alliages de magnésium modèles.

Viktor Kopp

Université de Rouen

U.F.R. des Science et Technique

Ecole doctorale "SPMII"

THÈSE

Discipline: Physique

Specialité: Science des Matériaux

Présenté par

Viktor S. KOPP

Pour l'obtention du grade de

DOCTEUR DE L'UNIVESITÉ DE ROUEN

Le 2 décembre 2010

Analyse et modélisation de transformations de phase par précipitation dans des alliages de magnésium modèles.

Directeur de thèse: *Didier BLAVETTE*

Encadrants: *Williams LEFEBVRE*

Cristelle PAREIGE

Membres du jury:

Mme. Charlotte Sylvie Becquart	Professeur des Universités	President
Mme. Patricia Donnadieu	Directeur de recherche CNRS	Rapporteur
M. Michel Perez	Professeur des Universités	Rapporteur
M. Didier Blavette	Professeur des Universités	
Mme. Cristelle Pareige	Maître de conférences	
M. Williams Lefebvre	Maître de conférences	

Resumé

La cinétique des premiers stades de précipitation dans les alliages Mg-RE a été étudiée par sonde atomique tomographique et par Microscopie électronique en transmission. La formation et la croissance des précipités β'' ordonnés et cohérents, depuis la solution solide HCP a été étudiée à 150°C pour l'alliage binaire Mg-2.6%pds Nd et pour l'alliage ternaire Mg-2.6%pds Y-2.7%pds Nd.

Dans l'alliage binaire, les précipités β'' forment des disques prismatiques de plan d'habitat $\{10\bar{1}0\}$. Leur croissance a lieu dans les directions [0001] et $[11\bar{2}0]$, leur épaisseur n'évoluant pas de façon significative.

L'étude de la cinétique dans l'alliage ternaire a montré que l'ajout d'yttrium ralentit fortement la cinétique. Seuls des amas de solutés riches aplatis ont été observés aux temps très longs.

Ce travail de thèse contribue également à la détermination du diagramme de phase Mg-Nd en précisant la solubilité à haute température du Nd dans Mg.

En parallèle aux études expérimentales, des simulations de la cinétique de formation de la phase $D0_{19}$ à partir d'une solution solide HCP ont été réalisées dans un alliage A-5.5%at B grâce à la méthode Monte-Carlo cinétique. Nous nous sommes focalisés sur l'influence de la mobilité atomique sur le chemin cinétique. Cette mobilité est contrôlée par le paramètre d'asymétrie u. Il a été montré que u n'influence que l'ordre à courte distance dans les premières sphères de coordination pendant les tout premiers stades de décomposition. La cinétique globale est indépendante de la valeur de u. La coalescence des prècipitès $D0_{19}$ se produit par un mècanisme d'èvaporation-condensation quel que soit la valeur de u, et est décrite par la loi de coalescence de Lifshitz-Slyozov-Wagner.

Abstract

Kinetics of first stages of precipitation in Mg-RE alloys have been studied by means of Atom Probe and by Transmission electron microscopy techniques. Formation and development of ordered coherent β''-precipitates from the HCP solid solution of a binary Mg-2.6Nd and a ternary Mg-2.6Y-2.7Nd (wt.%) alloys were investigated at 150°C.

In the binary alloy, the β''-precipitates form as plates on the prismatic planes. They grow in and directions, whereas the thickening of plates is insignificant or absent.

Investigation of the ternary alloy showed that additions of Yttrium significantly slow down the kinetics. Only plate-like solute-rich atomic heterogeneities were observed at long aging times.

The present work also makes a contribution to the determination of the binary Mg-Nd diagram ascertaining the high temperature solubility of Nd in Mg.

In parallel, simulation of the kinetics of the formation of the $D0_{19}$ phase from the hcp solid solution has been undertaken in A-5.5%at B by Atomistic Kinetic Monte-Carlo method. Main attention has been paid to the investigation of the influence of the atom-vacancy mobility, controlled by the asymmetry parameter u, on the kinetic pathways. It was shown that u only influences short range ordering in the first shell during the very early stages. Overall kinetics is independent on the value of u. Coarsening of $D0_{19}$ precipitates proceeds by the evaporation-condensation mechanism whatever the value of u. The mean precipitate size increases according to the Lifshitz-Slyozov-Wagner law.

Acknowledgements

First of all, I would like to express my gratitude to M. Didier Blavette, Professeur des Universités, director of the laboratory "Groupe de Physique des Materiaux" (GPM), for these three years which I spent in the laboratory under his supervision.

I am heartily thankful to my supervisors, M. Williams Lefebvre and Mme. Cristelle Pareige, Maitres de Conférences à l'Université de Rouen, for accepting the guidance over me and, whose encouragement and support from the initial to the final level enabled me to develop an understanding of the subject. I would like to express my special thanks to M. Williams Lefebvre for taking time out from his busy schedule to help me with some organization questions and in communication with state institutions.

I would like to thank the President of the jury Mme. Charlotte Sylvie Becquart, Professeur des Universités à l'École Nationale Supérieure de Chimie de Lille, and the referees M. Michel Perez, Professeur des Université à Insa de Lyon and Mme. Patricia Donnadieu, Directeur de recherche CNRS, who kindly accepted the proposition to examine this work.

Appreciation also goes out to Centre de Ressources Informatiques de Haute-Normandie (CRIHAN) for the computer facilities and technical assistance throughout my graduate program. I recognize that this research would not have been possible without the financial and organizational assistance of the University of Rouen and L'École doctorale "SPMII". Thus, I express my gratitude to these organizations.

A big part of this work would not be possible without a help of Béatrice Foulon, Charly Vaudolon, Sylvain Chambreland and Cécile Genevois. I need to express them my gratitude for their assistance they provided for different types of specimen preparations during my research project.

I must also acknowledge Mme. Helena Zapolsky, Professeur des Universités, for her support, scientific advises and suggestions.

I owe my deepest gratitude to the laboratory office staff, in particular to Agnès Dalle, Christine Mion, Caroline Jorry, Germain Martigny and Romain Vincent for their goodwill and all the instances in which their assistance helped me along the way.

I am indebted to many of my colleagues and friends for supporting me during this period of my life, namely Leonid B., Nicolas M., Julien B., Marilyne C., Audrey C., Anouar B., Malin T., Mathieu G., Johan A., Jussef R., Ali A., Abdelahad C., Evrard B.-E., Baishakhi M., Bonta S.R., Megha D., Maria G., Adeline M., Manuel R., Thomas P. and all others. Here, of course, I do not forget my Ukrainian colleagues who worked with me in the lab and

supported me outside it: Iryna, Lena, Slava and Sergiy Mykhailovytch. Thank you for our philosophical debates, exchanges of knowledge, skills, and venting of frustration during my study, which helped enrich the experience.

I would like, of course, to thank my mother and stepfather for the support they provided me through my entire life.

Especially, I must acknowledge Jane S. without whose support, encouragement and care (though over a distance), I would not have finished this thesis.

A very special thanks goes out to Valentin Kostin, my school teacher, without whose motivation and encouragement I would not, probably, have considered a career in physical research.

Lastly, I offer my regards and blessings to all of those who supported me in any respect during the completion of the project.

Contents

Introduction

Limiting the emission of green house gases as well as the reduction of fuel consumption are urgent topics that need to be solved in the near future especially in transportation industries. Besides more efficient processes and smart design, the use of light weight materials is one way to address these problems. Despite the fact that there is always a competition among various material groups such as light metals, steels and polymers for a use in relevant light-weight structures depending on economical aspects, materials and component requirements, magnesium still offers a promising potential. With regard to their intrinsic characteristics like low density, high specific strength, good machinability, high recyclability and availability, magnesium found more implementations in relevant applications.

The production of cast Mg-alloys under high pressure controlled atmosphere is well established and the main research activities aim now at improving the mechanical properties of Mg-alloys for applications up to 250–300°C, with a particular attention to the creep behavior at those temperatures. As a consequence, an intense activity is focused on the role of minor addition elements and their capability to form a high number density of precipitates which can improve the mechanical properties by means of the well known age hardening phenomenon.

Mg-RE system appears as a particularly relevant system to address this scientific topic. It has been found that rare earths (RE) have favorable influence on mechanical properties of magnesium alloys especially at higher temperatures. Despite the wide use of Mg-RE alloys, the scientific understanding of the influence of RE on mechanical properties is incomplete. Development of new Mg-alloys is not based or accompanied by fundamental studies of structural aspects of phase transformation, from the earliest stages to the microstructures responsible for the observed properties such as creep resistance. Schematically, the Mg alloy design strategy is rather based on an empirical approach than on the understanding of chemical and structural phenomena governing the phase transformations.

The fundamental understanding of kinetics of ordering and phase separation is essential for the optimization of material properties. It might be also of great importance for the prediction of the microstructure evolution of machine components made from the materials which are currently in use. These processes in alloys are of great interest both from scientific and technological points of view. Mechanisms of formation and distribution of secondary phases are often quite complex.

In the present work, we studied the early stages of kinetics of decomposition and ordering in the model Mg-Nd and Mg-Y-Nd alloys. Their microstructure is characterized by the presence of thin plate-like ordered ($D0_{19}$ structure) β'' precipitates coherent to the *hcp*-Mg matrix. High number density of these metastable solute rich particles is responsible for the improvement of mechanical properties of these alloys. Study of the conditions of appearance, evolution of composition, morphology, crystallographic relationships of these precipitates etc. at different types of aging times, is very important for the further development of series of new commercial Mg-RE alloys.

The transmission electron microscopy and X-ray (or neutron) scattering techniques allows to study experimentally the chemical order in alloys. The phenomenon of precipitation can be observed by the in-situ small angle scattering technique. Among a numerous analytical microscopes, the tomographic atom probe is the unique instrument which allows the reconstruction of 3D images of materials analyzed at the atomic scale. In the mean time, this instrument enables to perform the local and quantitative measurements of the composition. Moreover, at certain conditions, its good spatial resolution allows to get the crystallographic information on the analyzed material. Therefore, atom-probe tomography provides unique insight on solute behavior and the resulting structure and properties of materials. This technique has been used as major experimental instrument in the present work. It worth noting that in order to improve the understanding of results obtained by atom probe, the conventional transmission electron microscopy analyses have been also carried out.

In parallel with the experimental work, we have undertaken numerical simulations of the kinetics of precipitation in studied alloys. The atomistic kinetic Monte-Carlo (AKMC) method has been chosen for this study. It is based on the fundamental physical mechanism of vacancy diffusion and allows a direct comparison of simulated and atom probe data as both techniques operate at the same atomic scale.

Nevertheless, simulation of phase transformation in Mg-RE alloys is not straightforward as in such systems as Al-Cu, Ni-Fe, Au-Cu, Ni-Al, etc. which became classical examples in textbooks for material science physicists. There exist several reasons for that. First, the magnesium crystal structure is *hexagonal close-packed lattice* (*hcp*). To our knowledge, no kinetic study in *hcp* system has never been undertaken. Second, there is a lack of physical parameters associated to RE

elements and third, the energetic description of Mg-RE systems as it involves both chemical short-range interactions and long-range strain-induced interactions. This latter is a strong obstacles to overcome. It was then decided to start with a more simple system without a strain effect.

Thus, the present work constitutes the first step toward a complete description of these complex systems. We developed an AKMC program to simulate ordering and phase separation in a binary A-B alloy on the *hcp*-lattice with short-range pair interactions. One of our goals is to study the influence of some parameters on the kinetic pathway of the vacancy and on the microstructure.

The plan of this manuscript is following.

In the first chapter, we present the theoretical context of our study. The basic thermodynamic concepts and essential definitions are given in this chapter. Then, the overview of the existing experimental works concerning Mg-based age-hardenable alloys and, in particular, Mg-Nd and Mg-Y-Nd alloys is presented. The significance and perspective of use of APT technique for the study of alloys of interest is pointed and validated by examples of recent studies of Mg-RE alloys.

The second chapter deals with the description of the studied materials. The basic concepts of the tomographic atom probe technique are given in this chapter as well. The last part of the chapter is devoted to the data treatment methods, which were widely used in the framework of the experimental study for APT data analysis.

Experimental results are presented in chapter three. Here we start from the study of equilibrium phase diagram of the binary system. Then, on the example of an analyzed binary Mg-Nd samples, we validate the specific parameters necessary for the APT reconstructions, we point out the apparent problems and their solutions concerning atom probe analysis of studied alloys. Finally, the results of analysis of binary and ternary alloys come. The discussions of the obtained results are provided consequently.

We present in the fourth chapter the general principles of Monte-Carlo simulation methods. In particular we describe the different algorithms used to study this system.

The last (fifth) chapter is devoted to the AKMC study of phase decomposition and ordering in a diluted supersaturated binary alloy on the *hcp*-lattice. The thermodynamics of the system is described first. The parameters necessary for the determination of exchange frequencies of the vacancy with atoms in the framework of the pair-interaction model are given. The results of the study of different kinetic pathways in the systems conclude the presented work.

1 Thermodynamic background and phase transformations in Mg-based alloys.

1.1 Thermodynamic considerations of phase transformations in alloys.

The main use of thermodynamics in physical metallurgy is to allow the prediction of whether an alloy is in equilibrium. Considering phase transformations, we are concerned with changes towards equilibrium. Thermodynamics is therefore a necessary tool. This chapter deals with the basic thermodynamic concepts that are required for a fundamental appreciation of further results and discussions. The essential definitions are given in this chapter as well.

1.1.1 Second phase precipitation.

A thermodynamic analysis of stability and phase transformations in solid solutions is considered. For simplicity, we will consider here the case of a binary substitutional solid solution.

Let us consider quantity ΔW — the typical interchange energy between atoms. At high temperatures, when all ΔW are much smaller than the thermal energy, $k_B T$ ($\Delta W/k_B T \ll 1$, where k_B is the Boltzmann constant, T the absolute temperature), the interaction energy may be neglected and alloys may be treated as random solution, i.e. the probability of finding a particular atom at a particular crystal site (occupation probability) is equal to the corresponding atomic fraction.

At low temperatures, when the typical value of the interaction energy ΔW is much larger than the thermal energy $k_B T$ ($\Delta W/k_B T \gg 1$) in case of nonideal solid solution, the atomic arrangement is determined from the minimum internal energy, U, condition.

Depending on the nature of interatomic interactions, the low-temperature state may correspond to either an ordered phase or a mixture of ordered phases, disordered phases, or ordered and disordered phases. This can involve both composition and structural changes.

Let us consider a binary alloy with compositions of atoms A and B equal to c_A and c_B, respectively. Decomposition of a supersaturated single-phase alloy into two-phase state commonly occurs at constant temperature, T, and pressure p, and is thus driven by the reduction of Gibbs free energy:

$$G = U + pV - TS, \tag{1.1.1}$$

where V is the volume occupied by the alloy and S its entropy. Thermodynamic equilibrium is attained when G has reached a global minimum, i.e.

$$dG_{T,p} = dU + pdV - TdS = 0. \tag{1.1.2}$$

Usually for phase separation in solids the term pdV can be neglected with respect to the others in Eq. 1.1.2. Thus a good approximation for G is given by Helmholtz free energy

$$F = U - TS. \tag{1.1.3}$$

Equilibrium is achieved if F is minimized. Unmixing only takes place if the transition from the single-phase state lowers the free energy. In later case, a solid solution being unstable state decomposes into a two phase mixture.

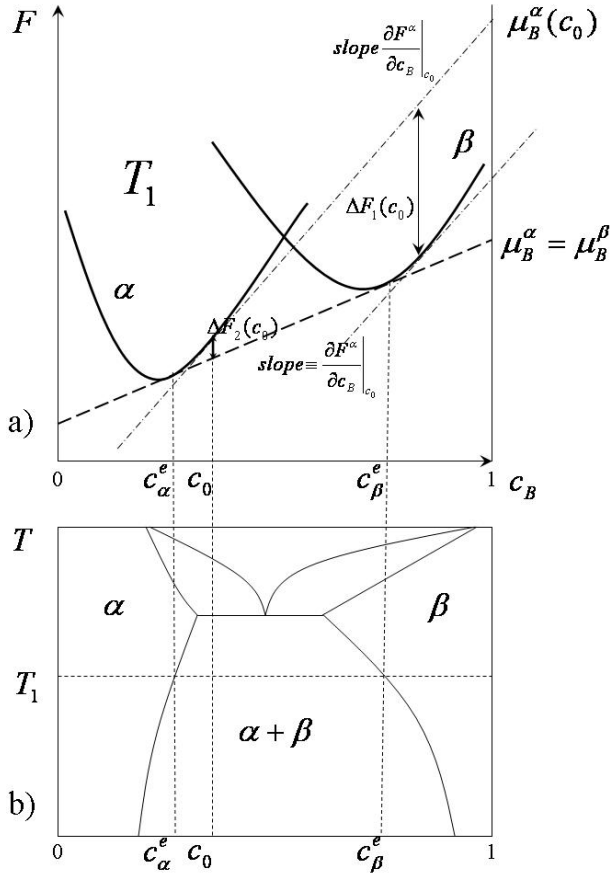

Figure 1.1.1: a) Free energy as a function of composition for a binary alloy with a miscibility gap at temperature T_1. The changes in free energy and the resulting driving forces, ΔF, for unmixing are are illustrated. b) Phase diagram of a binary model alloy. The two phase region, $\alpha + \beta$, is shown and corresponds. The equilibrium compositions, c_α^e and c_β^e, at temperature T_1 are defined by the free energy curve.

The construction of an equilibrium diagram is more fully appreciated when considered in relation to corresponding isothermal free energy composition diagrams, one of which is drawn in Figure 1.1.1a for the phase diagram shown in Figure 1.1.1b. For a given temperature, volume, and solute concentration of a binary alloy, equilibrium between the two phases α and β can only be achieved if the concentrations of A and B in the two phases have been established such that

$$\left(\frac{\partial F^{\alpha}}{\partial n_B}\right)_{T,V,n_A} = \left(\frac{\partial F^{\beta}}{\partial n_B}\right)_{T,V,n_A}, \tag{1.1.4}$$

where n_i is the number of i atoms per unit volume. In other words, at equilibrium the chemical potentials μ_B^{α} and μ_B^{β} (or μ_A^{α} and μ_A^{β}) of the component B (or A) in the two phases are identical and the two phases have a common tangent to the associated free energy curves. This fact is illustrated in Figure 1.1.1 for a supersaturated solid solution of composition $c_B = c_0$, which decomposes into B-depleted phase α and B-rich phase β of composition c_{α}^e and c_{β}^e, respectively. c_{α}^e and c_{β}^e are fixed by the common tangent to the free energy curves of the α- and β-phases.

The reduction in free energy during the transformation from the initial to the final state provides the driving force for nucleation, $\Delta F(c_0)$. The driving force for precipitation is composed of two different contributions:

- the gain in chemical free energy, $\Delta F_{ch} < 0$, associated with the formation of a unit volume of the precipitating phase;
- reduction of the driving force by the elastic strain energy, $\Delta F_{el} > 0$, accounting for the coherency strains which result from a variation of the lattice parameter with the spatial composition fluctuations.

The precipitating phases may have different crystal structures. The situation, when the lattice structure of the matrix differs from that of precipitating phase is common. In this case, we have to deal with boundaries between different solid phases, where the two adjoining crystals can have both different compositions and crystal structures.

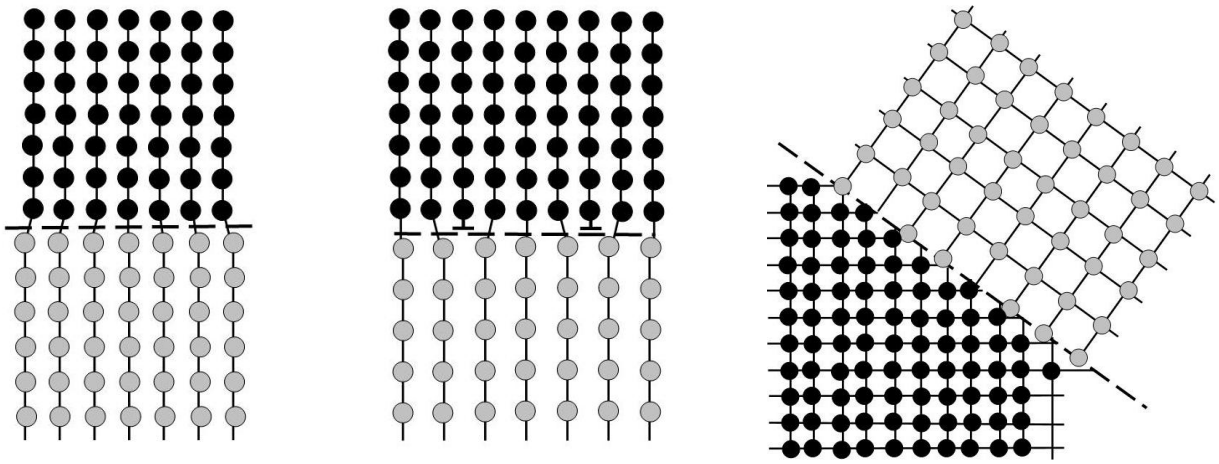

a) b) c)

Figure 1.1.2: Different types of interphase interfaces: a) a coherent interface with slight mismatch leads to coherency strains in the adjoining lattices; b) a semicoherent interface. The misfit parallel to the interface is accommodated by a series of edge dislocations; c)an incoherent interface.

Interphase boundaries in solids can be divided on the basis of their atomic structure into three classes (see Figure 1.1.2):

- A *coherent* interface arises when the two crystals match perfectly at the interface plane so that the two lattices are continuous across the interface. When distance between the atoms across the interface is not identical, it is still possible to maintain coherency by straining one or both of the two lattices. This case is actually shown as an example of coherent interface in Figure 1.1.2a.

- For sufficiently large atomic misfit (or interfacial area), it becomes energetically more favorable to replace the coherent interface with a *semicoherent* interface in which the disregistry is periodically taken up by misfit dislocations (Figure 1.1.2b).

- When the interfacial plane has very different atomic configuration in the two adjoining phases there is no possibility of good matching across the interface, the interface, then, is said *incoherent* (Figure 1.1.2c).

1.1.2 Precipitation sequence.

The complete decomposition of a supersaturated solid solution (SSSS) is usually a complex process which may involve several stages. Let us name ΔF^*, the energy increase associated to

formation of a nucleus. This energy barrier ΔF^* depends on both the driving force of precipitation and the nucleus/matrix interface energy, γ. If the equilibrium phase has a different type of structure from that of the matrix, precipitates are separated from the matrix by a high-energy incoherent interface. In such a case, the energy barrier to overcome for precipitation, ΔF^*, is very high (ΔF_2^* in the inset of Figure 1.1.3) and then the nucleation rate is very low. Thus, the system prefers to nucleate metastable phases which have coherent or semi-coherent interfaces with the matrix. Even if they have a lower driving force for nucleation (see for example β'' and β' in Figure 1.1.3) the low cost of the interface lowers ΔF^* (see ΔF_1^* in the inset of Figure 1.1.3). These phases nucleate earlier. Once nucleated, clusters of a secondary phases start to grow.

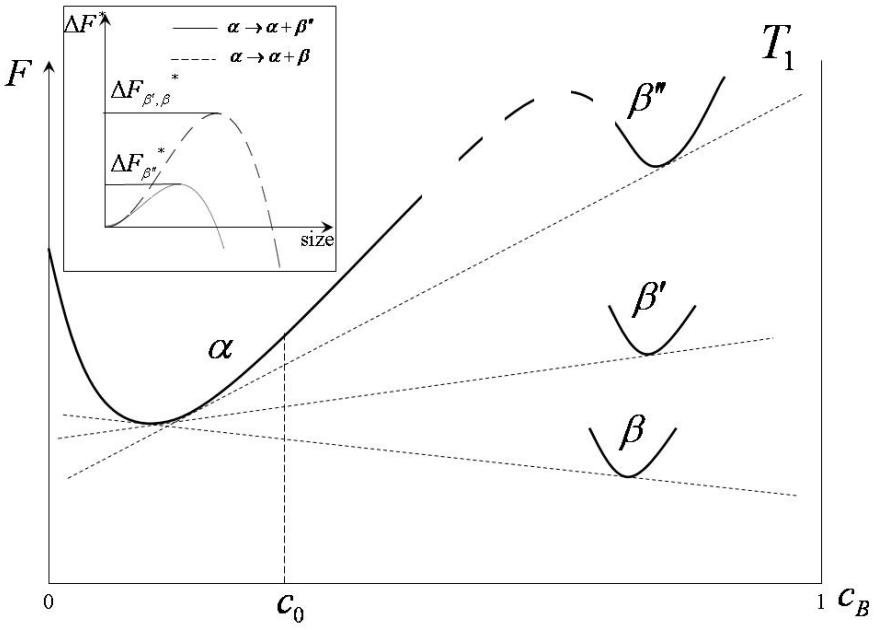

Figure 1.1.3: A schematic free energy diagram showing the driving forces for formation of metastable, β'' and β', phases and the equilibrium one, β at the temperature T_1. In the inset, the nucleation barriers for formation of metastable β'' and equilibrium β-phase are schematically illustrated.

They become less stable in comparison to equilibrium precipitates and transform or dissolve to form the equilibrium phase. This leads to the formation of a *precipitation sequence* to reach the thermodynamic equilibrium.

1.1.3 Precipitate morphologies.

The elastic strain energy affects not only the driving force for the precipitation and indirectly favors the formation of precipitation sequence, but also has a strong influence on the shape and

orientation of the formed precipitates.

In general the total elastic energy depends on the shape and elastic properties of matrix and a precipitate inclusion. As has been shown by Khachaturyan et al. [Kha67,Kha69,Kha83] the shape and orientation of a new phase coherent inclusion in an anisotropic crystal can be determined from analysis of strain energy.

The equation for the strain energy of an isolated coherent inclusion within an infinite anisotropic matrix has been obtained in a particular case when

- the phase transition is assumed to involve one type of crystal lattice rearangements only;
- the precipitates are simply connected regions of a finite volume.

In this case the equation for the strain energy has the following form (see [Kha83] for details):

$$E_{elast} = \frac{1}{2} \iiint_{-\infty}^{\infty} \frac{d^3k}{(2\pi)^3} B(\vec{n}) |\theta(\vec{k})|^2, \tag{1.1.5}$$

where $\theta(\vec{k})$ is the Fourier transform of the shape function of an arbitrary shaped coherent inclusion, and $B(\vec{n})$ is the function of the direction $\vec{n} = \vec{k}/k$, which contains all information on the elastic properties of the system and crystallography of the phase transformation.

When we have at our disposal the closed form of the total strain energy generated by a coherent inclusion of a new phase having an arbitrary shape, it is then natural to raise the question: what is the shape that minimizes strain energy (and, thus, free energy of the system) for a given inclusion of volume V? The correct answer to this question enables us to predict habit planes and orientations of new phase precipitates.

Having done the accurate analysis of the expression for strain energy (Eq. 1.1.5), one arrives at the following conclusion [Kha83]: *the minimum strain energy at a given inclusion volume is attained if the inclusion is "rolled out" to give an infinite platelet of infinitesimal thickness whose habit plane is normal to the vector* $\vec{n}_0$ *minimizing the function* $B(\vec{n})$.

It should, however, be remembered that an "unrolling" of a coherent inclusion into an infinitesimal thickness sheet minimizing the strain energy can never take place in actual systems, because of a competing effect: an unlimited increase of the surface energy. Competition between the strain and surface energies leads to inclusions of various shapes observed.

Qualitatively, it is clear that plate-like inclusions should be expected in cases of low interphase

energies and considerable mismatch between the parent phase and inclusion crystal lattices. On the other hand, with large interphase energies and small crystal lattice mismatch, spherical and polyhedral inclusions should predominate. In some special cases, when strain effect is quite strong, but the minimum of the function $B(\vec{n})$ is degenerate with respect to any $\vec{n}$ lying in a plane, the rodlike shape of precipitates might be detected.

1.1.4 Kinetics of phase transformation and age-hardening.

The thermodynamic description applies to systems that are in stable or metastable equilibrium. Thermodynamics can therefore be used to calculate the driving force for a transformation but cannot predict how fast a transformation will proceed. The study of how fast processes occur belongs to the science of *kinetics*. The theoretical and experimental investigation of the kinetics of phase transformation in alloys is one of the main problems of physical metallurgy. Knowledge of speed of phase transformation, conditions of formation of stable and equilibrium phases, deep understanding of mechanisms of transition between phases helps to choose and apply effective procedures to improve the mechanical (and some others) properties of alloy. One of such procedures is *precipitation hardening*.

Age hardening, also called *precipitation hardening*, is a heat treatment technique used to increase the yield strength of malleable materials. It relies on changes in materials microstructure to produce fine particles of an impurity phase, which impede the movement of dislocations, or defects in a crystal's lattice. The technique is widely used to improve the mechanical properties of alloys. The basic requirement for an alloy to be amenable to age-hardening, is a decrease in solid solubility of one or more of the alloying elements with decreasing temperature. Phase diagram of *age-hardenable* systems can often be compared to the schematic phase diagram displayed in Figure 1.1.4 (alloys which fulfill this criteria are called *age-hardenable*).

Heat treatment normally involves the following stages:

1. Solution treatment at a relatively high temperature, T_s, within the single phase region to dissolve the alloying elements (point **1** in Figure 1.1.4).

2. Rapid cooling or quenching (to room temperature) to obtain an SSSS of these elements.[1]

[1]Hence, systems for which the supersaturated solid solution cannot be retained upon a rapid cooling are not suitable.

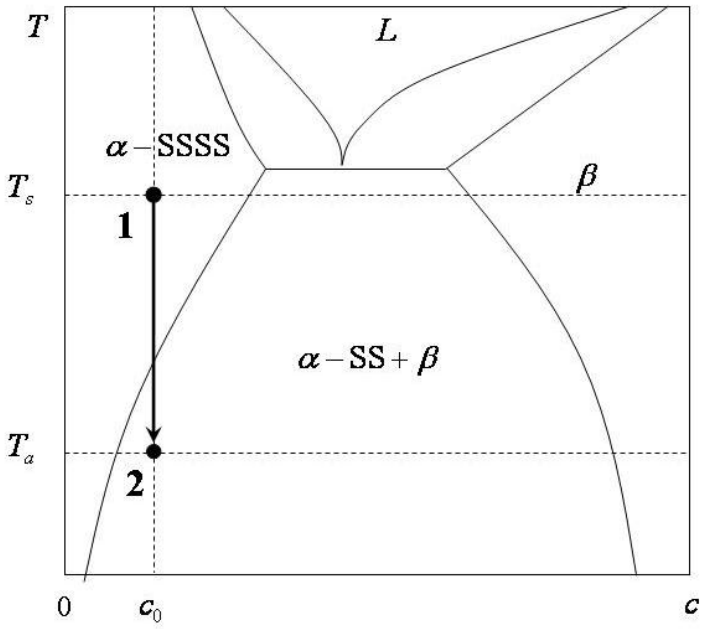

Figure 1.1.4: A typical phase diagram of an age-hardenable alloy.

3. Controlled decomposition of the SSSS to form finely dispersed precipitation, usually by aging (for convenient times) at intermediate temperature(s), T_a (point **2** in Figure 1.1.4).

The mechanical response of the systems varies with the aging time. The study of the kinetics of phase transformation in alloy is, therefore, very important for development of commercially useful materials.

Although we are most familiar with the precipitation process in binary alloys, our expanding knowledge of the behavior of multi-component systems indicates that precipitation in complex alloys occurs qualitatively in the same way that it does in the binary systems. Detailed study of the multi-component systems is now mainly governed by experimental techniques.

1.2 Review on Mg-based alloys

Magnesium being one of the most abundant elements on the Earth is also the lightest structural metal. It has a hexagonal-close packed crystallographic structure (see Appendix C for details). Some of the main physical properties of magnesium are given in Table 1.2.1.

Property	Value
Atomic number	12
Molar mass	24.3 kg/mol
Crystal structure	*hcp*
a	0.3203 nm
c	0.5199 nm
Melting point	650°C
Density	1738 kg/m^3
Elastic modulus	45 GPa

Table 1.2.1: Some physical properties of pure Magnesium.

The element (metal) is highly reactive. The free metal burns with a characteristic brilliant white light. Unlike aluminum, the presence of an oxide film on bulk and molten magnesium does not protect the metal from further oxidation. On the contrary, it accelerates this process. Melting is complete at 650°C and the rate of oxidation of the molten metal surface increases rapidly with rise in temperature such that, above 850°C, a freshly exposed surface spontaneously bursts into flame. Consequently, inert atmospheres must be used when handling magnesium and its alloys. Heat treatments are normally performed in atmospheres of inert gases or in salt baths, in order to avoid oxidations and explosions due to the low fire resistivity of the materials.

Magnesium is rarely used for engineering applications without being alloyed with other metals. However, at present the use of low cost Mg alloys is limited compared to aluminum alloys, mainly because of their poor mechanical and creep properties at elevated and high temperatures.

Mg-Al system constitutes the basis of the most widely used magnesium casting alloys since these materials were introduced for the industry needs. Commonly used Mg alloys contain from 8 to 9wt.% aluminium with small amounts of zinc, which gives some increase in tensile properties, and manganese, which improves corrosion resistance. Commercial magnesium alloys for automotive applications are AZ91[2](Mg-9.0Al-0.7Zn(wt.%)), AM50 Mg-5.0Al-0.4Mn(wt.%), and AM60 (Mg-6.0Al-0.4Mn(wt.%)). These alloys offer an excelent combination of mechanical properties, corrosion resistance and die castability. However, they have poor creep resistance at temperatures above 150°C, due to the low thermal stability of the intermetallic $Mg_{17}Al_{12}$ phase responsible for the age hardening. The latter makes them inadequate for major powerstrain applications.

There have been enormous efforts in developing creep resistant magnesium alloys [Mor01,

[2]According the American Society for Testing Materials the first two letters indicate the principal alloying elements, thus A corresponds to aluminium, E — rare earth, H — thorium, M — manganese, W — yttrium, Z — zinc and so on.

Mor02, Luo04] in the past decade. It has been found that among other elements of the periodic table, rare earths (RE) have favorable influence on mechanical properties of magnesium alloys especially at higher temperatures [Pol95].

All Mg-RE systems form eutectic phase diagrams with limited and decreasing solubility with the decreasing temperature, thus fulfilling one of the criteria for age hardening; furthermore, relatively good castability is maintained. The typical aged microstructure of Mg-RE alloys at maximum hardness has been reported to contain metastable and equilibrium phases as dispersed nanoscale precipitates. Very often they form as plates on the prismatic planes of Mg. These prismatic precipitate plates have been suggested [Nie03] to play an important role in strengthening by providing effective barriers to gliding dislocations. It is thus of interest to determine the structure, orientation and composition of such precipitates and to identify those factors responsible for their presence in Mg-RE systems. Moreover, RE-containing precipitates are thermally stable, ensuring hot strength and creep resistance.

The precipitation behavior of different binary Mg-RE alloys is quite similar. The typical precipitation sequence of the decomposition of supersaturated solid solution is following [Pol95, Smo04b]:

$$\alpha'(\text{hcp}) \rightarrow \beta''(\text{DO}_{19}) \rightarrow \beta' \rightarrow \beta$$

The first transient phase has hexagonal D0_{19} structure (see Appendix D for details) and is coherent to the close packed hexagonal α'-Mg matrix. Its appearance at the early stages of precipitation was reported in all investigated binary (and multicomponent) Mg-RE systems. On the contrary, the structure of metastable β' and equilibrium β phases depends on type(s) of rare-earth element with which magnesium was alloyed.

Despite the wide use of Mg-RE alloys, the scientific understanding of the influence of RE on mechanical properties is incomplete. The study of the kinetics of precipitation in binary Mg-Nd and ternary Mg-Y-Nd model systems is the main goal of the present work. The literature review on Mg-RE alloys which comes in the next sections is, hence, focused on the two systems.

1.2.1 Precipitation in the binary Mg-Nd system.

The addition of Nd in dilute amounts ($<$ 1at.%) to Mg results in a significant increase in hardening and strength after artificial aging. The increase in hardness is reportedly due to

formation of plate-shaped GP zones and precipitates on prismatic planes of the *hcp*-Mg matrix [Pik73, His02, Wil03]. This is why the binary Mg-Nd system is the basis for development of alloys which are in current commercial use (WE series alloys).

At relatively low temperatures (typically for $T < 250°C$) the sequence of precipitation found in this system is following:

$$\alpha'(\text{hcp}) \rightarrow \text{GPzones} \rightarrow \beta''(\text{DO}_{19}) \rightarrow \beta'(\text{bco}) \rightarrow \beta(\text{bct})$$

First this was reported in the pioneering work of Pike and Noble [Pik73]. Authors investigated the precipitation behavior of a binary Mg-0.5at.%Nd alloy by electrical resistivity and electron microscope techniques. The resistivity measurements showed distinct kinetic regions, suggesting the existence of four phases in precipitation sequence called Guinier-Preston (GP) zones, β'', β' and β respectively. The conditions under which each phase precipitates were defined. By-turn, using the transmission electron microscopy the information on the morphology, orientation and structure of newly formed precipitates were determined:

- GP zones suggested to be needle shaped with long axes parallel to the magnesium [0001] direction.
- The β'' was reported plate shaped, with a $\{11\bar{2}0\}$ habit. The structure is that of the perfectly coherent DO_{19} superlattice, with

$$[0001]_{\beta''} \parallel [0001]_{Mg},\ (11\bar{2}0)_{\beta''} \parallel (11\bar{2}0)_{Mg}.$$

- The β' phase was plate shaped with a $\{1\bar{1}00\}$ habit plane. The possible structure was proposed to be body-centered orthorhombic phase (bco).
- β particles were found to be incoherent and of body-centered tetragonal symmetry.

Almost in the same time the formation of GP zones has been suggested by Gradwell [Gra70] and later by Karimzadeh [Kar85]. But the zones in contrast to the Pike's results reported to be platelet on $\{1\bar{1}00\}$ matrix plane. This inconsistence between researchers stimulated the further investigations of GP zones in Mg-RE alloys. In particular, in the work of Hisa et al. [His02] using conventional TEM, HREM and computer simulation, the crystallographic features of a precipitate

formed in the early stage of aging of Mg-1.3wt.%Nd alloy have been analyzed. Detailed analysis and simulation of diffraction patterns have been performed and the results are summarized as follows

- The precipitates were reported to be two dimensional and formed on $\{1\bar{1}00\}$ matrix prism planes.
- The crystal structure of precipitates was found to be based on the DO_{19} superlattice. The structure contained atomic steps that were similar to anti-phase boundaries in ordered alloys and were arranged periodically along $< 11\bar{2}0 >$ as it is shown in Figure 1.2.1.

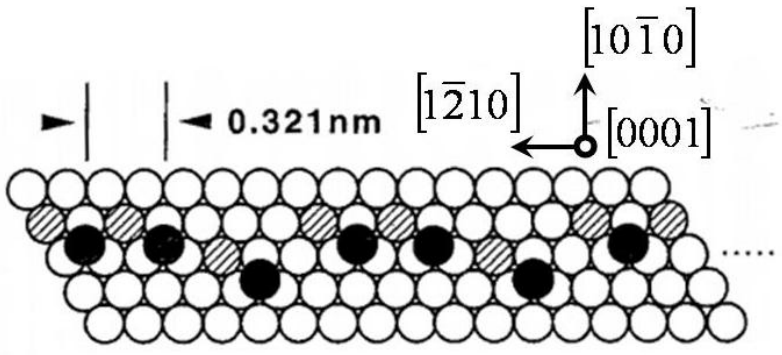

Figure 1.2.1: Crystal structure model for the stepped quasi-$D0_{19}$ precipitate proposed by Hisa et al. [His02]. The shaded circles represent the positions of Nd atoms on $(0001)_{Mg}$, the full circles the positions of Nd atoms on $(0002)_{Mg}$, and the open circles the position of Mg atoms on $(0001)_{Mg}$.

The most recent TEM investigation of the binary Mg-3.0wt.%Nd system at 200 °C performed by Wilson et al. [Wil03] suggested the existence of platelet precipitates with habit planes parallel to both $\{11\bar{2}0\}$ and $\{1\bar{1}00\}$ matrix planes. The $\{1\bar{1}00\}$ plates revealed to be thicker and shorter in length than the $\{11\bar{2}0\}$ platelets. However, it remained unclear in the work whether the precipitates were GP zones or β''.

The information about the precipitation phases in binary Mg-Nd system is summarized in Table 1.2.2.

Phase	Structure	Temperature range	Habit plane of plates
GP zones	thin $D0_{19}$	room temperature — 180 °C	$\{1\bar{1}00\}$
β''	$D0_{19}$	180 °C — 260 °C	$\{11\bar{2}0\}$ and $\{1\bar{1}00\}$
β'	bco	200 °C — 320 °C	$\{1\bar{1}00\}$
β	bct	300 °C — $\sim$ 545 °C	?

Table 1.2.2: Overview of occurrence conditions and orientations of phases in Mg-Nd alloy.

1.2.2 Precipitation in the ternary Mg-Y-Nd system.

A small addition of Y as an alloying element to the binary Mg-Nd system leads to a synergistic beneficial effect on magnesium's properties. It improves the tensile yield strength, fatigue strength, and creep resistance of Mg-Nd alloy [Agh08]. The latter caused a raised interest to the study of a Mg-Y-Nd system.

One of the first studies of the ternary system was realized by Vostry et al. [Vos88] who studied the isothermal annealing of Mg-6.0wt.%Y-3.0wt.%Nd alloy undertaken at 200 °C. The annealing response was investigated by hardness testing, electrical resistivity and TEM measurements. The results obtained were compared with those observed for the corresponding binary alloys Mg-6.0wt.%Y and Mg-3.0wt.%Nd. The results revealed that neodymium was responsible for the observed precipitation hardening. Structural changes accompanying the decomposition of the supersaturated solid solutions were investigated by TEM and revealed the formation of needle shaped precipitates parallel to the $< 1\bar{1}00 >$ directions.

Most of later works were devoted to the study of precipitate microstructure in more complex commercial Mg-RE alloys WE43 (Mg-4.0wt.%Y-3.0wt.%Nd(RE)-0.4wt.%Zr) and WE54 (Mg-5.25wt.%Y-3.5wt.%Nd(RE)-0.4wt.%Zr), which are based on the ternary Mg-Y-Nd system.

The precipitation sequence which is observed in these alloys is a complicated one and depends on the aging temperature and alloy composition [Smo04b, Smo04a]. It can be written as

$$\alpha'(\text{hcp}) \rightarrow \text{GPzones} \rightarrow \beta''(\text{DO}_{19}) \rightarrow \beta'(\text{bco}) \rightarrow \beta_1(\text{fcc}) \rightarrow \beta(\text{fcc})$$

The β'' precipitates have the ordered DO_{19} hexagonal superlattice structure similar to one observed in binary Mg-Nd system.

The β' precipitates has body centered orthorhombic structure with lattice parameters

$$a_{\beta''} = 0.64 \text{ nm}, \; b_{\beta''} = 2.23 \text{ nm}, \; c_{\beta''} = 0.52 \text{ nm},$$

Its orientation relationships with the matrix are following:

$$[001]_{\beta'} \parallel [0001]_{Mg}, \; (100)_{\beta'} \parallel [2\bar{1}\bar{1}0]_{Mg}.$$

The equilibrium β precipitate is *fcc* with $a = 2.23$ nm and the orientation relationship

$$[011]_{\beta} \parallel [0001]_{Mg}, \; (1\bar{1}1)_{\beta} \parallel [1\bar{2}10]_{Mg}.$$

The early stages of precipitation in a Mg-Y-Nd based alloy (Mg-4.0wt.%Y-3.3wt.%Nd(RE)-0.5wt.%Zr[3]) aged at 150 °C have been studied in details using TEM and small X-ray scattering (SAXS) in two works of Antion et al. [Ant03, Ant06]. By SAXS analysis, it was demonstrated that precipitation occurs in the alloy after solution treatment and quench, coherent with GP zone assumption. The expected size of particles was less than 0.7 nm, so they were not detected by the TEM examinations.

After the earliest stages the alloy microstructure consist of monoplanar precursors showing a DO_{19} chemical ordering with two possible habit planes: $\{1\bar{1}00\}$ and $\{11\bar{2}0\}$. With prolonged aging times at 150°C, monoplanar precipitates develop in both β'' and β' precipitates. According to Antion et al. [Ant03, Ant06], the $\{1\bar{1}00\}$ monoplanar precipitates lead to the formation of the β'-bco phase whereas the monoplanar precipitates with $\{11\bar{2}0\}$ habit plane form the coherent β'' phase.

In the work of Nie and Muddle [Nie99, Nie00], the late stages of decomposition of WE54 alloy were investigated. In this alloy aged at 250°C, the precipitation sequence involves initial formation of globular particles of metastable β' phase, skipping the GP zones and β'' phase formation (or passing this phase very rapidly). The previously unidentified phase β_1 has been revealed here as a major intermediate precipitate phase in this system. It had an *fcc* structure formed as plates with habit plane parallel to $\{1\bar{1}00\}_{Mg}$ and the following orientation relationships:

$$[110]_{\beta_1} \parallel [0001]_{Mg}, \; (\bar{1}12)_{\beta_1} \parallel [1\bar{1}00]_{Mg}.$$

Preferential nucleation of β_1 phase in association with the β' particles, which are invariably located at the end-facets of the β' plates, is suggested to be the consequence of shear strain energy accommodation. With extended aging, the metastable β_1 phase transforms *in situ* to the equilibrium β phase.

[3]It is believed that Zr additions do not play a part in the precipitation microstructure of interest here.

The results of Nie and Muddle [Nie99,Nie00] were reproduced by Apps et al. [App03a,App03b] on a simplified version of the commercial alloy WE43, noted there as WN42 and having the composition Mg-4.0wt.%Y-2.25wt.%Nd(RE)-0.6wt.%Zr. The existance of β_1 phase was confirmed, as well as the formation of β'' precipitates during the very early stages of ageing (up to 1 h) even at 250°C. The direct formation of β_1 precipitates (with no evidence of β'' and β' phases) as plates on $\{10\bar{1}0\}_{Mg}$, followed by an in situ transformation to the β precipitate was observed only at 300 °C isothermal aging. Later difference in precipitation behaviour of the alloy in comparison with the one of Nie and Muddle [Nie00] can be, of course, explained by the alloys composition difference. In addition, here was shown that the nucleation of the β_1 phase was associated with the β'' precipitates.

In the work of Lorimer et al. [Lor99] a determination of the composition of the transition phases formed in WE54 has been performed. It was found that coherent β'' phase has the composition $Mg_3(Y_{0.85},Nd_{0.15})$, β' precipitates are consistent with the precipitates having the composition $Mg_{12}YNd$. However, the composition of the β precipitates is found to be a function of alloy composition, thus having the $Mg_{12}YNd$ stoichiometry in WE54 alloy and $Mg_{12}(Y_{0.33},Nd_{0.67})$ in WE43.

Summarizing the information presented above, one will write the phases involved into the precipitation sequence of Mg-Y-Nd based alloy and temperatures ranges of there existence as it is given in the Table. 1.2.3:

Phase	Structure	Temperature range	Habit plane
GP zones	thin $D0_{19}$	$\sim 100°C - 150°C$	$\{1\bar{1}00\}$ and $\{11\bar{2}0\}$
β''	$D0_{19}$	$100°C - 250°C$	$\{1\bar{1}00\}$ and $\{11\bar{2}0\}$
β'	*bco*	$150°C - 250°C$	$\{1\bar{1}00\}$
β_1	*fcc*	$> 250°C$	$\{1\bar{1}00\}$
β	*fcc*	$> 250°C$	$\{1\bar{1}00\}$

Table 1.2.3: Overview of the occurrence conditions and orientation of phases in Mg-Y-Nd containing alloys.

1.2.3 Investigation of precipitation by means of APT in Mg-RE alloys.

The characterization of the microstructure of age-hardened alloys is a complicated problem. The investigation of tiny nano-scale precipitates which play the most significant role for improvement of mechanical properties of these alloys is rather difficult. It has been already almost fifteen

years as together with transmission electron microscopy, the tomographic atom probe technique (APT) is used for the study of inner microstructure of alloys. In case of age-hardened aluminum alloys and steels, the chemical composition of nano-scale precipitates formed in the early stage of aging have been successfully characterized by APT.

Atom probe being an ideal experimental technique for detection of solute atoms in alloys, has been used surprisingly not much for magnesium alloys characterization. Currently, only few atom probe characterization results of magnesium alloys have been reported.

The characterization of Mg alloys by APT meets some specific complications:

- Due to the low evaporation field of Mg, obtaining a stable field ion microscopy (FIM) image is not possible even with hydrogen. This limits some possibilities of the technique.
- Preparation of samples and their storage is a tricky procedure because of the high oxidation rate of pure-Mg and most of its alloys.
- High difference between evaporation fields of Mg-matrix and precipitates rises the probability to meet evaporation and reconstruction artifacts typical for APT analysis.
- The few-nanometer size and usually nonspherical (often plate-like) shape of precipitates (in Mg-RE alloys in particular) complicates to the analysis of microstructure.
- There is not so much experimental and theoretical data on APT and FIM analysis of materials with *hcp*-lattice, which is typical for magnesium and it alloys.

Despite the complications listed above, Ping et al. [Pin02] reported a first successful atom probe analysis of nanocristalline $Mg_{97}Y_2Zn_1$ alloy. The tiny objects observed in the system were characterized at the nanometric scale. Then, APT technique with either voltage or laser pulses, has been applied to various Mg-alloys: Mg-Ca-Zn [Oh05], Mg-Zn-Ag-Ca [Men09], Mg-RE-Zn-Zr [Pin02, Pin03], Mg-Gd-Zn [Hon05, Nie08], Mg-Gd-Y-Zn [Hon07][4]. A quantitative atom probe analysis allowed to observe such tiny objects as GP zones formed in Mg-6wt.%Zn [Oi08] as well as to measure their local composition. In some cases, when the atomic resolution was achieved and it was possible to reconstruct atomic planes, APT was able to demonstrate crystallographic relationships between the matrix and formed precipitates [Pin03, Nie08].

[4]Later three systems are relative to the Mg-Nd and Mg-Y-Nd systems, except that additions of Zn changes the habit plane of precipitates from a prismatic to the basal one [Wil03].

The possibility to gain a very accurate local compositional information with atom probe was used for matrix concentration measurements in many-component commercial Mg-based alloys [Sta09], as well as to investigate solute clustering in solid solutions of Mg-alloys [Nie08, Sta09].

In the work of Nie et al. [Nie08], to examine whether there existed any interactions between Gd and Zn atoms in the solid solution phase of alloy in as-quenched conditions and pre-aged conditions, a statistical approach, namely contingency table analysis [Mil02], was used. This approach compares experimentally observed frequencies of atoms of the two elements in individual compositional blocks with those expected for a perfectly random distribution of atoms of the two elements. It was shown by means of statistical test that the probability of a random distribution of Gd and Zn atoms was extremely low in the as-quenched alloys, whereas the co-segregation of Gd and Zn atoms gradually became difficult to detect during isothermal aging at 200°C.

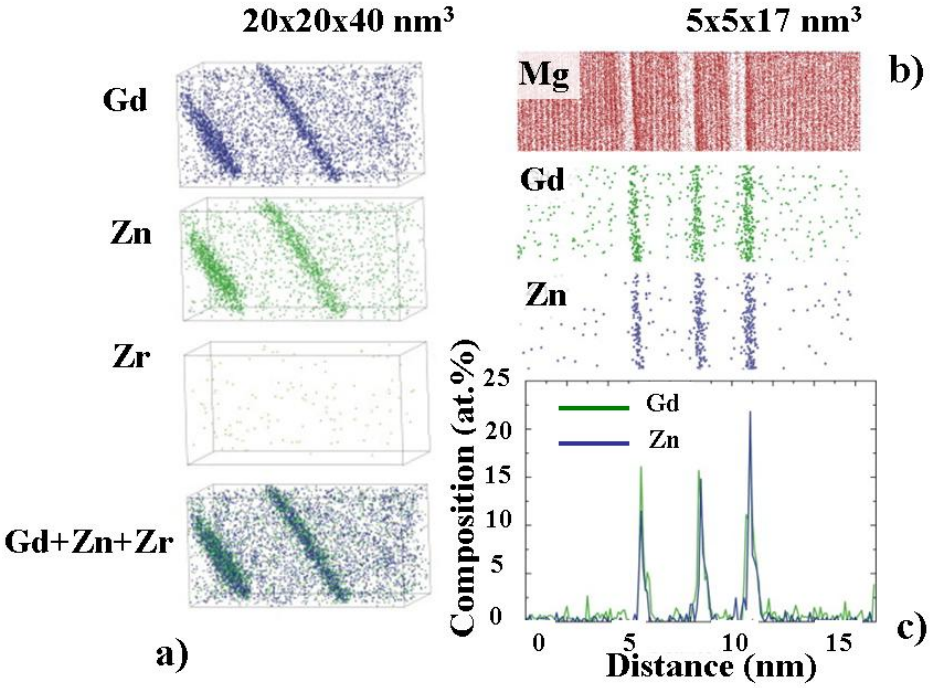

Figure 1.2.2: a) APT maps of γ'' precipitate plates formed in Mg-1.0Gd-0.4Zn-0.2Zr(at.%) alloy samples aged for 2 h at 250°C; b) APT maps showing distribution of Gd and Zn atoms in three γ'' precipitate plates formed in Mg-1.0Gd-0.4Zn-0.2Zr(at.%) alloy samples aged for 8 h at 250°C; c) composition profile of the three γ'' precipitates in a). The figures were taken from the work of Nie et al. [Nie08].

As an example of somewhat advanced possibilities of atom probe technique in application to Mg-alloys, Figure 1.2.2a shows the laser assisted atom probe tomography of Mg-1.0Gd-0.4Zn-

0.2Zr(at.%) alloy containing plate-like RE-rich γ'' precipitates in peak-aged conditions. Figure 1.2.2b illustrates that (0002) atomic planes are resolved in the magnesium matrix, but the resolution is lost near the precipitate. This is due to preferential retention of Gd atoms because of its higher evaporation field compared to Mg. Nevertheless, it is possible to conclude, that basal planes are habit planes for those precipitates. Figure 1.2.2b shows APT maps of Gd and Zn in three γ'' precipitates. Zr is not shown in these maps because, as it was investigated, its atoms do not segregate preferentially to precipitates. The composition profile in the direction normal to the habit planes of γ'' plates is also shown in Figure 1.2.2c. For the three precipitates shown in the figure, the averaged concentration of Gd in the plates is 15at.% and the Zn content is also 15at.%.

1.2.4 Conclusion.

The overview of APT measurements presented above characterizes this technique as helpful and promising for the investigation of Mg-alloys. The unique possibility of the technique to visualize in three dimensions alloy's microstructure at the atomic scale offers the promising opportunities for the study both early and late stages of decomposition in Mg-based age-hardenable alloys. APT provides the possibility to measure precisely local compositions of new-phase heterogeneities at the nanometer scale. Finally, the shape of precipitates of the secondary phase(s) can be directly visualized, and in certain cases, when the atomic resolution is achieved, habit planes and precipitate orientation relationships can be reconstructed.

The systems of our interest, binary Mg-Nd alloy and ternary Mg-Y-Nd one were intensively investigated by transmission electron microscopy. In the mean time, these alloys have never been analyzed by atom probe technique, regardless of the fact that this tool is perfectly suitable to investigate the early stages of phase decomposition. In the present work, the results on the atom probe study of age-hardened Mg-Nd and Mg-Y-Nd alloys are presented. The early stages of the decomposition, which plays the significant role in the alloys hardening response are analyzed. Results on kinetics of precipitate growth in terms of atomic fractions, local compositions and precipitate number densities are provided. The orientation relationships of plate-like precipitates occurring in the alloys are analyzed, despite the fact, that they appear on the prismatic planes of *hcp*-lattice which are rather difficult to resolve. The qualitative and quantitative comparison between APT and TEM data for some alloy samples is given in order to provide the link between

two techniques.

References

Agh08. E. Aghion, Y. Gueta, N. Moscovitch, B. Bronfin, *Journal of Materials Science*, **43**(14):4870 (2008).

Ant03. C. Antion, P. Donnadieu, F. Perrard, A. Deschamps, C. Tassin, A. Pisch, *Acta Materialia*, **51**(18):5335 (2003).

Ant06. C. Antion, P. Donnadieu, C. Tassin, A. Pisch, *Philosophical Magazine*, **86**(19):2797 (2006).

App03a. P. J. Apps, H. Karimzadeh, J. F. King, G. W. Lorimer, *Scripta Materialia*, **48**(5):475 (2003).

App03b. —, *Scripta Materialia*, **48**(8):1023 (2003).

Gra70. K. Gradwell, Ph.D. thesis, University of Manchester (1970).

His02. M. Hisa, J. Barry, G. Dunlop, *Philosophical Magazine A*, **82**(3):497 (2002).

Hon05. T. Honma, T. Ohkubo, K. Hono, S. Kamado, *Materials Science and Engineering A*, **395**(1-2):301 (2005).

Hon07. T. Honma, T. Ohkubo, S. Kamado, K. Hono, *Acta Materialia*, **55**(12):4137 (2007).

Kar85. H. Karimzadeh, Ph.D. thesis, University of Manchester (1985).

Kha67. A. G. Khachaturyan, *Sov. Phys. Solid State*, **8**:2163 (1967).

Kha69. A. G. Khachaturyan, G. A. Shatalov, *Sov. Phys. JETP*, **29**:557 (1969).

Kha83. A. G. Khachaturyan, *Theory of structural transformations in solids*, Wiley, 1983.

Lor99. G. Lorimer, R. Azari-Khosroshahi, M. Ahmed, in *Japan Institute Of Metals, Proceedings, (jimic-3), Pts 1 And 2 - Solid - Solid Phase Transformations*, edited by M. Koiwa, K. Otsuka, T. Miyazaki, volume 12, pp. 185–192, Japan Inst Metals, 1999.

Luo04. A. Luo, *International Materials Reviews*, **49**:13 (2004).

Men09. C. Mendis, K. Oh-ishi, Y. Kawamura, T. Honma, S. Kamado, K. Hono, *Acta Materialia*, **57**(3):749 (2009).

Mil02. M. Miller, *Atom Probe Tomography Plenum Publishers*, New York, 2002.

Mor01. B. L. Mordike, T. Ebert, *Materials Science and Engineering A*, **302**(1):37 (2001).

Mor02. B. L. Mordike, *Materials Science and Engineering A*, **324**(1-2):103 (2002).

Nie99. J. F. Nie, B. C. Muddle, *Scripta Materialia*, **40**(10):1089 (1999).

Nie00. —, *Acta Materialia*, **48**(8):1691 (2000).

Nie03. J. F. Nie, *Scripta Materialia*, **48**(8):1009 (2003).

Nie08. J. Nie, K. Oh-ishi, X. Gao, K. Hono, *Acta Materialia*, **56**(20):6061 (2008).

Oh05. J. Oh, T. Ohkubo, T. Mukai, K. Hono, *Scripta Materialia*, **53**(6):675 (2005).

Oi08. K. Oh-ishi, K. Hono, K. Shin, *Materials Science and Engineering: A*, **496**(1-2):425 (2008).

Pik73. T. Pike, B. Noble, *Journal of the Less Common Metals*, **30**(1):63 (1973).

Pin02. D. Ping, K. Hono, Y. Kawamura, A. Inoue, *Philosophical Magazine Letters*, **82**(10):543 (2002).

Pin03. D. H. Ping, K. Hono, J. F. Nie, *Scripta Materialia*, **48**(8):1017 (2003).

Pol95. I. Polmear, *Light alloys/metallurgy of the light metals, metallurgy and materials science.*, 1995, 3 edition.

Smo04a. B. Smola, I. Stulíková, *Journal of Alloys and Compounds*, **381**(1-2) (2004).

Smo04b. H. Smola, I. Stulíkova, *Kovove Materialy-metallic Materials*, **42**(5):301 (2004).

Sta09. N. Stanford, G. Sha, A. La Fontaine, M. Barnett, S. Ringer, *Metallurgical and Materials Transactions A*, **40**(10):2480 (2009).

Vos88. P. Vostry, I. Stulíková, B. Smola, M. Cieslar, B. Mordike, *Zeitschrift fur metallkunde*, **79**(5):340 (1988).

Wil03. R. Wilson, C. Bettles, B. Muddle, J. Nie, in *Magnesium Alloys 2003, Pts 1 And 2*, edited by Y. Kojima, T. Aizawa, K. Higashi, S. Kamado, volume 419-4 of *Materials Science Forum*, pp. 267–272, Trans Tech Publications Ltd, 2003.

2 Alloys and principal experimental methods.

2.1 Materials and treatments.

2.1.1 Materials.

The present study aims at the quantitatively studying the earlier stages of precipitation, as well as clarifying the structure and morphologies of the phases involved in the precipitation sequence of Mg-RE alloys. For this purpose two model alloys were elaborated: the binary Mg-Nd alloy and the ternary Mg-Y-Nd alloy. The latter can be considered as a model alloy for commercial WE-series of magnesium alloys. The nominal compositions of the alloys are given in the Table. 2.1.1

	Mg-Nd	Mg-Y-Nd
Y, at.% (wt.%)	-	0.73(2.56)
Nd, at.% (wt.%)	0.51 (2.94)	0.48(2.70)

Table 2.1.1: Nominal compositions of as-received alloys.

The binary and ternary alloys were prepared by melting of high-purity constituent elements (Mg, 99.99 wt.%, Nd, 99.6 wt.% and Y, 99.6 wt.%) at 800°C. Then rapid solidification via two-step squeeze casting procedure was applied: the first step, 80 MPa for 15 s and the second step, 120 MPa for 90 s. All alloy handlings were carried out in atmosphere consisted of mixture of argon and air.

2.1.2 Heat treatments.

Homogenization in the single phase region of the phase diagram (hereafter designated as SHT for solution heat treatment) was performed at temperature T_S for 8 h. For this purpose, cut samples were encapsulated in quartz tubes filled with low-purity argon, so as to preserve samples from a possible oxidation or burning-out. In order to do this, each time, five cycles of pumping (primary vacuum) — introduction of argon were systematically applied before an isostatic atmospheric pressure of argon was maintained in the tubes. Then the tube was sealed off with the help of an ethylene welding torch.

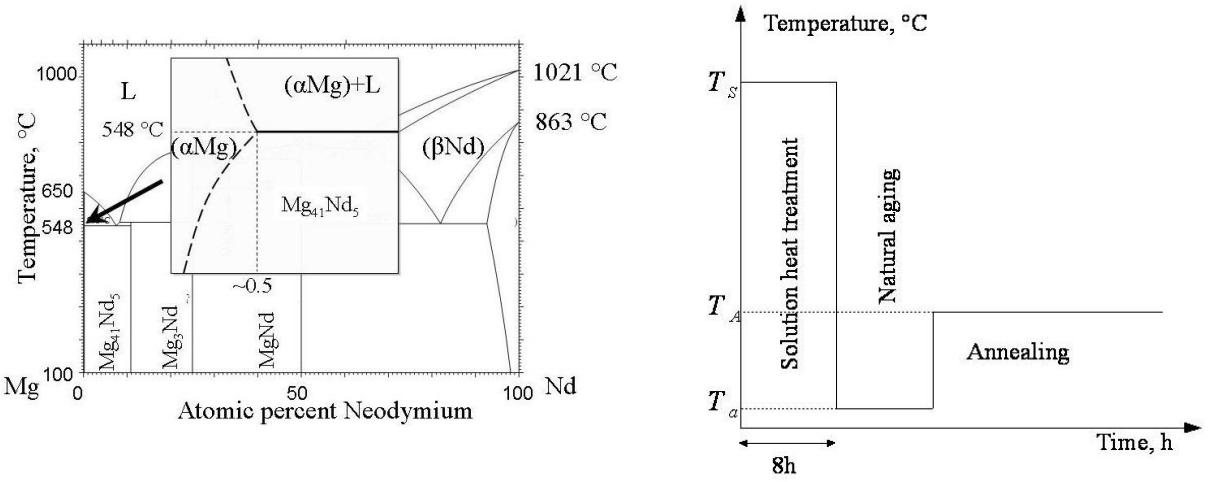

a) b)

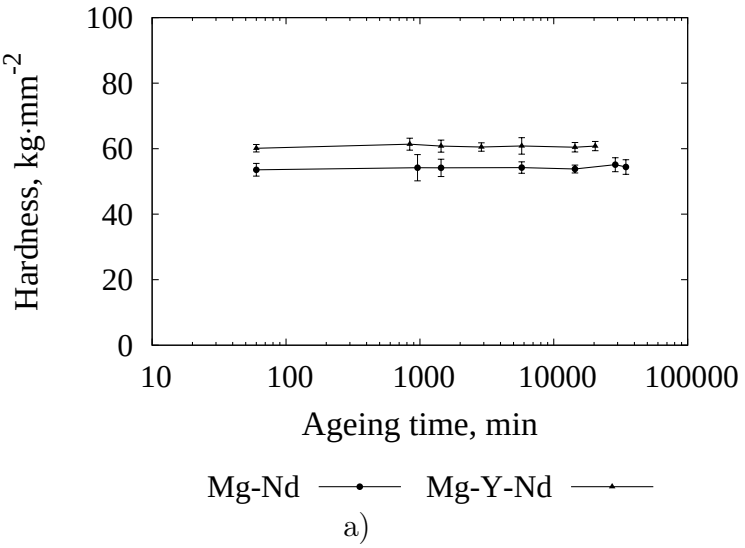

a)

Figure 2.1.1: a) The binary Mg-Nd phase diagram [Oka07]. The inset shows schematically the Mg-rich side of the phase diagram. The solubility limit and eutectic temperature are taken from References [Rok62] and [Oka07]. b) Typical heat treatment sequence. T_S is the temperature of a homogenization; T_A is the temperature of a heat aging; T_a is the room temperature. c) The evolution of hardness in the homogenized Mg-Nd and Mg-Y-Nd alloys at room temperature (natural aging).

For the binary alloy, the SHT procedure was carried out near eutectic temperature, $T_S = 545°C$, where the solubility of the solute must be the highest (see Figure 2.1.1a). The ternary Mg-Y-Nd alloy in as-cast conditions was solution treated at $T_S = 525°C$ in accordance with the procedure suggested by Antion et al. [Ant03]. Finally, homogenized samples were quenched into water at room temperature after the quartz tube being broken.

If further heat treatment procedure required the temperature to be higher than 250°C, SHT

samples were re-encapsulated into quartz tubes to protect them from the oxidation. For lower temperatures of annealing, alloy samples were covered by niobium foils in order to avoid a rough contamination. A typical heat treatment procedure applied in most of the cases is shown in Figure 2.1.1b.

One should mention that after a stage of heat treatment some natural aging followed. The duration of the natural aging has never been controlled. Indeed, according to our hardness measurements presented in Figure 2.1.1c neither ternary nor binary alloys do not reveal a tendency to natural hardening as some aluminum alloys do. Its influence on the further precipitation kinetics is supposed to be negligible.

2.1.3 Preliminary basic study of alloys.

Metallography observations. In order to check the grains microstructure of alloys in as-received and SHT conditions, metallography observations by means of light microscope have been performed on the binary Mg-Nd alloy.

Due to the high oxidation rate of magnesium, it was impossible to obtain proper images of grains after standard polishing with water. That's why we applied an additional stage of polishing with special alcohol based liquid (DP Lubricant Blue Struers) and polishing pastes (size of grains — 3μm and 1μm) which did not contain water. After polishing, samples were etched in *Nital* (10 ml nitric acid (68%) + 200 ml Ethanol) and contrasting images have been obtained (Figure 2.1.2).

One can clearly see the dendritic structure formed during solidification of the melt in Figure 2.1.2a corresponding to the as-cast condition. In contrast to the as-cast microstructure, the microstructure of homogenized sample is "smoother" (Figure 2.1.2b).

These data allowed us to measure the grain size distributions of as-cast and SHT alloys. In Figures 2.1.2c, d grain size distributions are presented for both as-cast and homogenized samples. Size of the grains increased after SHT procedure and the change in distribution is noticeable: in contrast to the distribution of Figure 2.1.2c, which is rather nonuniform, the one from Figure 2.1.2d resembles the log-normal one.

Because it is essential to obtain well homogenized specimen at the microscopic scale, the composition randomness was checked to be sure of the efficiency of the SHT by Electron dispersive X-ray spectroscopy (EDX) experiments.

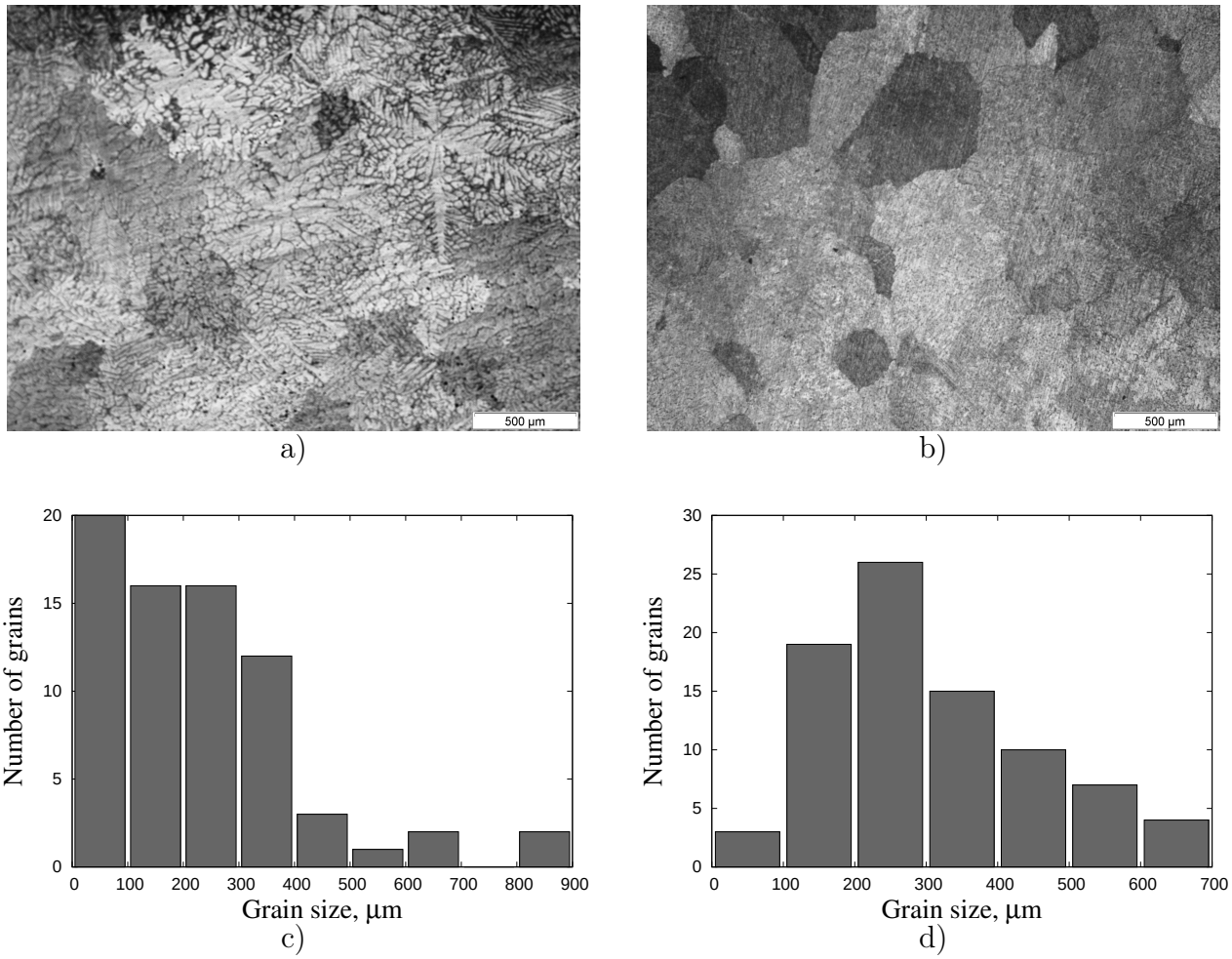

Figure 2.1.2: Light microscope micrographs showing a) as-cast and b) solution treated microstructures of the Mg-Nd alloy. Grain sizes distribution for c) as-cast and d) solution treated microstructures.

EDX study. Figure 2.1.3 shows Scanning electron microscopy (SEM) micrographs of (a) Mg-Nd, (b) Mg-Y-Nd as-cast alloys and (c) Mg-Nd, (d) Mg-Y-Nd homogenized alloys. All images in Figure 2.1.3 corresponding to the as-cast alloys, principally contain two regions in different colors: the RE-rich phase appears with a bright contrast whereas α-Mg is darker. The microstructure of both, binary and ternary alloys are characterized by primary α-Mg dendrites surrounded by intermetallic-containing eutectic in the inter-dendritic regions. While in the samples after SHT, the RE-rich regions have almost completely disappeared. The latter can serve as a proof of sufficiently good quality of the homogenization procedure.

By means of EDX analysis compositions of phases in both alloys were measured. The results are presented in the Table 2.1.2.

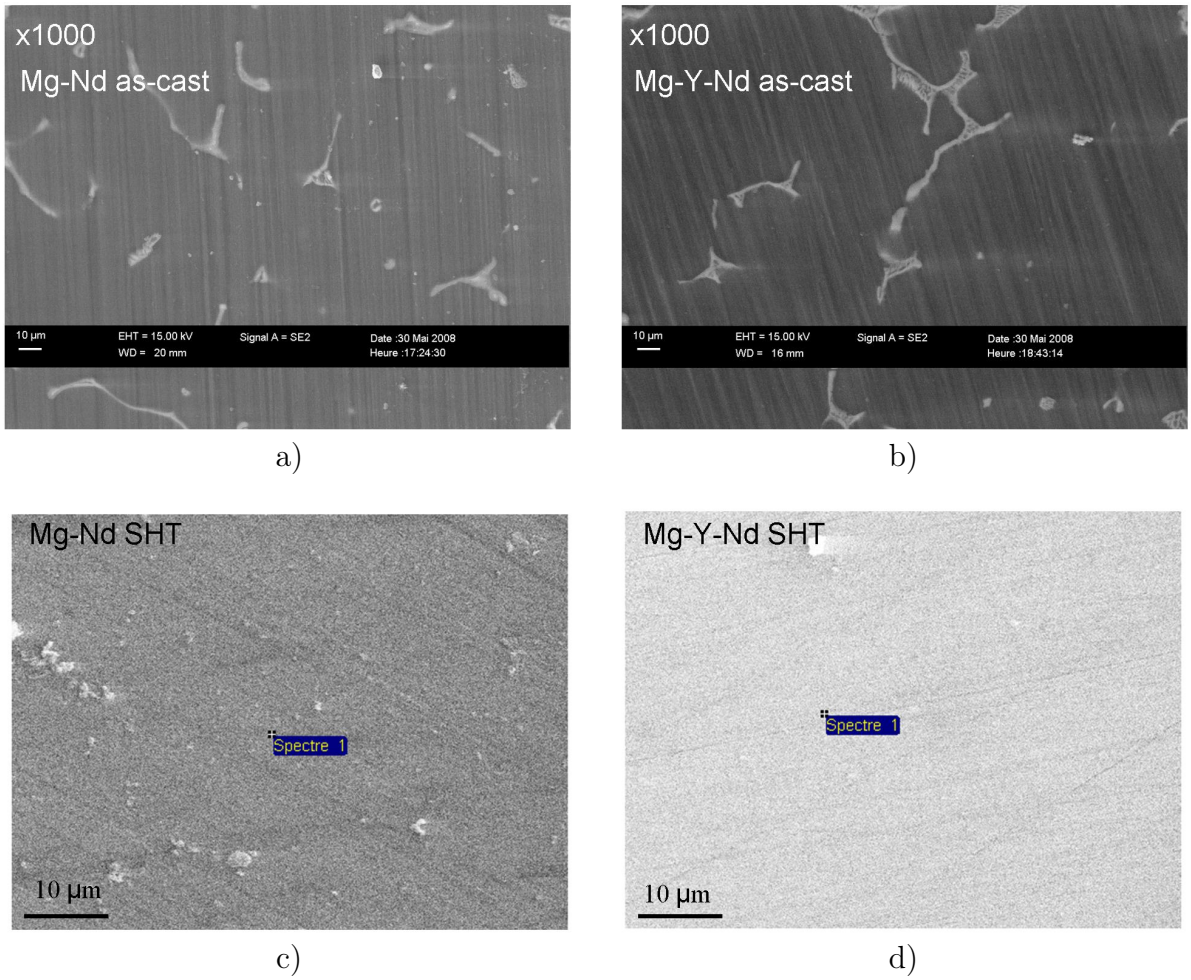

Figure 2.1.3: SEM micrographs showing a)Mg-Nd, b)Mg-Y-Nd as-cast and c)Mg-Nd, d)Mg-Y-Nd solution treated alloys microstructures.

	Mg-rich phase concentration, at.%	RE-rich phase concentration, at.%
Mg-Nd as-cast	- (Nd)	4.8 ± 0.5 (Nd)
Mg-Nd SHT	0.5 ± 0.1 (Nd)	- (Nd)
Mg-Y-Nd as-cast	- (Nd), - (Y)	5.0 ± 0.5 (Nd), 2.1 ± 0.5 (Y)
Mg-Y-Nd SHT	0.5 ± 0.1 (Nd), 0.7 ± 0.1 (Y)	- (Nd), - (Y)

Table 2.1.2: Mean compositions of phases obtained by means of EDX technique.

In as-cast alloys the compositions of Mg-rich phase significantly fluctuated from one point of analysis to another, that's why the data on matrix compositions are not included in the table. The Nd-rich phase observed in binary alloy in as-cast condition should be $Mg_{41}Nd_5$ equilibrium phase, which appears in this composition region of the binary phase diagram (see Figure 2.1.1). However, according to Delfino and Saccone [Del90] it, however, may be also $Mg_{12}Nd$ metastable phase which usually appears after melt cooling.

It is worth to mention that for both phases $Mg_{12}Nd$ and $Mg_{41}Nd_5$, the RE concentration is higher. This disagreement, however, can be explained by the backside signal coming from the matrix during the composition measurements of the fine RE-rich formations.

2.2 Tomographic atom probe technique.

Electric-field- induced evaporation of ions from a needle-like surface, and their subsequent identification by time-of-flight mass spectrometry, forms the basis of the atom-probe technique [Mil92, Bla93a, Bla93b, Dec94]. The microanalytical technique of atom probe tomography (APT) permits the spacial coordinates and elemental identities of the individual atoms within a small volume to be determined with near atomic resolution. Therefore, atom probe tomography provides atomic resolution three dimensional images of the solute distribution within the materials.

In this chapter a brief overview of the technique principles, application and problems in usage is presented. To go deeper into details the reader is referenced to some atom probe reviews [Bla93a, Bla93b, Hon99, Bla00, Cer07, Kel07, Sei07, Mil09] and books [Tso90, Mil96, Mil00].

2.2.1 Principle.

Atom probe is conceived as a field ion microscope (FIM) equipped with a time-of-flight mass spectrometer, so that the observed surface atoms could individually be chemically identified.

In field ion microscopy, a sharp cryogenically-cooled needle-shaped specimen is pointed at a phosphor screen. A trace image gas is introduced into the ultrahigh vacuum system and a positive voltage is then applied to the specimen. When the electric field reaches a critical value, the image-gas atoms are field ionized close to the specimen surface. The resulting ions are repelled towards the phosphor screen where they form the field ion image. When the field is raised sufficiently further, specimen surface atoms are removed as ions. This removal process is called *field evaporation*. Field evaporation enables the interior of the specimen to be analyzed.

The theory of field evaporation has been published previously [Bla88, Cer88, Het91, Bow94]. During field evaporation, atoms positioned at highest field locations, such as step edges, evaporate first. Under applied electric field, the positively charged specimen repels ions created at its surface and the ion trajectories follow the electric field lines established between the specimen and a detector.

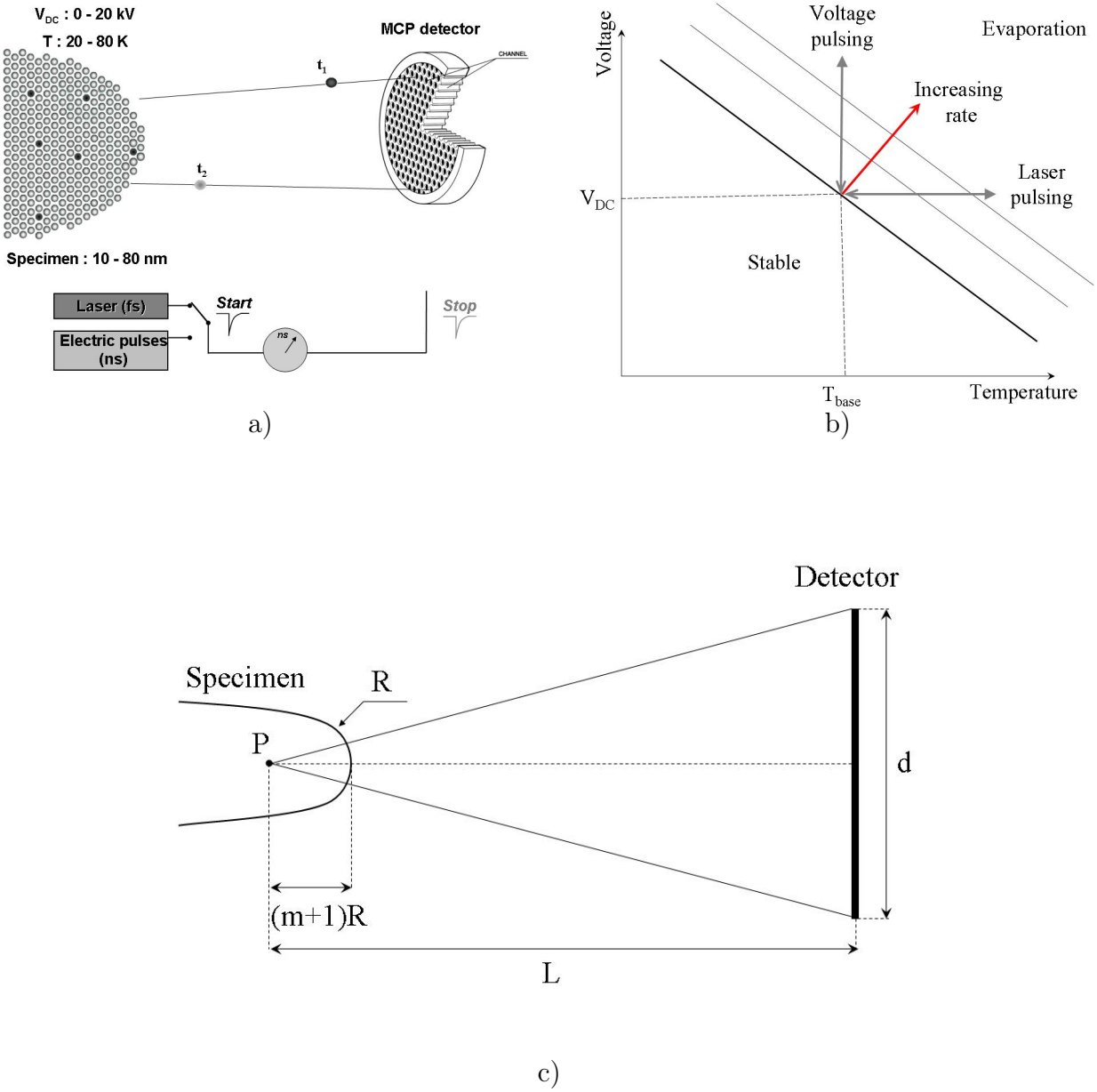

Figure 2.2.1: a) Schematic view of an atom probe; b) Evaporation rate as function of tip temperature and applied voltage; c)the tomographic atom probe as a projection microscope. The magnification is $G = \frac{L}{(m+1)R}$.

Since its invention by E. W. Müller in 1967 [Mul68], the atom probe has been used in numerous scientific areas. Crucial improvements were brought to the initial design. This way, generation of modern three-dimensional atom probes appeared [Cer98,Cer07,Dec07,Kel07,Sei07]. The design of these instruments relies in a general way on the use of a position sensitive detector. As the depth investigation of the material proceeds, a layer-by-layer reconstruction of the analyzed volume can be undertaken and 3D-atomic distribution map can be reconstructed.

A general view of the tomographic atom probe is provided in Figure 2.2.1a. The specimen is

prepared in the form of a very sharp tip ($R \sim 10 - 80$ nm). In order to get reliable composition data, the tip is maintained at low temperatures ($T_{base} < 100$ K). Control of the evaporation process and measure of time of departure is achieved by first establishing a standing field, $V_{DC} \sim 0-20$ kV, below the ionization threshold of the specimen, and then applying short duration electric field, $V_p \sim 0.2V_{DC}$, or laser pulses as shown in Figure 2.2.1b.

As it was shown by Houard and co-workers [Hou10], the physical process involved in the laser-assisted field evaporation is thermal. The localization of the laser-power absorption at the tip apex may be controlled by choosing the appropriate laser polarization and wavelength.

The detector is composed of a microchannel plate stack (MCP) which allows the detection of positions of ion impacts. Once the position of impacts on the detector is known, the coordinate of the atoms at the specimen surface may easily be computed. The calculation is based on geometrical arguments.

Figure 2.2.1c shows that the derivation of atom positions from impact coordinates simply involve a point projection (P). As shown in Figure 2.2.1c, the image magnification is given by the expression:

$$G = \frac{L}{(m+1)R}, \tag{2.2.1}$$

where m is the image compression factor related to the position of the projection point (P). It is generally close to 0.6. R is the tip radius and L is the free flight length of an ion (the estimated specimen to detector distance).

As the specimen is field evaporated, its radius normally increases and hence the magnification decreases. The specimen radius is deduced from the evaporation voltage (V) via the simple relationship:

$$R = \frac{V}{E\beta}, \tag{2.2.2}$$

where E is the evaporation field at the apex of the specimen and β a specimen shape related constant. This relationship is, to a first approximation, a linear relationship with the voltage. Therefore, if the radius is independently determined for a particular evaporation voltage the product $E\beta$ can be estimated. This may be done by examining the specimen in the transmission electron microscope or by counting the number of rings between known poles in a field ion micrograph. The radius at any other voltage can then be extrapolated from Eq. 2.2.2. In the presented work, however, another calibration method was used. It is described in Section 3.2.1.

The x and y coordinates of the position of the ion in the specimen for an analysis along the specimen axis may be expressed as

$$x = \frac{X_a}{G} \qquad \text{and} \qquad y = \frac{Y_a}{G}, \tag{2.2.3}$$

where X_a and Y_a are the coordinates of an ion impact on the detector.

In proportion, as the material is field evaporated layer by layer, a 3D reconstruction of the analyzed volume can be made. In practice the third coordinate (z) is deduced from the number of detected ions (N). A small increment of depth coordinate (Δz) corresponding to the ΔN evaporated atoms is given by formula:

$$\Delta z = \frac{\Delta N \Omega_i}{Q d_a^2}, \tag{2.2.4}$$

where Ω_a is the atomic volume of the i^{th} ion in the phase under analysis, Q the detection efficiency of the detector, and $d_a^2 = (d/G)^2$ is the size of the analyzed area with d being the diameter of the detector (see Figure 2.2.1c). Usually additional corrections are also included in these calculations in order to take into account the curvature of the specimen surface(see, for example [Bas95,Mil00]).

The time-of-flight of field evaporated ions is measured for every evaporation pulse (departure time); the signal produced by the MCP provides the arrival time. The mass-to-charge ratio M/n of arriving ions is then deduced from the applied voltage, $V_{tot} = V_{DC} + V_p$, and time of flights, t, by using the energy balance relationship:

$$neV_{tot} = \frac{1}{2} M v^2, \tag{2.2.5}$$

where $v = L/t$ supposing the absence of energy compensation devices and thus the motion of ions rectilinear and uniform efter evaporation; M is the ion mass, n is the ion charge state (1^+, 2^+...), and e the electron elementary charge.

2.2.2 Detection efficiency and mass resolution.

The typical detection efficiency of an atom probe is $50 - 60\%$ of the ions removed from the specimen. Consequently, about 40% of arriving ions are lost. The loss is mainly due to some ions striking the interchannel regions of microchannel plates in the position-sensitive detector, and

thereby not being detected. These atoms are being lost in a random way, so this effect does not affect the quantitative measurements of composition.

Time-of-flight measurements provide a value for the mass-over-charge ratio of each evaporated ion and therefore their identity. The data collected in an experiment can be represented in the form of mass spectrum (Figure 2.2.2). The latter indicates the number of detected ions as a function of their mass-over-charge ratio (given in atomic mass units, amu).

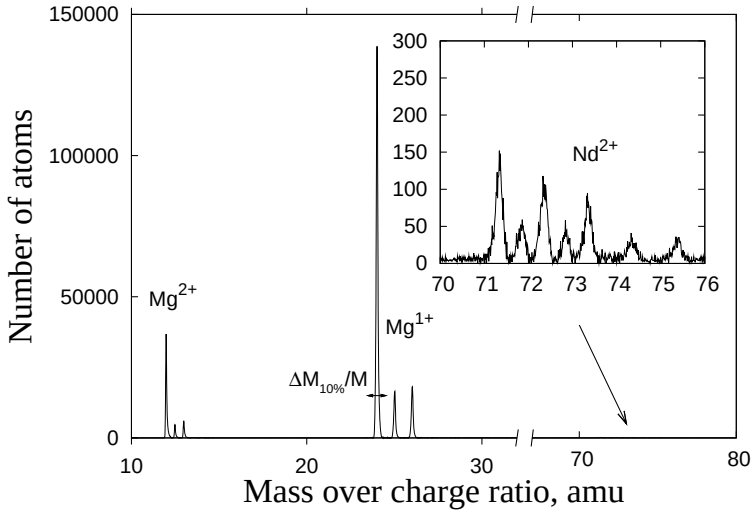

Figure 2.2.2: Typical mass spectrum of a binary Mg-Nd alloy. The mass resolution is defined as the ratio between the major peak position and the peak width on the 10% of its height.

One of the main characteristics of an atom probe is its mass resolution. It characterizes the capability of an instrument to resolve two neighboring peaks on the mass spectrum. It is convenient to define the mass resolution as the ratio between the peak position (in amu) and the peak width on the 10% of its height.

Compositional analysis based on mass spectrum analysis depends on the mass resolution of the atom probe and noise floor. By-turn, the mass resolution mainly depends on the free flight length for ions. The noise level depends on the quality of an analyzed specimen and whether the electric mode or laser mode is used for experiment.

2.2.3 Spacial resolution.

Depth resolution. The depth resolution is determined by the distance of screening of electric field on the specimen surface. In conductive materials it is usually about 0.1 nm. This value is comparable with the typical lattice interplane distances. Typically, the best spacial resolution

is achieved along the depth of analysis and lattice planes of a crystalline materials are usually resolved if their normal is close to the direction of analysis.

Lateral resolution. In the plane perpendicular to the analysis direction, the image of the lattice is blurred. The lateral resolution is of several Angströms. The physical limit is mainly controlled by the ion-optical aberrations. With the typical magnification G of an atom probe (about 10^7), an error in the position of ion impact equal to 1 mm (caused for example by trajectory aberrations of the evaporating ions in the close vicinity of the specimen surface) lead to uncertainties in the range $0.2 - 0.5$ nm. The latter appears to be enough to blur the lattice structure. Deeper discussion concerning spacial resolution of an atom probe one can find in the recent work of Gault et al. [Gau10].

2.2.4 Evaporation and reconstruction artifacts.

Isotope overlap. For some materials not all the peaks in the mass spectrum can be unambiguously assigned to elements because of an overlap of two (or more) isotopes with the same mass-over-charge ratio. It is then impossible to distinguish them on the mass spectrum.

In the case of Mg-Nd and Mg-Y-Nd alloys, this problem seems to be less important, as the most of the major peaks of different elements (their isotopes) are well straddling. Table 2.2.1 provides the principal ion peaks detected during APT analyses.

		Peak position, amu		
Element	Isotope/compound	1^+	2^+	3^+
Mg	^{24}Mg, ^{25}Mg	24.0, 25.0	12.0, 12.5	
	^{26}Mg+$^{24}MgH_2$	26.0	13.0	-
	$^{25}MgH_2$, $^{26}MgH_2$	27.0 , 28.0	13.5, 14.0	
Y	^{89}Y	-	44.5	29.67
	$^{89}YH_2$	91.0	45.5	-
	^{89}YH, $^{89}YH_3$	-	45.0, 46.0	-
Nd	^{142}Nd, ^{143}Nd		71.0, 71.5	
	^{144}Nd, ^{145}Nd	-	72.0, 72.5	-
	^{146}Nd, ^{148}Nd, ^{150}Nd		73.0, 74.0, 75.0	

Table 2.2.1: Principal peaks detected in the mass spectrum constructed after APT analysis of Mg-Nd and Mg-Y-Nd alloys.

Preferential retention and evaporation. This effect can arise because elements with relatively small or large field evaporation may be preferentially evaporated or retained, respectively.

Let us consider a binary alloy with constituents A and B, for which the evaporation fields are different and $E_B > E_A$. In the Figure 2.2.3 three different cases are presented.

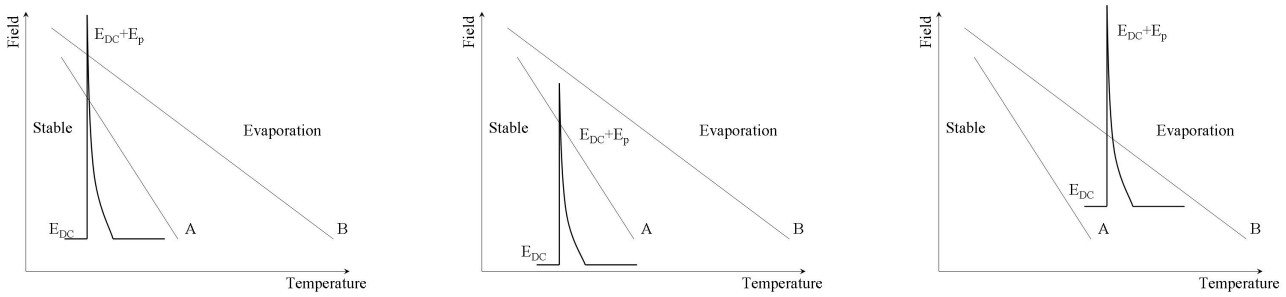

Figure 2.2.3: Influence of electric field formed on the specimen's tip on the evaporation conditions of chemical species A and B: a) proper evaporation conditions; b) preferential retention conditions for B; c) preferential evaporation conditions for A.

- In the case (a) no ions field evaporate at standing field, E_{DC}, and both species start to field evaporate and can be detected after an addition of electric impulses, $E_{DC} + E_p$, where E_p is the field pulse amplitude. Measured compositions are then correct in this case.
- If the increase in field due to application of the pulse voltage is too low, case (b), the element that is more difficult to field evaporate (B) will be retained on the surface.
- If the standing field or voltage on the specimen is too high, case (c), element (A) with the lower evaporation field will preferentially evaporate during the time between the pulses.

Local magnification. When a precipitated phase with an evaporation field different from that of the major (matrix) phase is present in a material, effects of the trajectory abberations can be significant. Indeed, the difference in evaporation fields of two phases provoke local variations of the curvature radius (see Figure 2.2.4). Latter modify the ions trajectories during very first moments of their flights from the specimen surface to the detector [Mil91, Vur00]. The local magnification effect is illustrated in the simulations of ion impacts on the detector given in Figure 2.2.4.

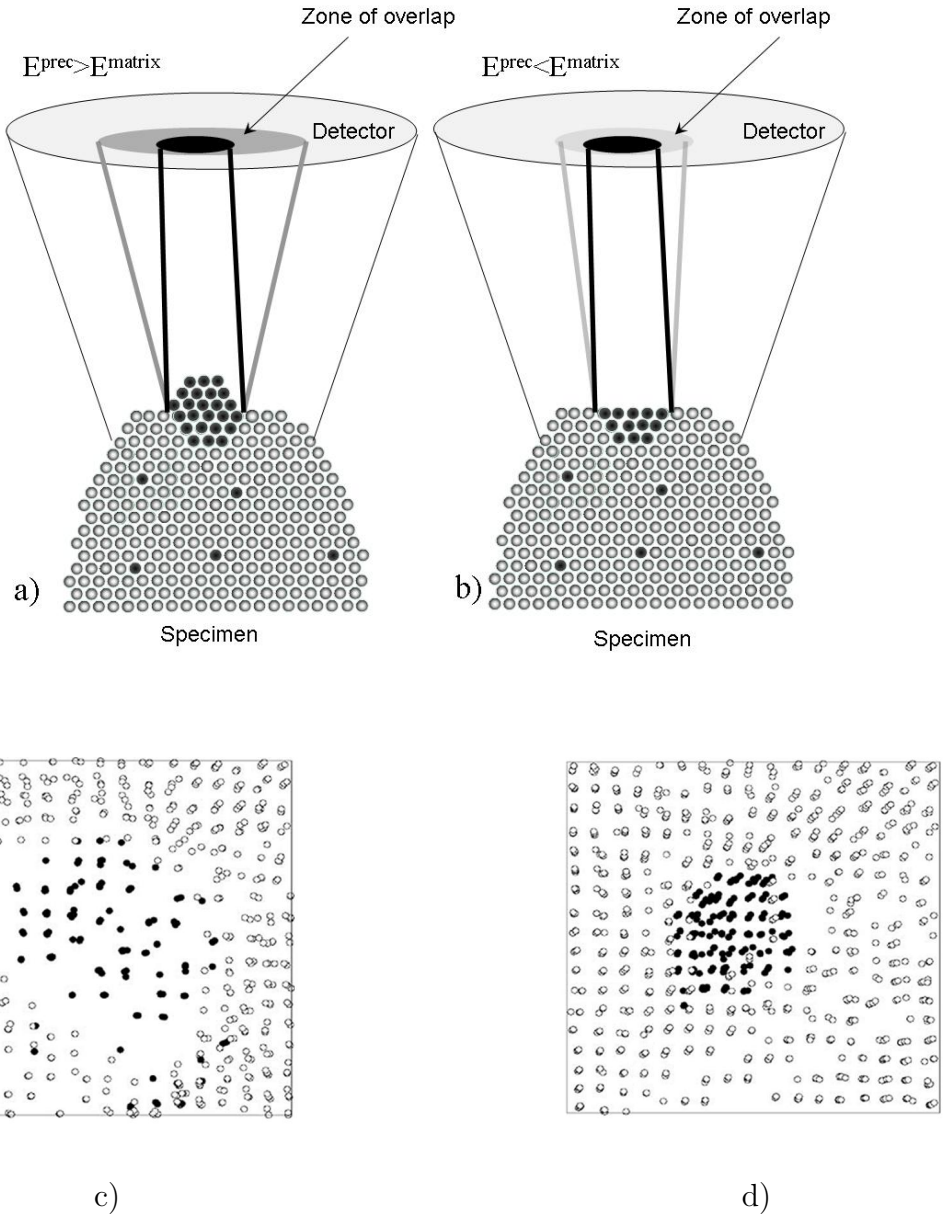

Figure 2.2.4: Schematic of the local magnification effect in case of evaporation of a) a high-field precipitate; b) low-field precipitate. Simulation of impact images for a binary AB alloy containing a spherical β particle (eight interatomic distances in diameter). β phase is pure in B and its environment is pure in A. These two simulated images are cross sections of reconstructed precipitates with c) $E^{prec} > E^{matrix}$ and d) $E^{prec} < E^{matrix}$: B atoms are in black and A are in gray. The images are reproduced from [Bla01].

For a high evaporation field of the particle; precipitate ions fall outside the particle and a depleted zone forms close to the interface (Figure 2.2.4c). In contrast, for a low evaporation field of the particle, the image of the precipitate (pure in B atoms) is compressed and ions coming from the surrounding matrix (pure in A) fall in the particle image (Figure 2.2.4d). More details on the procedure and results of simulations can be found in Reference [Vur00].

The local magnification can consequently modify the morphology and the characteristic di-

mensions of precipitated phases and then trajectory overlaps associated to this effect consequently distort the measured chemical compositions of the phases.

This effect has been observed for the Mg-RE alloys investigated by means of atom probe. The errors introduced by the local magnification and the ways to overcome them is discussed in Section 3.2.4.

2.2.5 Experimental conditions.

In order to reduce the number of artifacts in the APT analysis data, it is necessary to choose correct experimental conditions. The most important parameters in an atom probe experiment are the temperature of the specimen during analysis and the pulse fraction applied to the specimen. If these parameters are not carefully chosen, incorrect compositional estimates may arise because of evaporation artifacts described above.

Experiments were carried out depending on the purpose of the measurements on two instruments: Energy Compensated Tomographic Atom Probe (ECOTAP) and Laser Assisted Wide-Angle Tomographic Atom Probe (LAWATAP) equipped with an advanced Delay Line position-sensitive Detectors (a-DLD) [Cos05]. The use of a-DLD detector minimizes the losses of information due to impact superposition or multi-event detection.

In ECOTAP the energy spread of emitted ions is reduced thanks to an energy compensating device (a reflectron lens [Bem03]). This way, the high mass resolution is provided and, therefore, improved accuracy of composition measurements can be achieved. However, the volume of analysis is not big (typically $10 \times 10 \times 100$ nm^3).

By-turn, LAWATAP, where the view angle is five times more than the ECOTAP's one, provides analyses of volumes with dimensions about $50 \times 50 \times 100$ nm^3. This allows to have a wider view on an analyzed sample microstructure as well as to get a good statistics.

In both cases, atom probe data collection was performed at a specimen temperature of 40 K, a pressure of $< 10^{-8}$ Pa and a target evaporation rate from 0.004 to 0.010 ions per pulse.

ECOTAP was used in electric mode with voltage pulse fraction (pulse voltage over steady-state direct current voltage) approximately equal to 20% and a pulse frequency of 2.0 kHz.

The LAWATAP analyses were performed using femto-second laser pulses with a wavelength $\lambda = 515$ nm (green laser), pulse repetition rate equal 100.0 kHz and a power set-up of the

laser representing $\sim 20\%$ of the standing potential. In order to choose the proper laser power, the equivalent pulse fraction has been adjusted in all experiments according to the geometric procedure illustrated in Figure 2.2.5.

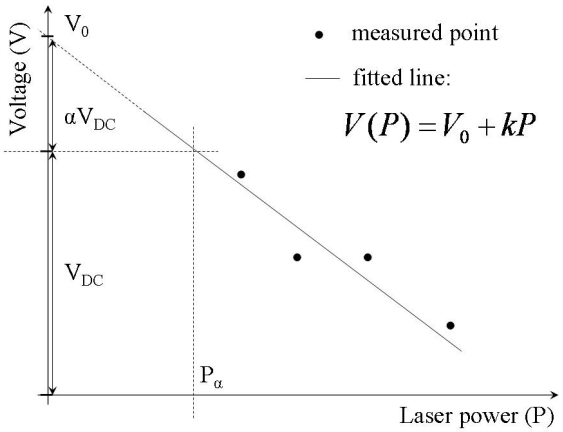

Figure 2.2.5: An example of equivalent pulse-fraction measurements.

For this purpose, at a fixed value of evaporation rate, three or four measurements of standing voltage, V_{DC}, were done for different values of the laser power, P. The dependence V_{DC} versus P is supposed to be linear and can be fitted on the experimental points. From the parameters of linear fit, V_0 and k, one can find the laser power P_α for a desired pulse fraction α using formula:

$$P_\alpha = -\frac{\alpha V_0}{(\alpha + 1)k}, \tag{2.2.6}$$

2.3 Description of atom probe data treatment methods.

2.3.1 Precipitate identification.

The new phase formations, as precipitates and clusters, observed by an atom probe, can be defined as discrete regions enriched in solute atoms. In order to calculate precipitate compositions, the user selects a volume around each region in the 3D atom map that is considered to be a precipitate. The process of selecting the desired region in three dimensions can be difficult, especially in the case of non-spherical, rod-shaped or diffuse precipitates. Therefore, it is convenient to identify the solute atoms belonging to each particle. Thanks to computer techniques this process can be automated.

There are different versions of cluster identification algorithms [Mil02, Vau03, Hei03]. We, however, use the algorithm given below:

1. Explore the vicinity of all atoms. If the number of solute atoms, N_s, (or solute composition, c_s) in the sphere with radius R^{max} centered on a considered atom is less than a chosen threshold N_s^{min} (or c_s^{min}), this atom is labeled as "non clustered". Else (the concentration criteria is fulfilled) this atom is labeled as "clustered".

2. All "clustered" atoms situated closer than R^{max} one to each other belong to the same cluster.

3. Groups of atoms that contain less than a minimum value N_{min} of atoms are removed.

The scheme illustrating the identification process is given in Figure 2.3.1. In Figure 2.3.1b, the sphere of radius R^{max} centered on the atom **1** involves enough solute (black) atoms, so that the atom **1** obeys a clustering criteria. Solute atoms within the thick dashed line will be defined as being a single precipitate. The atom **2** within a given distance R^{max} has no solute atoms, and, hence, is not "clustered".

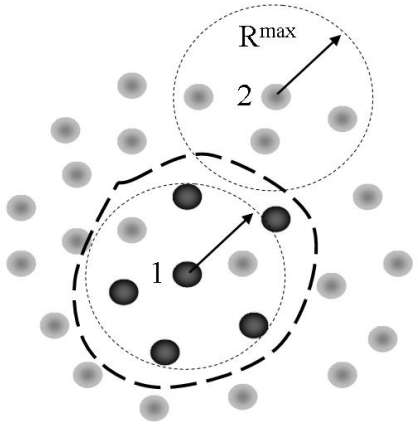

Figure 2.3.1: Schematic diagram showing the precipitate selection process.

The choice of parameters R^{max}, c_s^{min} (or N_s^{min}), N_{min} is obviously important for the results and usually is not a straightforward task. The choice of certain values of parameters will be given in the section of APT results.

2.3.2 Concentration profile technique.

One of the most common forms of data analysis is the construction and statistical analysis of a composition profile. The first step to create a composition profile is to select the volume

within the three-dimensional data from which the composition profile is desired. The shape of this selected volume is usually either a cylinder or a rectangular block depending on the type of feature under analysis.

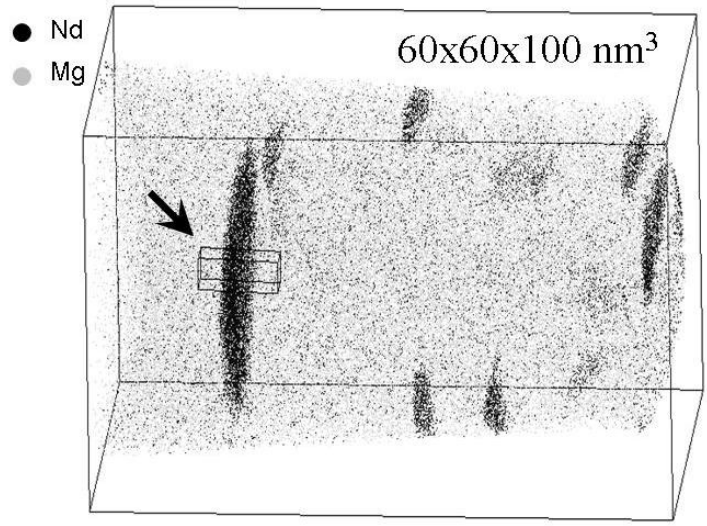

a)

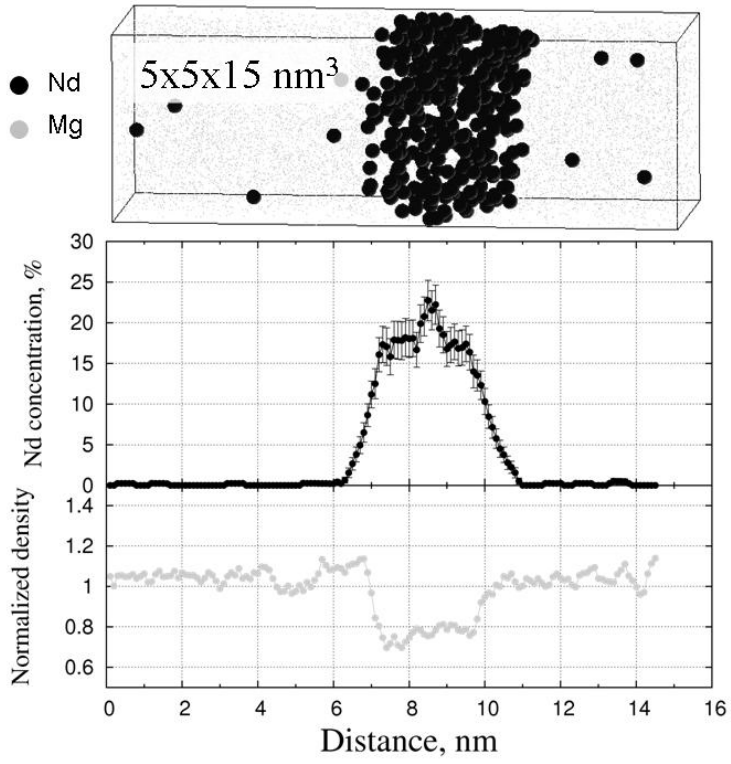

b)

Figure 2.3.2: Atom probe analysis in the Mg-Nd alloy aged at 250°C for 30 min. a) atom map; b) composition and atom number density profile across the interface indicated in (a) by the arrow.

The size and position of this selected volume are then carefully adjusted by the user until the desired volume is enclosed. Once the volume has been selected and correctly positioned, the

atom-by-atom data within the selected volume are divided into small slices perpendicular to one of the axes of the selected volume.

The size of the slices may be defined in terms of distance. The concentration of all the elements present in each slice are then determined based on the number of atoms of each elemental species with the use of the standard equation:

$$c^i = \frac{N_s^i}{N^t}, \tag{2.3.1}$$

where N_s^i is the number of ions of solute i, and N^t is the total number of ions detected in the sampling volume. The estimate of standard error of this measurement, σ^i, is given by

$$\sigma^i = \sqrt{\frac{c^i(1-c^i)}{N^t}}. \tag{2.3.2}$$

An example of a composition profile across an interface is shown in Figure 2.3.2.

In the same way, the atom number density profile may be estimated, where instead of Eq. 2.3.1 one should use

$$N_\nu = \frac{N_t}{\nu}, \tag{2.3.3}$$

where N_t is the number of observed atoms in the volume ν. This type of profiles allow to detect local fluctuations of atomic density in the vicinity of (low- or high-field) precipitates, crystallographic poles or other artifacts.

In atom number density profiles, instead of absolute values of N_ν we use the normalized density ρ, which does not depend on the size of a sampling volume. The normalized atomic density is given by the following equation

$$\rho = \frac{N_t \Omega}{abc}, \tag{2.3.4}$$

where Ω is the (average) atomic volume; a, b, c are the dimensions of the sampling volume.

2.3.3 Pair correlation functions.

The cosegregation and antisegregation behavior of the solute elements in an alloy at the early stages of phase separation may be examined with the use of pair correlation functions [DG06]. This method is effectively used in the cases, when atomic clusters contain very few atoms and, thus, cannot be revealed by other methods.

The pair-correlation function $g_{ij}(r)$ represents the probability function of having two atoms of given natures (i, j) at a distance r, reduced to a unit density. It can be derived from the radial distribution function $G_{ij}(r)$ by the following relation:

$$g_{ij}(r) = \frac{G_{ij}(r)}{4\pi\rho r^2 dr}, \tag{2.3.5}$$

where ρ is the atomic density. The radial distribution function, $G_{ij}(r)$, is the probability density of finding an atom j at r when an atom i is at the origin.

Let us consider a volume containing N_A atoms of type A and N_B atoms of type B. For computing the A-B pair correlation function, we count the number $n_{AB}(r)$ of B atoms situated between a distance of r and a distance $r + dr$ of any A atom. It will be given by the expression $n_{AB}(r) = N_A G_{AB}(r)$. Thus, between r and $r + \Delta r$

$$g_{AB}(r) = \frac{n_{AB}(r)}{4/3\pi[(r + \Delta r)^3 - r^3]N_A N_B/V}. \tag{2.3.6}$$

The pair correlation function is unity if there is no correlation between A and B, greater than 1 if there is a positive correlation and less that 1 if there is a negative correlation.

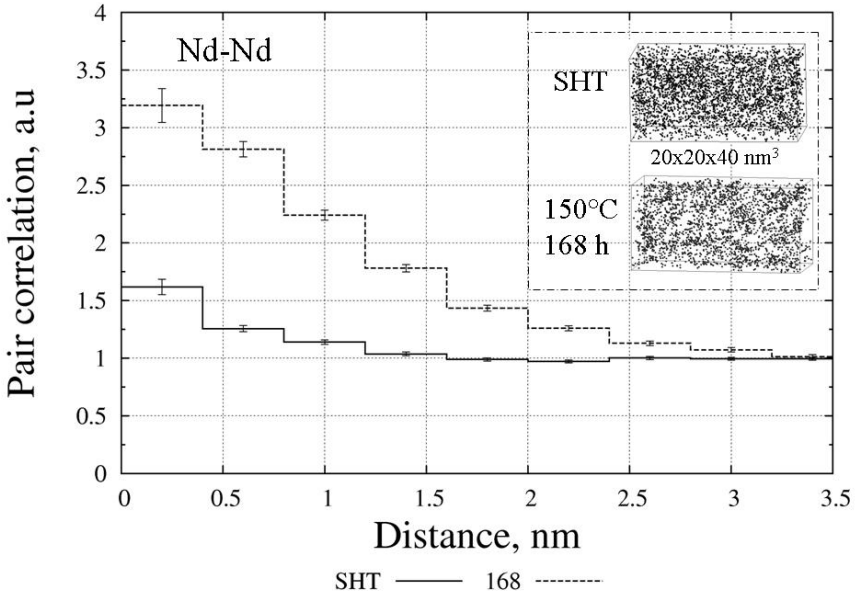

Figure 2.3.3: Example of Y-Y pair correlation functions for solution heat treated and aged (at 150°C for 168 h) Mg-Nd-Y samples. The APT atomic volumes of the Mg-Nd-Y samples are provided in the inset (only Nd atoms are shown).

Equivalently, Eq. 2.3.6 can be transformed in the following form:

$$g_{AB}(r) = \frac{c_{AB}(r)}{\langle c_B \rangle}, \tag{2.3.7}$$

where $c_{AB}(r)$ is the mean concentration of atoms B within a spherical layer between spheres with radii r and Δr around an atom B; $\langle c_B \rangle = N_B/V$ is the average concentration of atoms B in the analyzed volume V.

An example of a pair-correlation analysis is given in Figure 2.3.3. A visual analysis of the distribution of Nd atoms (see APT maps in the inset in Figure 2.3.3) hardly reveal any evidence for the formation of clusters following the heat treatment of Mg-Y-Nd alloy sample at 150°C for 168 h. However the pair correlation function showed that the Nd exhibit much pronounced positive autocorrelation in the aged sample than in the solution heat threated one.

In the theory of errors (see e.g. [Tay96]), if a measured quantity, $\aleph$, is given as a function of independent quantities, $\{X_i\}$: $\aleph = f(\{X_i\})$ $(i = 1..N)$, then the error, $\Delta\aleph$, is calculated from the errors of independent quantities, $\{\Delta X_i\}$, as follows

$$\Delta\aleph = \sqrt{\sum_{i=1}^{N} \left\{ \frac{\partial f}{\partial X_i} \Delta X_i \right\}^2}, \tag{2.3.8}$$

where ΔX_i are the errors made in the measurements of quantities X_i.

According to Eq. 2.3.8 the error $\Delta g_{AB}(r)$ can be expressed as follows

$$\Delta g_{AB}(r) = \sqrt{\left\{ \frac{c_{AB}(r)}{\langle c_B \rangle^2} \Delta_{\langle c_B \rangle} \right\}^2 + \left\{ \frac{1}{\langle c_B \rangle} \Delta_{c_{AB}} \right\}^2}, \tag{2.3.9}$$

where $\Delta_{c_{AB}}$ and $\Delta_{\langle c_B \rangle}$ are given by standard deviations:

$$\Delta_{c_{AB}} = 2\sigma(c_{AB}) = 2\sqrt{\frac{c_{AB}(r)(1 - c_{AB}(r))Q}{N(r)}}$$

$$\Delta_{\langle c_B \rangle} = 2\sigma(\langle c_B \rangle) = 2\sqrt{\frac{\langle c_B \rangle (1 - \langle c_B \rangle)Q}{N}}$$

with $N(r)$ and N being the total number of atoms in spherical layer bounded by radii r and $r + \Delta r$ and total number of atoms in the analyzed volume, respectively. Q is the detection efficiency of the atom probe.

References

Ant03. C. Antion, P. Donnadieu, F. Perrard, A. Deschamps, C. Tassin, A. Pisch, *Acta Materialia*, **51**(18):5335 (2003).

Bas95. P. Bas, A. Bostel, B. Deconihout, D. Blavette, *Applied Surface Science*, **87-88**:298 (1995), proceedings of the 41st International Field Emission Symposium.

Bem03. E. Bemont, A. Bostel, M. Bouet, G. D. Costa, S. Chambreland, B. Deconihout, K. Hono, *Ultramicroscopy*, **95**:231 (2003).

Bla88. D. Blavette, G. Grancher, A. Bostel, *J. Phys. Colloques*, **49**:C6 (1988).

Bla93a. D. Blavette, A. Bostel, J. M. Sarrau, B. Deconihout, A. Menand, *Nature*, **363**(6428):432 (1993).

Bla93b. D. Blavette, B. Deconihout, A. Bostel, J. M. Sarrau, M. Bouet, A. Menand, *Review of Scientific Instruments*, **64**(10):2911 (1993).

Bla00. D. Blavette, E. Cadel, B. Deconihout, *Materials Characterization*, **44**(1-2):133 (2000).

Bla01. D. Blavette, F. Vurpillot, P. Pareige, A. Menand, *Ultramicroscopy*, **89**(1-3):145 (2001).

Bow94. K. Bowman, M. Miller, L. Shenton, *Applied Surface Science*, **76-77**:403 (1994).

Cer88. A. Cerezo, T. J. Godfrey, G. D. Smith, *J. Phys. Colloques*, **49**:C6 (1988).

Cer98. A. Cerezo, T. J. Godfrey, S. J. Sijbrandij, G. D. W. Smith, P. J. Warren, *Review of Scientific Instruments*, **69**(1):49 (1998).

Cer07. A. Cerezo, P. H. Clifton, S. Lozano-Perez, P. Panayi, G. Sha, G. D. Smith, *Microscopy and Microanalysis*, **13**(06):408 (2007).

Cos05. G. D. Costa, F. Vurpillot, A. Bostel, M. Bouet, B. Deconihout, *Review of Scientific Instruments*, **76**(1):013304 (2005).

Dec94. B. Deconoihout, S. Chambreland, D. Blavette, *Adv. Mater.*, **6**(9):695 (1994).

Dec07. B. Deconihout, F. Vurpillot, B. Gault, G. Da Costa, M. Bouet, A. Bostel, D. Blavette, A. Hideur, G. Martel, M. Brunel, *Surf. Interface Anal.*, **39**(2-3):278 (2007).

Del90. S. Delfino, A. Saccone, R. Ferro, *Metallurgical and Materials Transactions A*, **21**(8):2109 (1990).

DG06. F. De Geuser, W. Lefebvre, D. Blavette, *Philosophical magazine letters*, **86**(4):8 (2006), anglais.

Gau10. B. Gault, M. P. Moody, F. De Geuser, A. La Fontaine, L. T. Stephenson, D. Haley, S. P. Ringer, *Microscopy and Microanalysis*, **16**(01):99 (2010).

Hei03. A. Heinrich, T. Al-Kassab, R. Kirchheim, *Materials Science and Engineering A*, **353**(1-2):92 (2003), 47 th International Field Emission Symposium.

Het91. M. Hetherington, J. Hyde, M. Miller, G. Smith, *Surface Science*, **246**(1-3):304 (1991).

Hon99. K. Hono, *Acta Materialia*, **47**(11):3127 (1999).

Hou10. J. Houard, A. Vella, F. Vurpillot, B. Deconihout, *Phys. Rev. B*, **81**(12):125411 (2010).

Kel07. T. F. Kelly, M. K. Miller, *Review of Scientific Instruments*, **78**(3):031101 (2007).

Mil91. M. Miller, M. Hetherington, *Surface Science*, **246**(1-3):442 (1991).

Mil92. M. K. Miller, *Surface Science*, **266**(1-3):494 (1992).

Mil96. M. Miller, A. Cerezo, M. Hetherington, G. Smith, *Atom Probe Field Ion Microscopy*, volume 52 of *Monographs on the Physics and Chemistry of Materials*, Oxford University Press, Oxford, 1996.

Mil00. M. Miller, *Atom probe tomography*, Springer, New York, NY, 2000.

Mil02. —, *Atom Probe Tomography Plenum Publishers*, New York, 2002.

Mil09. M. Miller, R. Forbes, *Materials Characterization*, **60**(6):461 (2009).

Mul68. E. W. Muller, J. A. Panitz, S. B. McLane, *Review of Scientific Instruments*, **39**(1):83 (1968).

Oka07. H. Okamoto, *Journal of Phase Equilibria and Diffusion*, **28**(4):405 (2007).

Rok62. L. Rokhlin, *Izv. Akad. Nauk. SSSR, Otd. Tekh. Nauk, Met. Toplivo*, **2**:126 (1962).

Sei07. D. N. Seidman, *Annual Review of Materials Research*, **37**(1):127 (2007).

Tay96. J. R. Taylor, *An Introduction to Error Analysis: The Study of Uncertainties in Physical Measurements*, University Science Books, 1996, 2nd edition.

Tso90. T. T. Tsong, *Atom-Probe Field Ion Microscopy*, Cambridge University Press, Cambridge, UK, 1990.

Vau03. D. Vaumousse, A. Cerezo, P. J. Warren, *Ultramicroscopy*, **95**:215 (2003).

Vur00. F. Vurpillot, A. Bostel, D. Blavette, *Applied Physics Letters*, **76**(21):3127 (2000).

3 Atom probe investigation of Mg-Nd and Mg-Y-Nd alloys.

3.1 The binary Mg-Nd phase diagram. Mg-rich side.

3.1.1 Introduction.

Though the age hardening response in Mg-Nd is known for a long time [Nic71], the evolution of Nd solid solubility in Mg is not perfectly established. The Mg-rich region of the Mg-Nd equilibrium phase diagram has been investigated in the 60's [Par57, Dri63]. This work has been recently continued by means of thermodynamic calculations using available experimental data [Del90, Men07]. Despite a substantial effort paid to the investigation of the Mg-Nd phase diagram, one may find a discrepancy between disposal values of maximum solubility at eutectic temperature (Table 3.1.1). Such variations of measured solubility from work to work might be the consequence of a variation in the purity of the starting materials, which was sometimes quite low [Gor05] and which could be the result of contamination of the melt by Mg and Nd reduction of the crucible materials.

Reference	Temperature, °C	Maximum solubility, $at\%(wt\%)$
[Rok62]	552	0.63(3.60)
[Sav58]	-	0.33(1.93)
[Par57]	548	0.10(0.59)

Table 3.1.1: Available information about maximum solubility of Nd in Mg.

The assessed Mg-rich part of the Mg-Nd phase diagram, wherein some phase boundaries appear as dashed lines in [NH88, Oka91, Oka07], shows a negligible equilibrium solid solubility of Nd in Mg. However, this region of the phase diagram is of great interest as it determines for instance the conditions for an accurate homogenization of alloy required for further aging treatments. In addition, by exploring higher supersaturation values in Nd, aging treatments may lead to unusual values of strength because of a finer precipitation.

The aim of this study is to establish experimentally the equilibrium solid solubility of Nd in Mg by direct composition measurements. Beyond the difficulty of establishing a reliable procedure for alloy preparation to assess Nd solid solubility in Mg (e.g. alloy making with pure metals, long time heat treatments, alloy preparation for analysis), the measurement of Nd concentration in the Mg matrix is not straight forward for at least two reasons: *i)* the second phase embedded

in the Mg-matrix might be so finely dispersed that a direct measurement of matrix composition without any convolution with the precipitates is impossible; *ii)* the level of Nd concentration is so low (a few thousands at. ppm) that most of analytical techniques fail. For these reasons, the use Atom Probe Tomography is an excellent alternative. This destructive technique enables the determination of atom positions in a volume of material with a near atomic resolution [Mil02]. Its chemical sensitivity may reach in some cases a few tens of at. ppm and, thanks to the 3D reconstruction, the distinction between matrix and precipitates is possible.

3.1.2 Experimental.

Samples of the binary alloy for this measurements were solution heat treated according to the procedure described in the Section 2.1.2. Then, they were aged (after being encapsulated) at different temperatures (from 400 to 520 °C) for times ranging between 90 and 504 h.

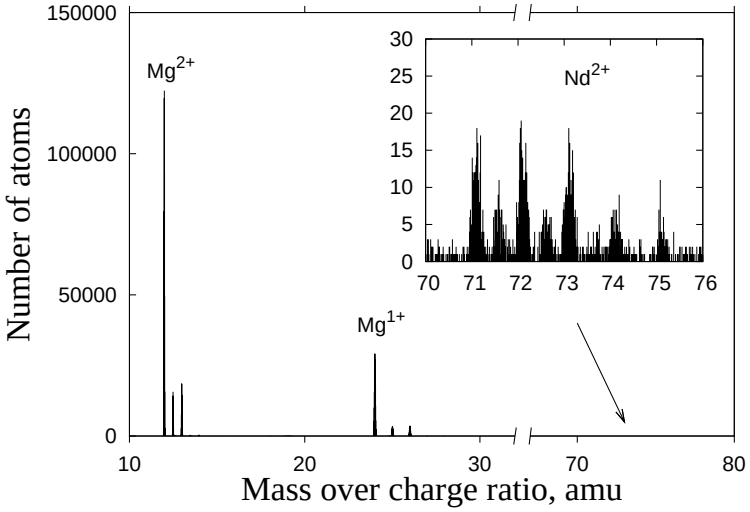

Figure 3.1.1: A typical mass spectrum observed by APT technique for the Mg0.51(at.%)Nd alloys

The APT was carried out on an Energy Compensated Tomographic Atom Probe. A very small proportion of magnesium ($\sim$ 1 *at.*%) was detected in the form of magnesium hydrides. This is extremely common in APT, even for Al-based alloys for which $(AlH)^+$ ions are detected, though this phenomenon does not affect global composition measurement. It must be pointed out that no other peak than those indicted in Figure 3.1.1 was observed. Consequently, one can exclude any detectable presence of impurities.

3.1.3 Results and discussion.

In order to validate our following analysis, the composition of SHT sample was checked and confronted to the nominal one. The value measured in analysis after noise subtraction is equal to $c_{Nd} = 0.49 \pm 0.02$ (at.%), which is in perfect agreement with the nominal composition of the alloy. This result reinforces the chosen experimental conditions. Moreover, since the concentration of the matrix is equal to the nominal one, this indicates that no precipitation of a second phase occurs at 545°C.

The isothermal aging at 400, 480 or 520°C, leads to the precipitation of an Nd-rich equilibrium phase. As the formation of the second phase proceeds, the matrix concentration is expected to converge asymptotically to its equilibrium value equal to the solid solubility at the given temperature. If one measures the matrix concentration after an infinite time of aging, he will therefore find a value of the equilibrium solid solubility. Since infinite time is obviously non attainable experimentally, hypothesis has been made that aging times and temperatures were large enough to allow complete transformation of the supersaturated solid solution. As shown by Figure 3.1.2 and Table 3.1.2, the asymptotic regime appears to be reached. For all counts on the time-scale, the composition remains stable in the range of experimental error. This is not surprising insofar as very long aging times were applied, therefore enabling a nearly complete transformation of the alloy even for the shortest time.

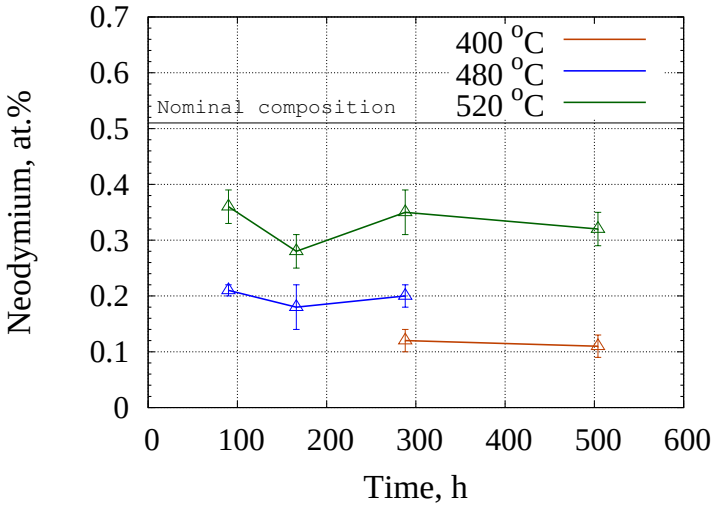

Figure 3.1.2: The measured composition evolution of samples aged at different temperatures.

As a second hypothesis, Gibbs-Thomson's effect has been neglected. This effect may lead

to an overestimation of matrix concentration if second phase precipitates are small with curved interfaces. However, precipitates formed at high temperature are not of this kind. In the binary Mg-0.50%(at.)Nd alloy, Pike and Noble [Pik73] observed irregularly shaped big particles rarely distributed after aging at 350°C for 30 min. Despite the fact that authors of that work identified those precipitates as $Mg_{12}Nd$ phase, which according to modern data was metastable, we believe that the stable $Mg_{41}Nd_5$ phase particles would have the same properties. It means, that we expected the formation of comparably large-scale precipitates separated by relatively big distances.

The latter has been indirectly confirmed by the fact that in our APT analysis, the measured concentration was lower than the nominal composition of alloy. Moreover, the distribution of solutes was homogeneous through all analyzed volumes and no precipitates or Nd-rich zones were detected. Taking into account the mean total analyzed volume ($\sim 15 \times 15 \times 100$ nm^3) achievable for the used technique, the number density of precipitates must be less than $4.5 \cdot 10^{22}$ m^{-3}. It appears then reasonable to conclude that investigated samples are in late stages of the kinetic and that the Gibbs-Thomson effect can be neglected.

T, °C	Time, hours				Estimated c_{Nd}^{eqv}, at.% (wt.%)
	90	166	288	504	
	c_{Nd}, at.% (wt.%)				
400	-	-	0.12±0.02 (0.71±0.12)	0.11±0.02 (0.64±0.12)	0.11±0.02 (0.64±0.12)
480	0.21±0.01 (1.23±0.06)	0.18±0.04 (1.06±0.23)	0.20±0.02 (1.18±0.12)	-	0.20±0.02 (1.18±0.12)
520	0.36±0.03 (2.10±0.18)	0.28±0.03 (1.64±0.18)	0.35±0.04 (2.04±0.23)	0.32±0.03 (1.87±0.18)	0.32±0.03 (1.87±0.18)

Table 3.1.2: Concentration of Nd in the Mg matrix for different aging times and temperatures.

Then, we accept these stable values as the solubility limits of Nd in Mg for the different temperatures investigated. The obtained values of Nd solubility in Mg were plotted on the temperature-concentration plane presented in Figure 3.1.3 and confronted to the only previous available experimental measurements provided by Rokhlin [Rok62] thanks to resistivity measurements.

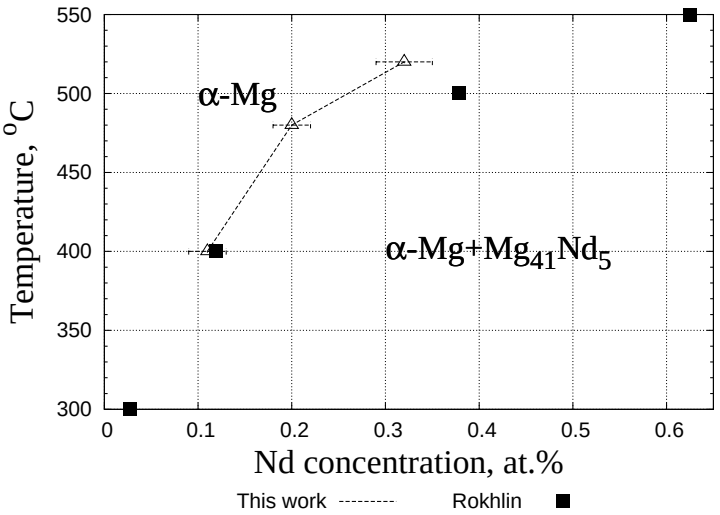

Figure 3.1.3: The determined phase boundary of the binary Mg-Nd alloy. The solid line corresponds to the values obtained in current study; the black squares correspond to values measured in [Rok62].

In all available thermodynamic calculations the solubility of Nd in magnesium supposed to be zero [Gor05, Men07]. The latter reflects rather the lack of reliable experimental data. In the work by Rokhlin [Rok62], the solubility of neodymium (and cerium) in magnesium was investigated by measuring the resistivity of alloys of various composition and aged at various temperatures. The solubility of an element was determined from the kink on the curve describing the dependence of resistivity versus the composition. As it is seen from Figure 3.1.3, our results are quite close to those obtained by Rokhlin, though our study indicates a slightly lower solubility of Nd with increasing temperature. However, a major result provided by our work is the confirmation that the solubility at eutectic temperature is much higher than the value of Park and Wyman [Par57] ($\approx 0.1 at.\%$) normally cited in the literature.

3.1.4 Conclusions.

We have assessed experimentally the high temperature solid solubility limit of Nd in Mg by means of Atom probe Tomography. Thanks to its high sensitivity, this technique has enabled reproducible measurements of Nd content in the Mg-matrix. This experimental work provides a clarification on the Mg-rich part of the Mg-Nd phase diagram. The results presented in this study should help for the extraction of thermodynamic quantities of the Mg-Nd system and for modification of the Mg-Nd binary phase diagram.

This work has been accepted as a publication in *Journal of Phase Equilibria and Diffusion.*

3.2 Characterization of precipitates in binary Mg-Nd alloy aged at 190°C for 24 hours.

In this section we make an attempt to describe the main ideas, methods and protocols which were used for the characterization of the Mg-alloys of interest. Moreover, attention will be paid to problems which appear during the investigations of those Mg alloys by the Tomographic atom probe technique. Solutions for these problems will be proposed here.

The atom probe data treatment is given in this section on the example of the binary Mg-Nd alloy homogenized according to the procedure described in the Section 2.1.2 and annealed for 24 hours at 190°C. This type of heat treatment was used by Pike and Noble [Pik73] in their TEM investigation of precipitation sequence of Mg-Nd alloy. It has been reported at these conditions the formation of well developed nano-scale coherent precipitates with DO_{19} crystallographic structure. The results of Pike and Noble are used here for the explanation of microstructure observed by atom probe in the alloy of the same composition and heat treatment.

3.2.1 APT reconstruction parameters.

As it was already mentioned before, in a first approximation, APT can be considered as a point projection microscope. In this simple model the selection of compression factor β (see Section 2.2.1 for the definition) for the successful reconstruction of an analyzed volume is of major importance for further data treatments.

When a sample is analyzed with a tomographic atom probe in the vicinity of a low Miller index pole, the reconstructed volume exhibits the trace of atomic planes. If one is able to index the pole (and, hence, the planes), then he knows the real inter-plane spacings. Adjusting the observed inter-plane spacings to the real ones by playing with the reconstruction parameters, one can find an appropriate set of those parameters. This method was used in the current work.

According to Miller [Mil02] in a material with *hcp*-lattice, the poles with indexes $\{0002\}$, $\{10\bar{1}0\}$ and $\{11\bar{2}0\}$ are the "strongest", as the planes corresponding to those poles have the biggest interplane distances. If the investigated sample is orientated in such a way that direction of analysis is close to a pole direction, it is likely to observe the atomic planes corresponding to the pole.

Moreover, crystallography also affects ion trajectories along field lines. As suggested by Waugh

et.al [Wau76], the so-called roll-up motion or movement of atoms about to field evaporate and influence by neighboring atoms on the tip surface can give rise to variations of the impact density at crystallographic poles and depleted/dense zone lines along major crystallographic planes. These heterogeneities help to index a pole near which they were found.

In Figure 3.2.1a, a slice of analyzed volume of a Mg-Nd alloy sample normal to the direction of analysis is shown. The magnesium atomic density forms a flower-type pattern near a pole.

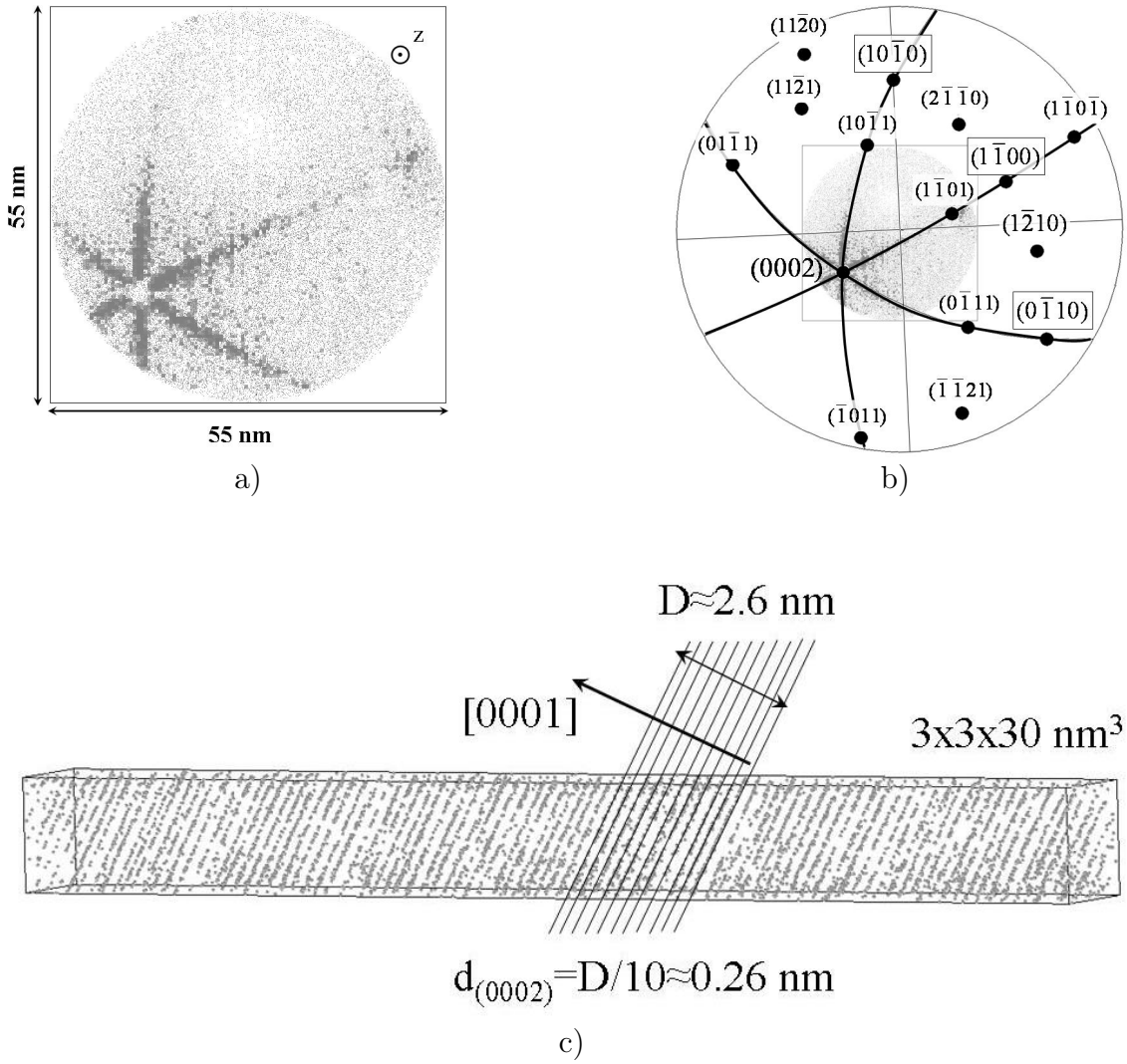

Figure 3.2.1: a) Field-desorption image formed by pulsed-field-evaporation of Mg atoms from a needle-shaped specimen during APT analysis. Zones of elevated atomic density are shown. b) Superposition of the observed field desorption image and stereographic projection generated for *hcp* magnesium matrix. c) Visualization of atomic planes observed inside (0002)-pole with inter-plane distance adjusted to the right value ≈ 0.26 nm typical for Mg-lattice.

The ideal superposition of the observed pattern with the stereographic projection generated for magnesium lattice (Figure 3.2.1b) proves that the observed pole corresponds to the (0002) atomic

plane. The inter-plane distance for these planes in pure magnesium is $d_{(0002)} \approx 0.26$ nm. In Figure 3.2.1c the visualization of planes is given for which the inter-plane distance is set approximately equal to 0.26 nm by adjusting the parameters of APT reconstruction: the magnification M and geometrical factor β. The adjusted values can be now used for other APT reconstructions, as they are believed to remain constant for the same type of material and atom probe device.

It is worth noting that in this experiment the (0002) planes are thin and well spaced only in the center of their pole. With moving away from the pole, thin planes start to overlap (Figure 3.2.2), forming thick two-plane traces separated by approximately double distance. This phenomenon did not find any explanation, but seems to be very general in APT experiments on Mg systems (see, for example [Pin03]).

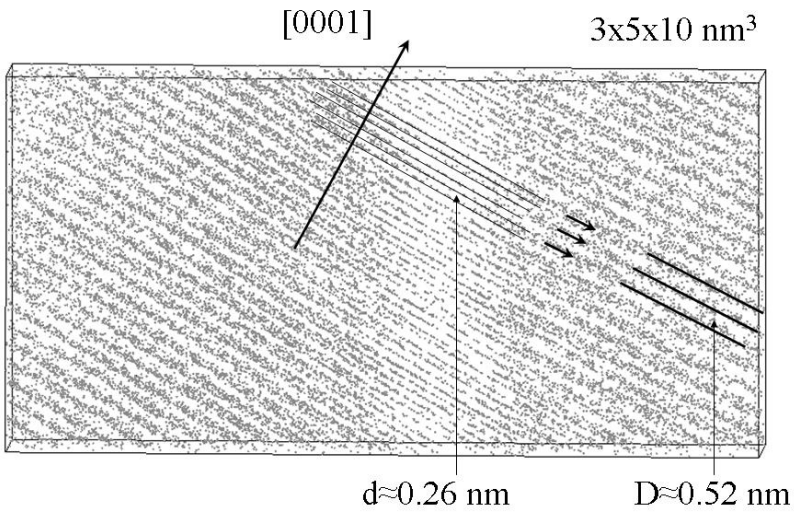

Figure 3.2.2: Visualization of atomic planes observed for the (0002)-pole. The reconstruction (or evaporation) artifact is observed leading to the mixing of single basal planes of *hcp*-lattice and formation of thick planes separated by double distances.

The appearance of "thick" planes separated by approximately $D \approx 0.52$ nm near the border of the reconstructed volume (when (0002) pole is not visible) often gives the idea about relation between analysis direction and [0001] direction in the *hcp*-lattice.

3.2.2 Precipitate orientation relationships.

In the literature review (Section 1.2) it was mentioned that precipitates in Mg-RE alloys have some specific orientation relationships. When crystallographic directions in a specimen analyzed by APT can be identified, one can also make an analysis of precipitate crystallographic orientations.

In Figure 3.2.3 a part of reconstructed volume with a family of Nd-rich precipitates is shown. The volume oriented in a specific direction reveals angle relationships between plate-like precipitates. It is seen, that these precipitates have the angle approximately equal to 120° between them.

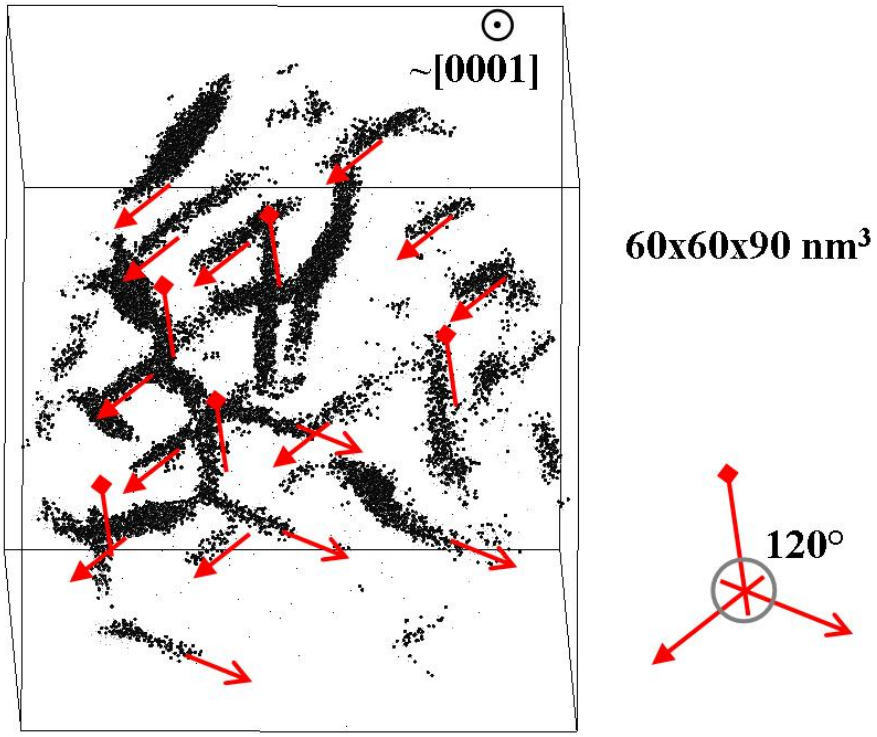

Figure 3.2.3: Precipitate angle relationships observed in the sample oriented in such a way that zone axis is approximatelly equal to [0001].

Poles and planes observed in APT analysis occur to be useful for the determination of crystallographic orientation relationships of the precipitates. The usage of these information is shown in Figure 3.2.4.

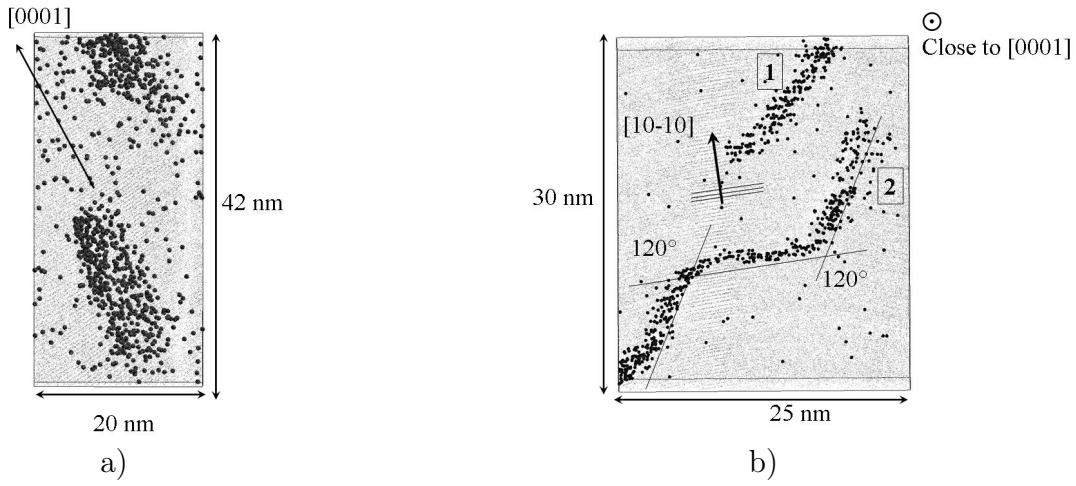

Figure 3.2.4: Thin slices of reconstructed volumes ($\sim$ 3 nm in depth) demonstrating a) the elongation of precipitates along [0001] direction and b) precipitate habit plane found to be equal to $\{10\bar{1}0\}$. Mg atoms are shown as gray points; Nd atoms are black spheres.

From Figure 3.2.4a, it is seen that the precipitates are elongated along the [0001] direction of the Mg *hcp* lattice, whereas Figure 3.2.4b provides the information about habit plane of one of the observed precipitates. Three interconnected precipitates marked by number **2** are orientated with respect to one another under the angle of 120°. One of those three precipitates (in the middle) is obviously perpendicular to the $[10\bar{1}0]$-direction of the *hcp*-lattice, hence, its habit plane is $(10\bar{1}0)$. The right and left precipitates also lay in planes from $\{10\bar{1}0\}$-plane family. The latter can be concluded from the fact that the direction of view corresponds to the [0001]-lattice direction and the angle equivalent to 120° in this case transforms one plane from $\{10\bar{1}0\}$ family into another. The habit plane of precipitate marked by number **1** was not found in this case.

An idea about habit planes for precipitates can be also found using traces formed by field desorption images. This is demonstrated in Figure 3.2.5. This technique is more sophisticated and needs some additional explanations.

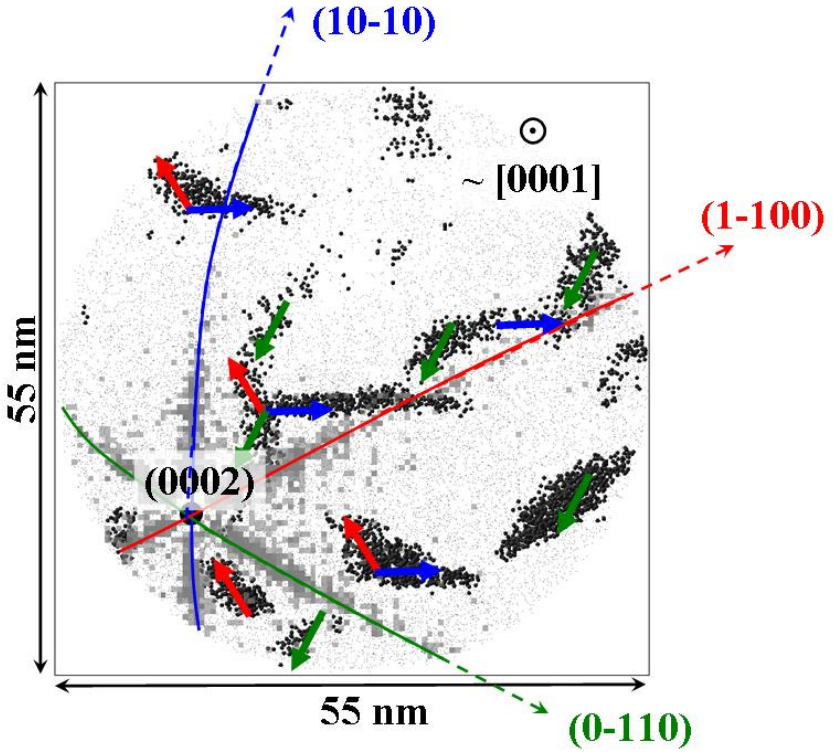

Figure 3.2.5: Field-desorption image with high atomic density lines pointing the traces of $\{10\bar{1}0\}$-poles and Nd-rich plate-like precipitates oriented perpendicular to the observed crystallographic directions, proving the $\{10\bar{1}0\}$-planes to be the habit ones.

In Figure 3.2.5, one can see Nd-enriched precipitates (Nd atoms are shown in black) orientated in different directions together with gray traces corresponding to zones of elevated atomic density. The traces intersect in a pole. According to indexation given in Figure 3.2.1b) the pole has been identified as (0002). By-turn, lines connect the poles $\{0002\}$ and $\{10\bar{1}0\}$, thus they are traces of $\{10\bar{1}0\}$-poles. They can serve as an indication of $\langle 10\bar{1}0\rangle$ directions in the analyzed specimen. It is seen that most of the precipitates are approximately perpendicular to the traces, i.e. perpendicular to the identified directions. Therefore, the habit planes for those precipitates should be from the $\{10\bar{1}0\}$ family.

Figure 3.2.4b) and Figure 3.2.5 demonstrate that there are precipitates for which habit plane is found to be from the $\{10\bar{1}0\}$-plane family. This agrees well with the findings made in other works [Gra70, His02, Wil03] devoted to the study of binary Mg-Nd system. However, in Figure 3.2.4b) and Figure 3.2.5 there were found some precipitates, for which it was not possible to claim if $\{10\bar{1}0\}$ is their habit. This could occur either because there exist precipitates with other crystallographic orientations or due to somewhat inexact orientation of the analyzed volume. Certain APT artifacts

leading to the loss of crystallographic information cannot be also discarded. As initially APT technique was developed for the investigation of concentration inhomogeneities in different types of materials, its usage for the acquisition of crystallographic information is limited.

According to Pike and Noble [Pik73] after the heat treatment applied to the investigated specimen, thin plate-like coherent DO_{19} precipitates should form. The stoichiometric composition of a bulk fully ordered DO_{19} precipitate is expected to be A_3B. However, the concentration in a profile across an observed precipitate is too low in comparison with the one expected for the DO_{19} superstructure (see for example concentration profiles provided in Figure 3.2.6).

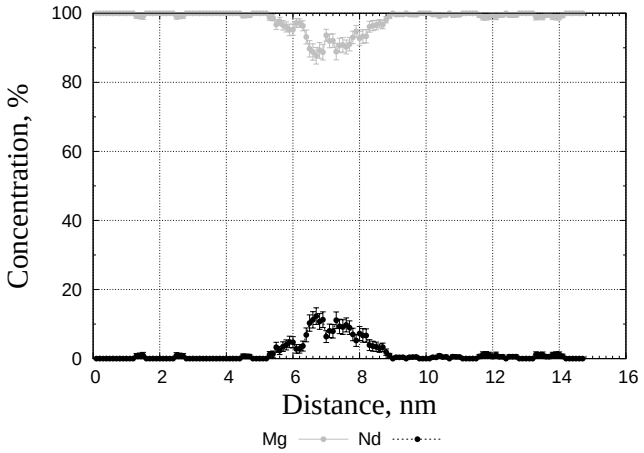

Figure 3.2.6: Typical Concentration profile across a typical precipitate observed in the Mg-Nd alloy aged at 190°C for 24 h.

We explain the significant decrease in precipitate concentration by mixing of atoms near precipitate interfaces caused by i) the limit in spacial resolution of APT and ii) the local magnification effect. Obviously, for the plate-like precipitates the mixing is of major importance near the interfaces bounding thin precipitate sides.

3.2.3 Spacial resolution and its effect on the precipitate composition.

In order to check the effect of the limited spacial resolution, simple simulations have been performed. We started from the undistorted ideal *hcp*-lattice and a perfectly ordered one-plane precipitate embedded in it and surrounded by pure matrix (Figure 3.2.7a). The shown precipitate lies on the $(10\bar{1}0)$ matrix plane. However, it should be emphasized that in the present model an orientation of precipitate as well as an assumption of pure matrix results in no loss of essential characteristics and does not change the final conclusion.

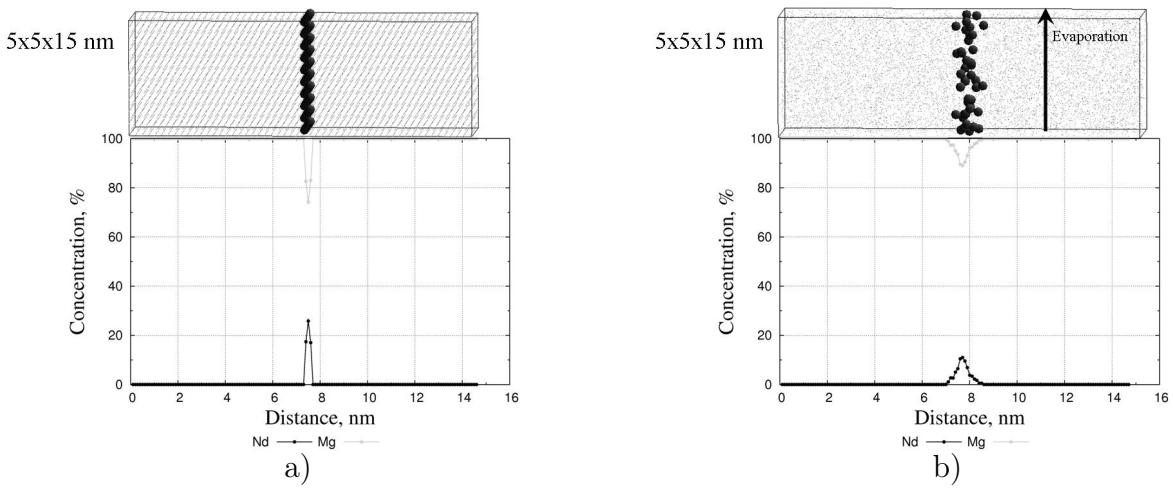

Figure 3.2.7: A one-plane precipitate and the concentration profile across disturbed volume. The parameters of shift are: $\sigma_\perp = 0.3$ nm, $\sigma_{||} = 0.1$ nm, $Q = 0.6$.

Now, if one measures the concentration profile across the precipitate, he will obtain the peak 25 % of solute concentration in the place of precipitate location, which is the real value. Then atoms are allowed to change their positions in such random way to take into account the error made by APT analysis and reconstruction due to its limited spacial resolution. It is well known, that the resolution in the direction of analysis (depth resolution) is close to the atomic resolution, whereas the resolution in perpendicular direction (lateral resolution) is worse. Due to the anisotropy of the APT's resolution, the shift of atoms is performed according to the following algorithm: an atom shifts in the evaporation direction respecting the shifts distribution

$$P_{||}(z) = \frac{1}{\sigma_{||}\sqrt{2\pi}} \exp\left(\frac{(z-\sigma_{||})^2}{2\sigma_{||}^2}\right)$$

and in the mean time in the perpendicular direction —

$$P_{\perp}(\rho) = \frac{1}{\sigma_{\perp}\sqrt{2\pi}} \exp\left(\frac{(\rho-\sigma_{\perp})^2}{2\sigma_{\perp}^2}\right)$$

where $\sigma_{||}$ and $\sigma_\perp$ correspond to the depth and lateral resolutions, respectively. Their typical values are $\sigma_{||} = 0.1$ nm and $\sigma_\perp = 0.3$ nm. In addition, an atom is thrown out with the probability $1-Q$, where $Q < 1$ is the detection efficiency of a tomographic atom probe. The typical detection efficiency is equal to 60%.

In Figure 3.2.7b, the result of the simulation is presented for the case when the direction of

analysis is parallel to the precipitate habit plane. This time the profile concentration measured across the disturbed precipitate shows a significant decrease from initial 25% to final $\sim$ 15% value. In addition we have an appreciable virtual widening of our precipitate. This case corresponds to the "worst case", when the angle, θ, between precipitate habit plane and the direction of APT analysis is equal to 0. In general, θ takes any value from interval $0..\pi/2$, and, thus, the effect of mixing due to the limited spacial resolution depends on precipitate orientation.

The formation of some agglomerates of ordered one-plane precipitates separated by 3 pure Mg atomic layers in a (quasi-)ternary Mg-Y-Nd system was reported [Ant03]. This is probably also the case for binary Mg-Nd alloy. To analyze the transformation of a such agglomerate after an APT analysis, a sequence of three one-plane DO_{19} precipitates was generated, Figure 3.2.8a. After the shifting procedure described above, this agglomerate transforms into thick precipitate with the concentration significantly lower than the initial one (Figure 3.2.8b)) .

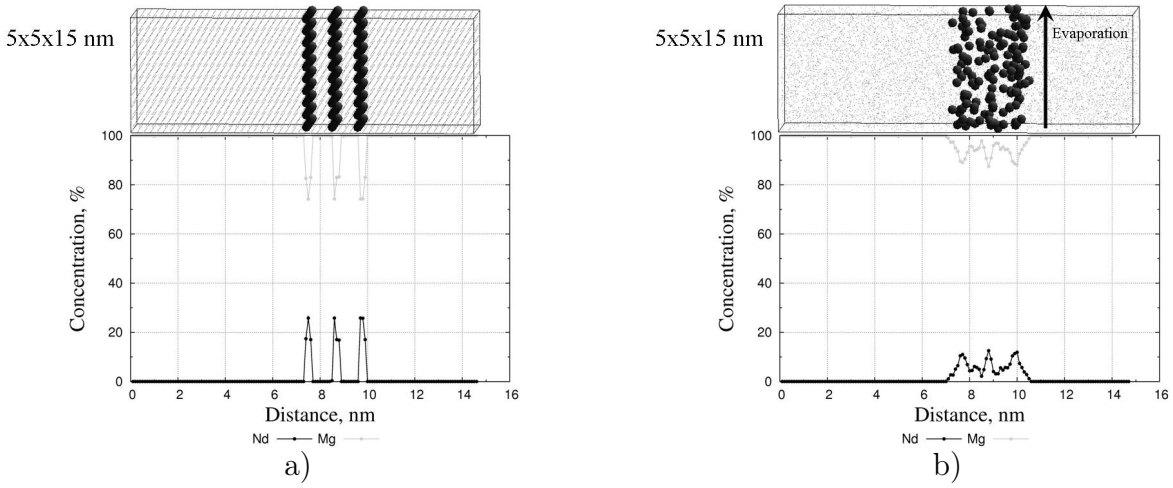

Figure 3.2.8: An agglomerate of three ordered one-plane precipitates and the concentration profile across disturbed volume. The parameters of shift are: $\sigma_{\perp} = 0.3$ nm , $\sigma_{||} = 0.1$ nm, $Q = 0.6$.

Of course, the real situation might be much more complex, as, for example, we don't take into account, non-zero solute matrix concentration. But in the mean time, the described model does not claim to be exhaustive and is rather qualitative.

3.2.4 Local magnification effect and its effect on the precipitate composition.

The local magnification effect leads to the mixing of matrix atoms with the ones from precipitates. Of course, it is necessary to take this mixing into account when calculating precipitate

concentrations and (atomic) volume fractions. But first, it would be useful to find out if considered precipitates of the second phase are low-field or high-field ones.

In theory, it can be done by several methods:

- the field-ion microscopy can give the answer to this question by showing the precipitates as either dark spots or bright spots on the background of matrix in case of either low-field or high-field precipitates, respectively.

- in case of different fields of evaporation of precipitate and matrix atoms, the distribution between charge states of ions has to exhibit difference for ions evaporated from matrix and precipitates: if one element is considered, when precipitate atoms evaporate at higher field than matrix ones (high-field precipitates), then they should contain higher charge states of ions, and vice versa. In principle, the ratio between number of ions of different charge states might give according to Kingham [Kin82] the fields of evaporations both matrix and precipitate atoms.

- as it was shown in Figure 2.2.4 the image of low-field precipitates has to become compressed whereas for the high-field ones a depleted zone forms close to the interface. Therefore, visual inspection is able to answer the question whether the precipitates are low-field or high field ones.

The FIM technique comes to be very tricky for usage in present case because of low evaporation field of Mg. The FIM analysis could not be performed in the framework of the present work due to impossibility to introduce the hydrogen as an imaging gas into the FIM system.

The distribution of charge states of atoms in the matrix and precipitates are presented in Table 3.2.1. It is seen that there exists some difference between distribution of single- and double-charged Mg ions from detected in precipitates and in the matrix. The percentage of double charged ions evaporated from precipitates is higher, making the assumption about high evaporation field of secondary phase grounded.

Matrix		Precipitates	
Mg^{+}, %	Mg^{2+}, %	Mg^{+}, %	Mg^{2+}, %
85.00 ± 0.02	15.0 ± 0.02	80.82 ± 0.09	19.2 ± 0.09

Table 3.2.1: Relative distributions of single- and double-charged states of Mg-atoms associated with precipitates and the matrix measured in a Mg-Nd alloy sample aged at 190°C for 24 h.

The number of detected ions per unit volume, latter named atomic density, globally (measured in a whole reconstructed volume) has some constant value, associated to the real atomic density of an analyzed material and normalized by the detection efficiency of an Atom probe. Locally, however, the atomic density may be (and indeed is) inhomogeneous. The inhomogeneity appears in a vicinity of crystallographic poles and other special crystallographic zones (Figure 3.2.1b), as well as in a vicinity of precipitates having an evaporation field different from that of the matrix (Figure 2.2.4). In Figure 3.2.9, the depletion in atomic density near an Nd-rich precipitate formed in the investigated sample is revealed, which is a typical indication that the precipitate is a high-field one. In addition, the fluctuation of atom density is also illustrated in Figure 3.2.9. Observed depletion in atomic density near precipitate is typical for all APT analysis of Mg-alloys containing precipitates. Latter, to our opinion, proves that the precipitate atoms need a higher field for evaporation in comparison to matrix ones.

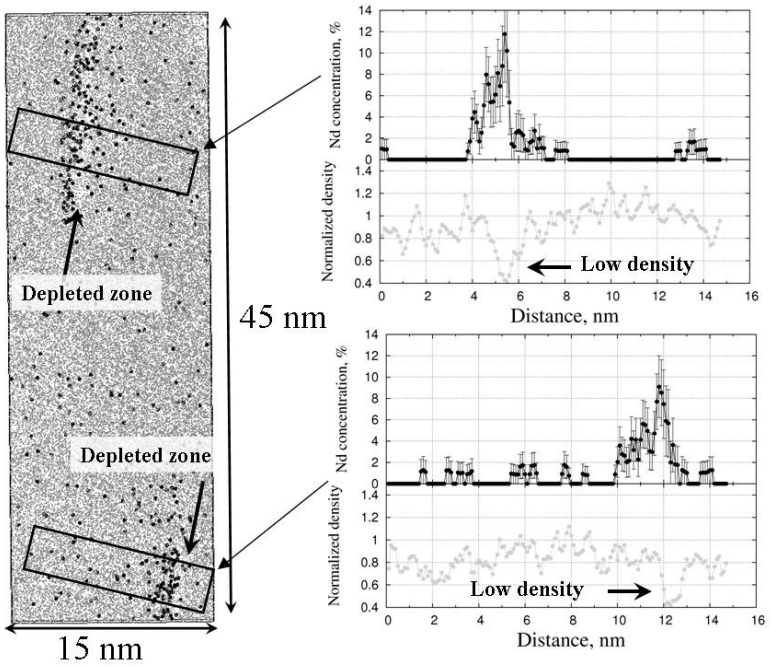

Figure 3.2.9: "Atomic density holes" observed near Nd-rich precipitates indicating about high field of evaporation of precipitate atoms in comparison to the matrix ones. Mg atoms are shown as gray points; Nd atoms are black spheres.

Crucial problems interfering from the investigation of two-phase samples essentially come from the aberrations in the ion trajectories, notably in the close vicinity of interfaces. An important artifact revealed by Figure 3.2.9 is the *delocalization* of precipitates after field evaporation. This delocalization gives rise to biased compositions particularly for nano-scale plate-like particles like

those observed in a Mg-Nd alloy, which have another evaporation field than the surrounding matrix. In the next section, possible procedures for the correction for precipitate concentrations and atomic fractions are discussed.

3.2.5 Precipitate concentration and atomic fraction.

It was shown that due to the limited spacial resolution and first of all due to ion trajectory aberrations, an overlap between matrix and precipitate atoms happens. In this case, the concentration of precipitates in principle becomes biased and should be corrected.

In the literature different methods for concentration correction were discussed and applied [Vur00, Geu05]. The main idea is to separate the mixed atoms, those which initially contributed to a precipitate and those which were in the matrix, and move them on initial positions. Here, we apply a version of correction procedure initially proposed by De Geuser [Geu05] and successfully applied in the work of Hasting et al. [Has09].

Let us consider a plate-like solute-rich precipitate embedded into the pure matrix. In a reconstructed volume, as it was shown above, the concentration profile across the smallest precipitate's dimension will give some value for solute concentration, which is normally lower than the real one because of mixing of atoms caused by the local magnification effect and spatial resolution.

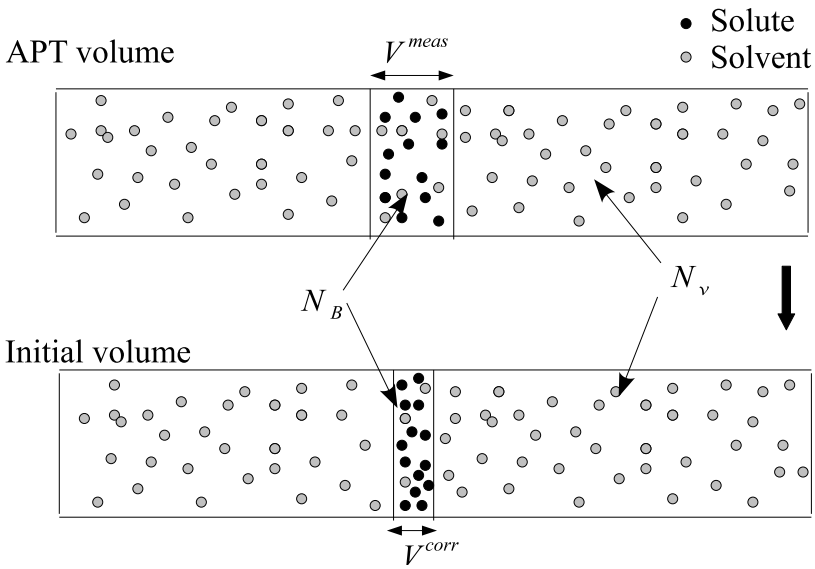

Figure 3.2.10: Schematic description of the concentration correction method applied to thin plate-like precipitates.

In order to perform a correction, let us suppose that all solute atoms, N_B, found in the volume V^{meas} initially occupied a smaller volume, V^{corr}. In order to calculate the corrected concentration, c^{corr}, we divide the number of solute atoms, N_B, by the total number of atoms, N^{total}, which should have been found in the volume V^{corr}. The value of N^{total} can be determined from the atomic density, N_ν, as follows $N^{total} = N_\nu V^{corr}$. The procedure is schematically illustrated in Figure 3.2.10.

Thus, the corrected concentration is given by simple formula: $c^{corr} = N_B/(N_\nu V^{corr})$. The atomic density, N_ν, should be measured in a precipitate free zone relatively far from a pole in order to avoid possible errors.

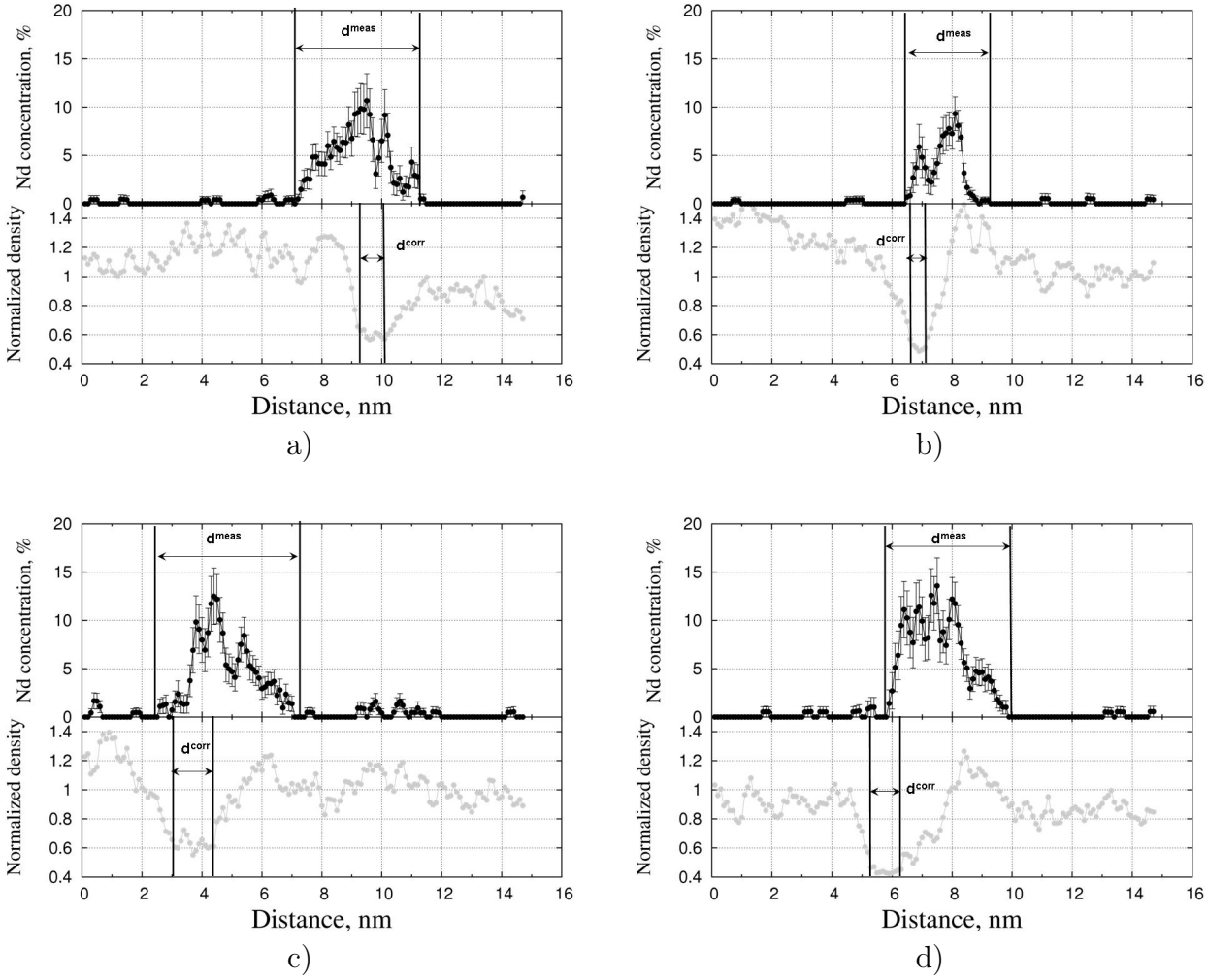

Figure 3.2.11: Concentration profiles and corresponding atomic densities taken from four different precipitates observed in a APT-reconstructed volume. The dimentions of the boxes were equal to $5 \times 5 \times 15$ nm^3.

In this method, the main question is how to determine the initial value of precipitate volume,

V^{corr}. It was shown earlier, that the local magnification effect in addition to atomic mixing causes the formation of atomic density inhomogeneities, i.e. holes in atomic distribution near precipitates. So, it would be natural to suppose, that undisturbed precipitate initially occupied the volume corresponding to the atomic density hole visible in the reconstruction. The realization of this idea is illustrated in the Figure 3.2.11, where correction procedure is applied for several precipitates.

Using this method of correction one might emphasize two main sources of errors for the measured precipitate concentration: i) the standard statistical error, Δ_c, ii) the error, Δ_d, which comes from the uncertainties on the determination of corrected precipitate thickness. The statistical error is given by formula

$$\Delta_c = 2\sqrt{\frac{c^{corr}(1-c^{corr})Q}{N^{total}}}, \tag{3.2.1}$$

where N^{total} is the total number of atoms in the volume V^{corr}, c^{corr} corrected concentration and $Q = 0.6$ is the detection efficiency of atom probe. By-turn, the error Δ_d is calculated as follows

$$\Delta_d = c^{corr}\frac{\Delta d}{d^{corr}}, \tag{3.2.2}$$

where Δd is the systematic error coming from the measurement of d^{corr}. Typical value of Δd is equal to 0.1 nm. Total error made on concentration should be, then, estimated as follows:

$$\Delta_{tot} = \sqrt{\Delta_d^2 + \Delta_c^2}. \tag{3.2.3}$$

The results of the correction procedure applied to the precipitates for which profiles are given in Figure 3.2.11 are presented in Table 3.2.2.

Figure	N_ν, nm^{-3}	d^{meas}, nm	c^{meas}, %	d^{corr}, nm	c^{corr}, %
3.2.11a	28	4.5	4.3	1.0	18.3 ± 3.0
3.2.11b	31	3.0	3.4	0.6	15.3 ± 3.6
3.2.11c	27	5.0	4.1	1.2	15.7 ± 2.4
3.2.11d	28	4.0	6.5	1.0	21.7 ± 3.3

Table 3.2.2: Results of the composition correction procedure for the four precipitates, whose composition profiles are presented in Figure 3.2.11.

It is worth noting that applied correction procedure significantly changes the precipitate composition as it is seen from comparison of columns c^{meas} and c^{corr} of Table 3.2.2. Still the corrected

concentration differs from that expected for the bulk $D0_{19}$ phase and one sees that its value deviates depending on analyzed precipitate. There may be proposed two explanations: i) the investigated phase is metastable, hence, the composition of precipitates may be out of stoichiometry; ii) the structure of the precipitates may be complicated as it was discussed by Hisa et al. [His02] for Mg-Ce alloy, where ordered two-dimensional precipitates had stepped quasi-DO_{19} structure.

Together with precipitate (and matrix) concentration, the precipitate volume fraction (defined as the part of sample volume occupied by precipitate phase) is used for the characterization of the decomposition stage of an alloy. When precipitate and matrix atoms have the same atomic volumes, the apparent precipitate volume fraction is equal to the precipitate atomic (molar) fraction, defined as number of precipitate atoms divided by total number of atoms detected in the volume. However, due to the local magnification effects, precipitates appear in reconstructed images with a much different volume than expected (i.e. high-field precipitates are expended in a reconstructed volume), thus, the apparent atomic (molar) fraction is not to be mistaken with the apparent volume fraction.

It is obvious that the measured (i.e. without correction) value of atomic fraction, f', of the precipitate phase is biased. However, the true fraction, f, (in contrast to the volume fraction) can be easily deduced from the values of measured,$c_B^{\prime prec}$, and corrected precipitate compositions, c_B^{prec}:

$$f = f' \frac{c_B^{\prime prec}}{c_B^{prec}}, \tag{3.2.4}$$

with f' being the measured value of atomic fraction.

It is demonstrated above, that well-developed precipitates in the binary Mg-Nd system are planar, with the smallest direction, which does not exceed the size of 2 nm. Moreover, a significant influence of the local magnification effect on the concentration and size of precipitates is noted. The specific shape of precipitates accompanied with the influence of local magnification effect makes impossible an accurate determination of precipitate boundaries by the cluster identification algorithm (Section 2.3.1). The solute atoms (Nd) from precipitates are usually identified correctly, whereas a large part of magnesium atoms from the matrix become associated to precipitates. That is why the following sections, instead of precipitate atomic fraction, we will mainly use another characteristic named solute fraction, f_s. It is defined as fraction of solute atoms involved into

precipitation:

$$f_s = \frac{N_s^{prec}}{N_s}, \tag{3.2.5}$$

where N_s^{prec} is the number of solute atoms involved into precipitation and N_s is the total number of solute atoms in the sample. In order to define the error Δf_s, we assume that solute fraction, f_s, is calculated from the equation $f_s = N^{prec}c_s^{prec}/Nc_s$, where c_s^{prec} and c_s are the concentrations of solute atoms in precipitates and in the whole analyzed sample, respectively; N^{prec} and N are the numbers of atoms in precipitates and whole analyzed volume, respectively. It is easy to check that the latter is absolutely equivalent to Eq. 3.2.5. Systematic error made by cluster identification method cannot be properly identified, whereas statistical error in the concentrations usually does not overcome the value $\sim 10\%$. We suppose, that the relative error in values c_s^{prec} and c_s are equal to $\alpha = 10\%$. Then, the value Δf_s is calculated as follows:

$$\Delta f_s = \alpha\sqrt{2} f_s. \tag{3.2.6}$$

3.2.6 Other type of precipitates.

The temperature range for existence of coherent β'' precipitates was suggested by Pike and Noble [Pik73] and claimed to be approximately between 180°C and 260°C. But in some analyses of the sample aged for 24 hours at 190°C, together with thin plate-like precipitates associated with β'' phase, other type of precipitates was found. The illustration is given in Figure 3.2.12.

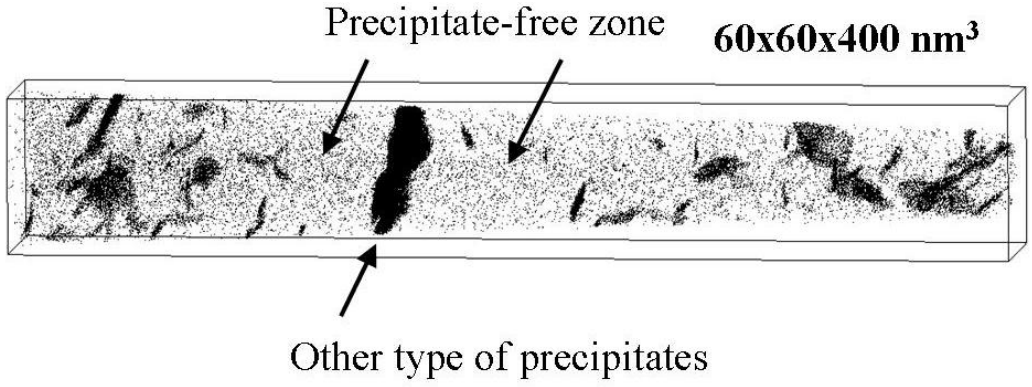

Figure 3.2.12: APT elemental map, showing the distribution of Nd atoms in an analyzed sample. The arrows show location of thick solute-enriched precipitates and solute- and precipitate depleted zones around precipitates.

One can see, that in addition to relatively small precipitates observed at the beginning and at

the end of the analysis, two thick precipitates are visible in the middle. Remarkable feature that in close vicinity of those precipitates other precipitates are almost absent, this forms a precipitate-free zone.

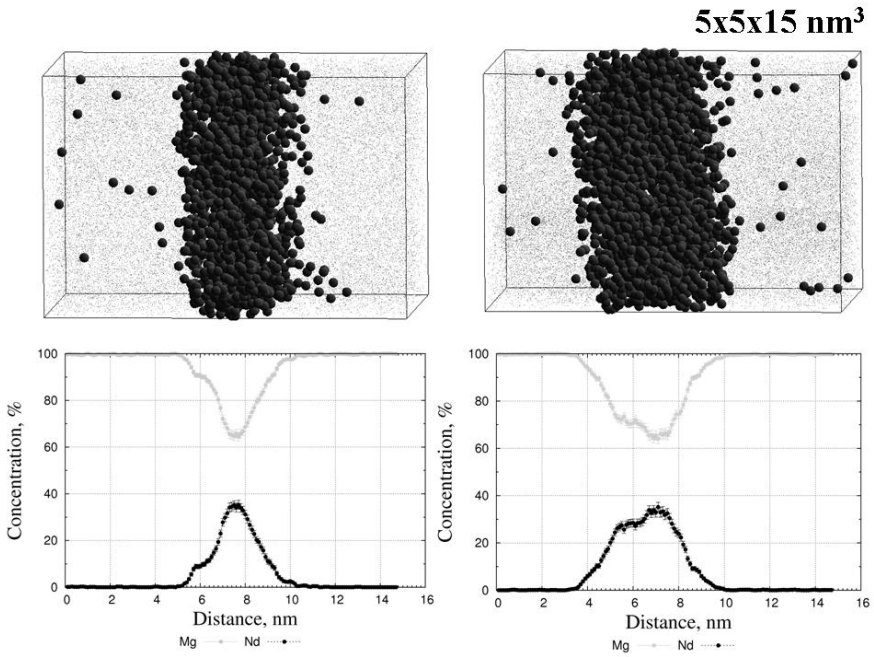

a)

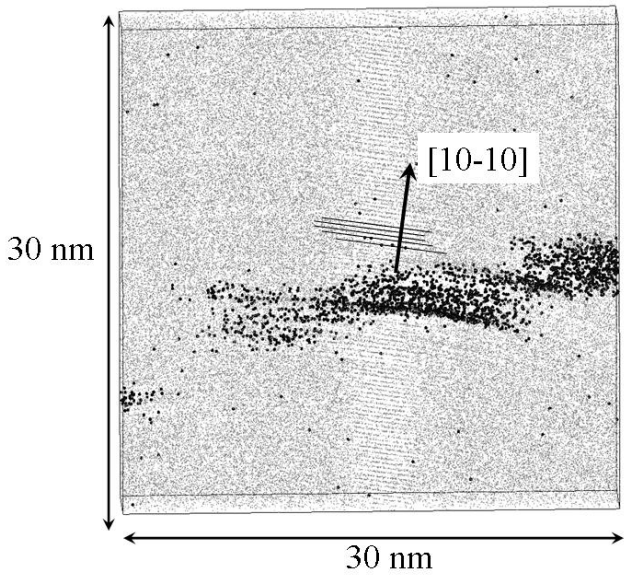

b)

Figure 3.2.13: a) Concentration profile across a thick precipitate demonstrated in Figure 3.2.12; b) a thin slice of the APT-reconstructed volume demonstrating the orientation of the thick precipitates relative to the $[10\bar{1}0]$ direction.

The composition of the big precipitates is much higher than others. The composition profile for

these thick precipitates is given in Figure 3.2.13a together with the indication about the precipitate orientation Figure 3.2.13b.

The high solute content indicates that these are β'-precipitates. The composition of β'-phase formed in binary Mg-Nd alloy initially investigated by Karimzadeh [Kar85] and then reported by Lorimer [Lor86] was found to be equal to Mg_2Nd_{17}, i.e. $c_{Nd} \approx 89\%$. The solute content measured by means of concentration profile (Figure 3.2.13a)) is less than for the suggested phase. However, if the concentration-correction procedures, similar to those described above, are applied, the corrected concentration becomes equal to $c_{Nd} = 79 \pm 8.1\%$. Which is quite close to the value expected for β' phase.

The considered precipitates are quite massive. The thickness of the smallest dimension is about 4 nm. It is worth noting that in this case, the applicability of the correction procedure is arguable. We, then, do not exclude the possibility that the considered precipitates are thick $D0_{19}$ precipitates with the composition $c_{Nd} = 25\%$. The elevated concentration of solute measured by composition profiles of the investigated precipitates (Figure 3.2.13a)) may occur due to the preferential evaporation of low-field Mg-atoms.

However, the probable existence of the β' phase at this temperature of annealing turned out the decision to apply a lower temperature in order to assure the investigation of the precipitation of only β'' phase. The investigation of the kinetics of precipitation in the Mg-Nd binary alloy has been studied for the aging at the temperature equal to 150°C.

3.3 Precipitation kinetics in binary Mg-Nd alloy aged at 150°C.

3.3.1 Results

The temporal evolution of the precipitate morphology of the model Mg-Nd alloy is displayed in a series of $10 \times 10 \times 45$ nm^3 3D-APT reconstructions, each containing approximately 120 thousands atoms (Figure 3.3.1).

Samples aged for 54 and 101 hours at 150°C. At these relatively short times of aging, a high-density distribution of Nd-rich clusters consisting of few tens of solute atoms appears (Figure 3.3.2).

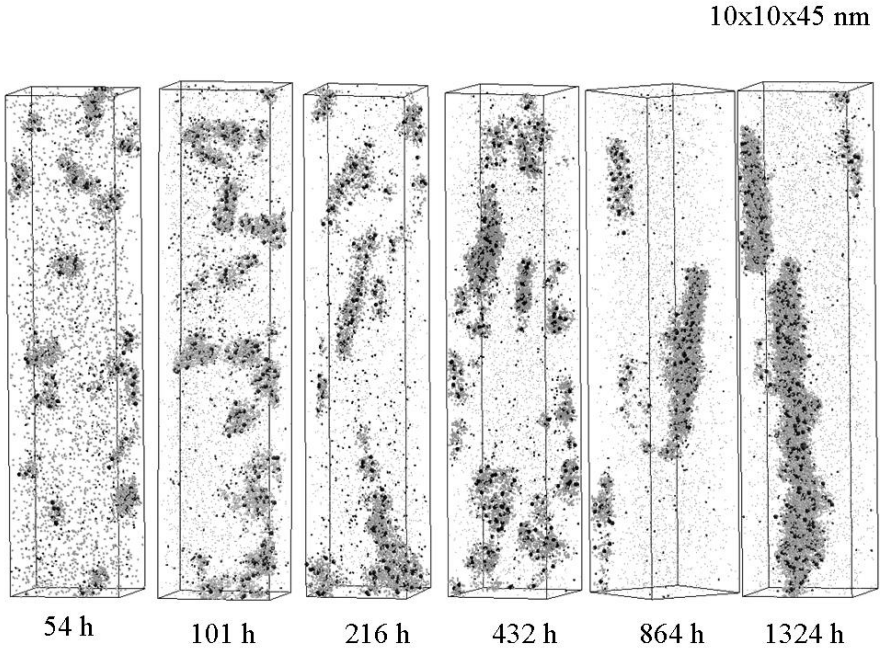

Figure 3.3.1: APT elemental maps of the Mg-Nd alloy aged at 150°C for various times indicated under the corresponding volumes. Nd solute atoms partition to the matrix are shown as small points; Mg solvent atoms are omitted for clarity. The nanometer-sized precipitates are highlighted by using spheres of nonzero radii for solute (black) and solvent (gray) atoms.

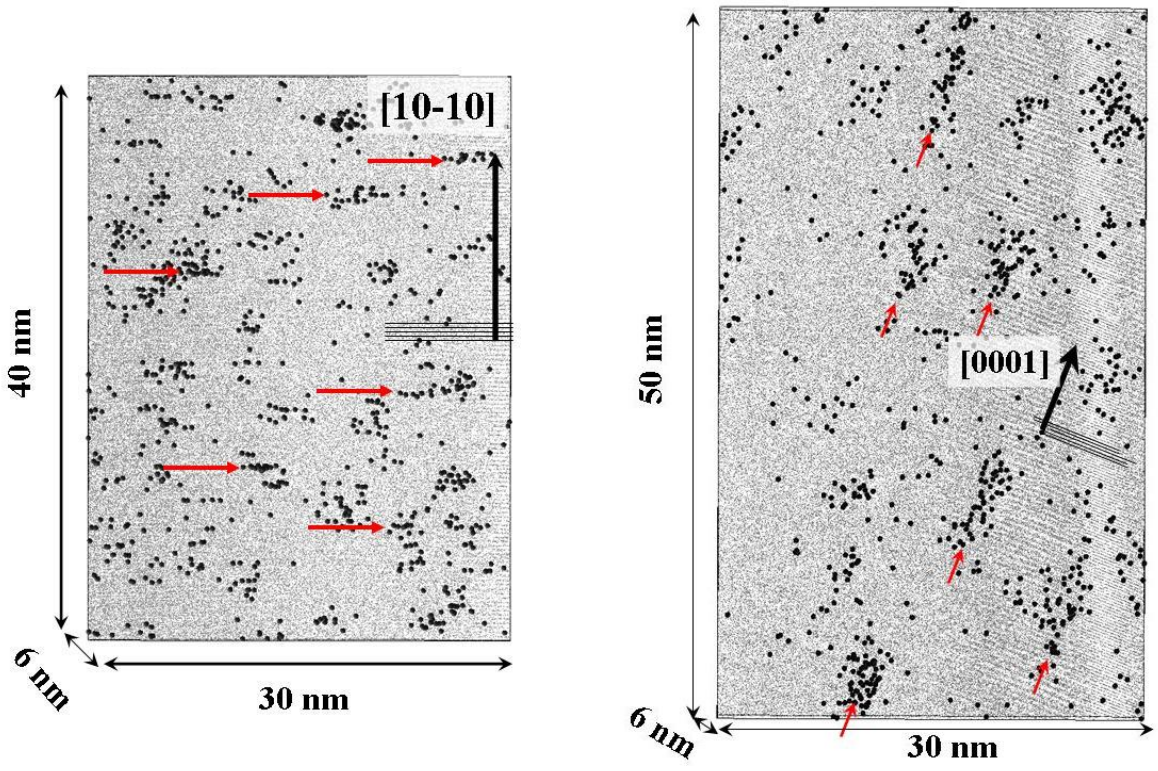

a) b)

Figure 3.3.2: APT atomic maps of a Mg-Nd sample aged at 150°C for a) 54 hours and b) 101 hours. The special orientations of analyzed volumes are chosen in order to demonstrate precipitate morphology and orientation.

Due to a very small precipitate size and the strong local magnification effect the most of atomic clusters observed after 54 h of aging are rather shapeless. However, an accurate inspection of the analyzed volume reveals that some of the precipitates form as very thin Nd-rich atomic sequences on the $(1\bar{1}00)$-atomic planes (Figure 3.3.2a). In the sample aged for 101 h (Figure 3.3.2b), the (0002) planes were revealed. The precipitates, as shown by Figure 3.3.2b, are elongated along [0001]. We suppose that the precipitates observed after 54 h and 101 h of aging are of the same nature. Superposing the results, we conclude that the precipitates are almost two-dimensional plates with the $\{1\bar{1}00\}$ habit plane elongated in the [0001] direction.

Sample aged for 216 **hours at** 150°**C.** The development of the precipitate microstructure proceeds. The precipitates stay very thin in one dimension. Their growth is performed by the subsequent coarsening in two directions. Figure 3.3.3 clearly demonstrates this time that the habit plane for precipitates is from $\{1\bar{1}00\}$-plane family.

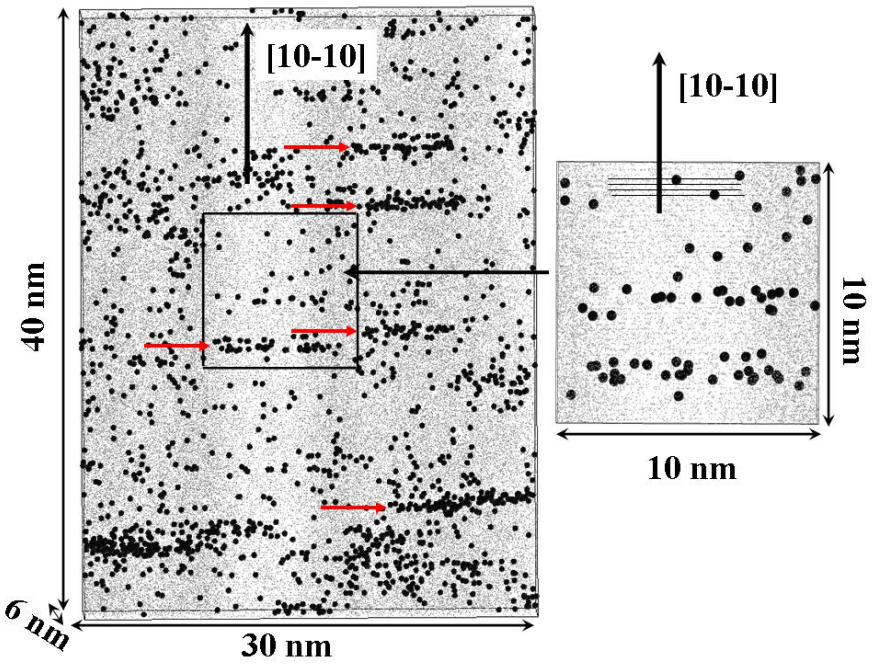

Figure 3.3.3: APT atomic map of a Mg-Nd sample aged at 150°C for 216 hours.

Samples aged for 432 **and** 864 **hours at** 150°**C.** These late stages of precipitation are characterized by further development of precipitate microstructure.

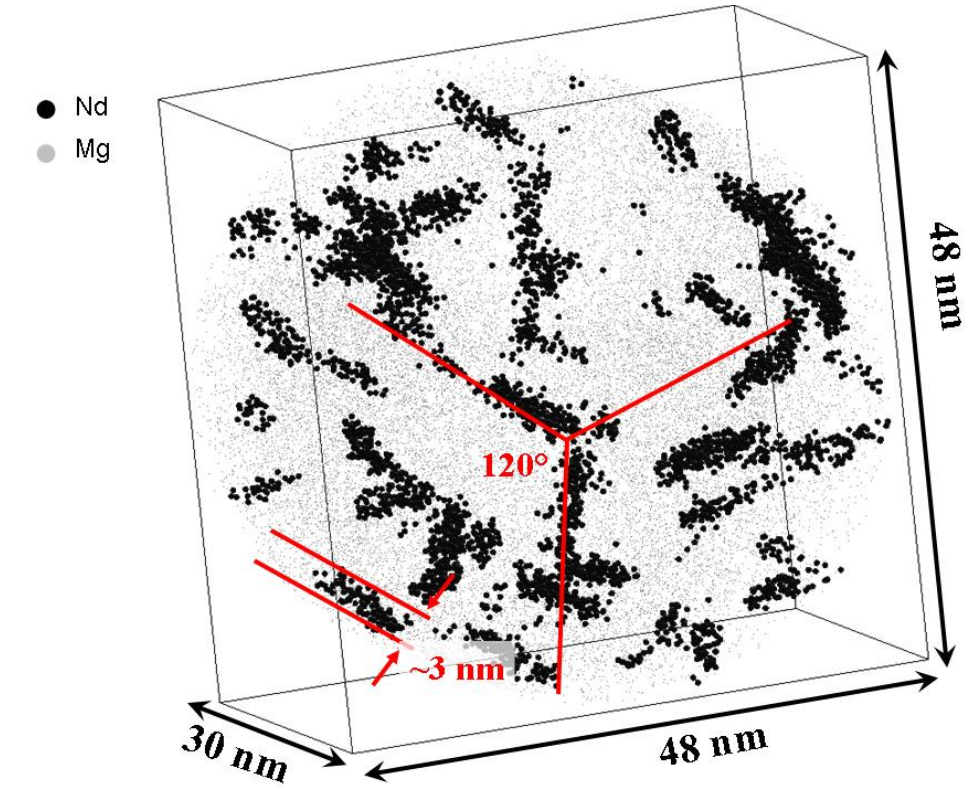

a)

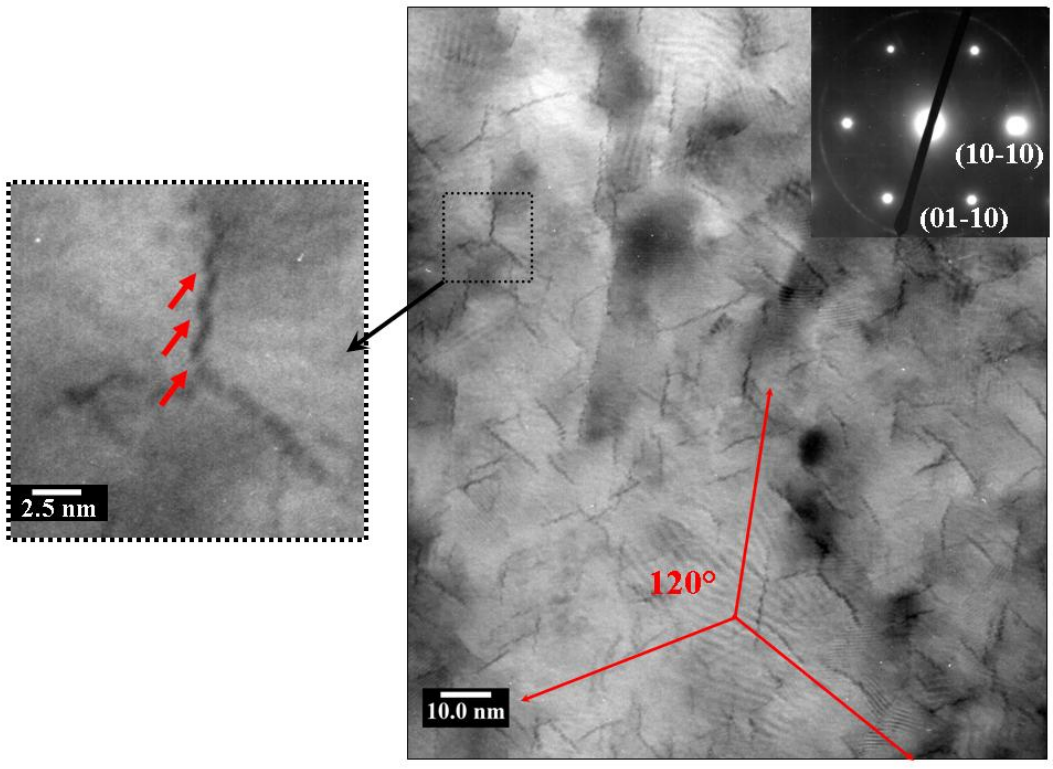

b)

Figure 3.3.4: a) APT atomic map and b) TEM micrograph of a Mg-Nd sample aged at 150°C for 864 hours. The zone axis is close to [0001] direction.

The specific angle relationships, previously reported for the sample aged at 190°C for 24 h can be clearly revealed in the alloy after the annealing at these times (see for example, Figure 3.3.4a). The angles between precipitates at a certain direction of view are approximately equal to 120°. Obviously, this direction of view should correspond to the direction [0001] of the *hcp*-lattice. Observed precipitate thickness ranges in interval to 1–3 nm.

In order to compare the result of APT analysis to TEM observations, TEM micrographs of a sample aged for 864 h at 150°C are provided in Figures 3.3.4b and 3.3.5b. In Figure 3.3.4b) the zone axis is close to [0001]. The precipitates appear as thin sticks on micrograph's plane. The sticks have various lengths on the basal plane which ranges in the interval 4–10 nm. The thickness of sticks is hardly measurable, but obviously does not overcome 1 nm. It is less than that observed in the APT analysis. Three precipitate orientations are clearly visible. It is worth noting that observed precipitates are rough, i.e. consist of some subfragments, as shown in the zoomed inset of Figure 3.3.4b.

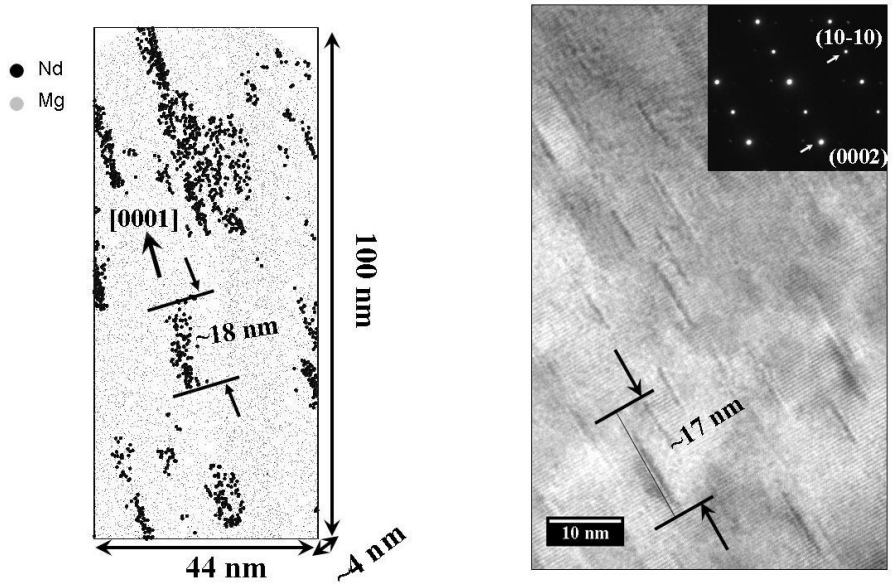

Figure 3.3.5: a)APT atomic map and b) TEM micrograph of a Mg-Nd sample aged at 150°C for 864 hours. The zone axis is perpendicular to [0001] direction.

Figure 3.3.5 provides the comparison of precipitate morphology as investigated by TEM and APT techniques from another direction of view: the zone axis is perpendicular to [0001] direction. The morphology and the precipitate sizes are quantitatively similar as observed by both techniques.

Long time aging for 1324 **hours at** 150°**C.** After this aging, precipitates become comparable in their sizes with those observed in the sample aged for 24 h at 190°C. Most of precipitates are plate-like, with the bigger dimension directed along the [0001] axis of the Mg-matrix. Rare precipitates demonstrate a complex shape as shown in Figure 3.3.6c. As it is seen from the figure, the precipitate may spontaneously change on 60° degrees its direction of growth. Coagulated precipitates were also revealed.

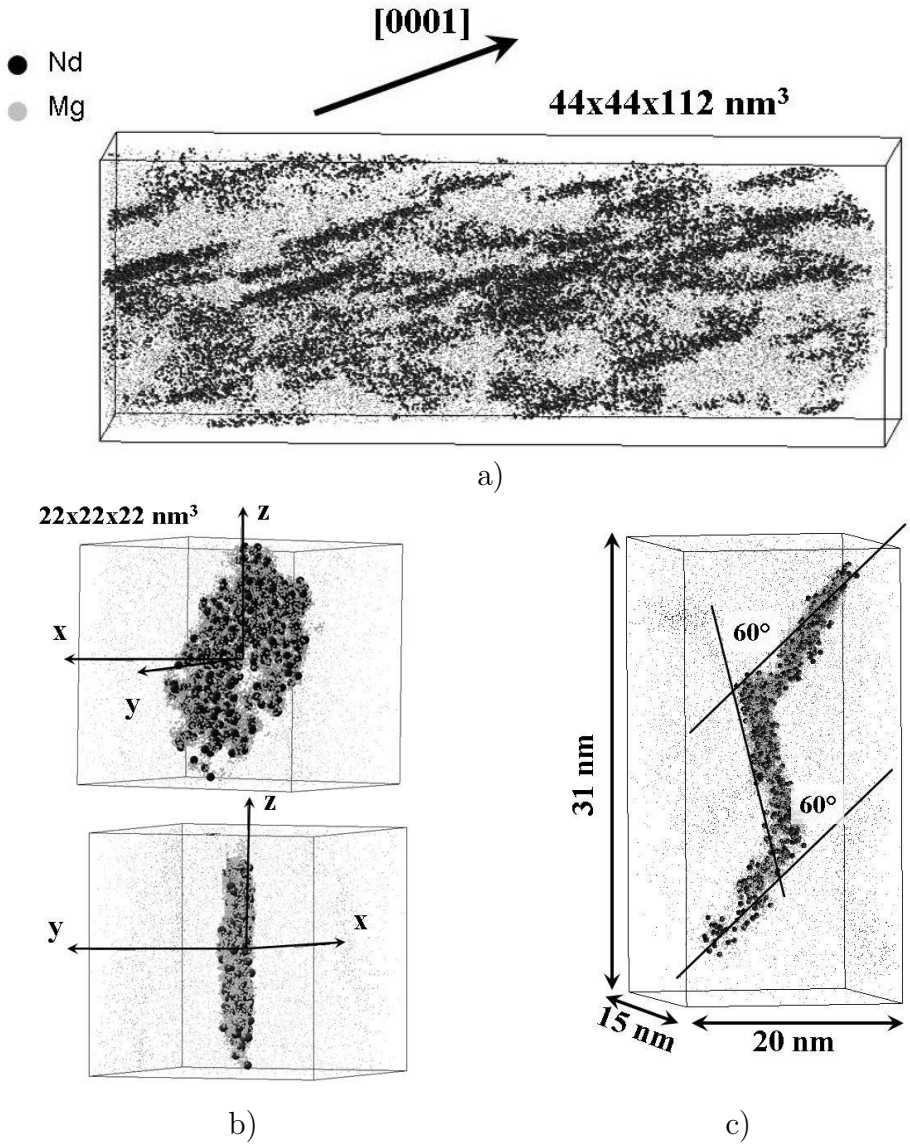

Figure 3.3.6: APT atomic maps of a Mg-Nd sample aged at 150°C for 1324 hours. a) The perspective view of the analyzed volume. b) Typical shape of the formed precipitates. c) A precipitate of the complex shape revealed in the volume.

Overall kinetics. The APT data presented in this section were analyzed using software developed at the University of Rouen. Details of the cluster identification procedure that was applied

to distinguish particles from the matrix are given in Section 2.3.1. Parameters used for cluster identification are presented in Table 3.3.1.

$c_N^{min}d$, %	R^{max}, nm	N^{min}
2	0.1	50

Table 3.3.1: Parameters used for the cluster identification.

Cluster identification algorithm was applied to reconstructed volumes with dimensions $20 \times 20 \times 60$ nm^3 each containing approximately 600 thousands atoms. Then, every identified cluster was checked manually if it consisted of one single precipitate or an agglomerate of precipitates. The number of glued precipitates in every agglomerate is taken into account in the calculation of the precipitate number density, $N_\nu^{prec} = N^{prec}/V$ (being N^{prec} number of precipitates in the volume V).

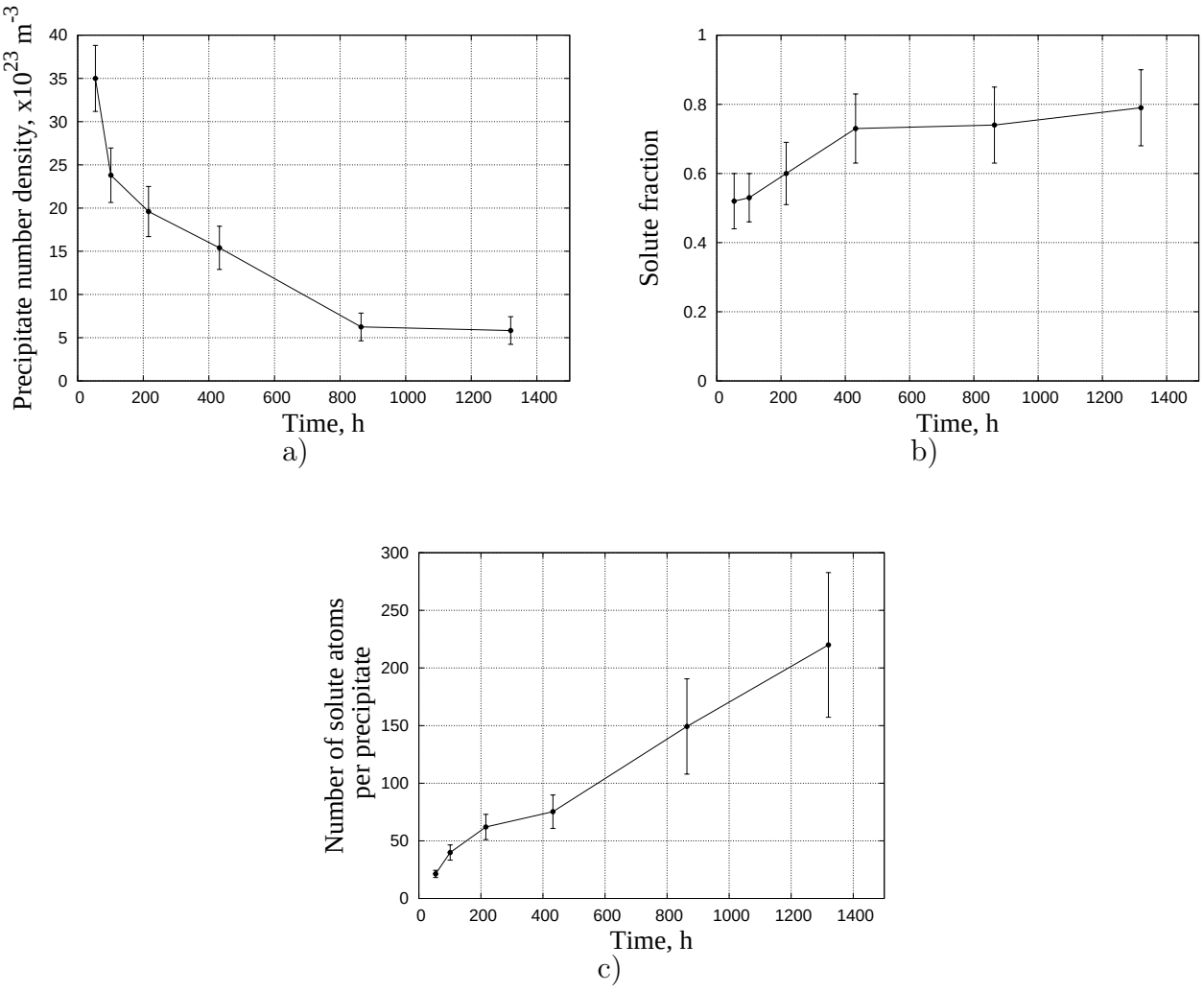

Figure 3.3.7: The temporal evolution of the precipitate a) number density, N_ν^{prec}, b) involved solute fraction, f_s, and c) mean number of solute atoms per precipitate, $\langle N \rangle_s^{prec}$.

The error in precipitate number density, ΔN_{ν}^{prec}, is calculated as $\sqrt{N^{prec}}/V$. Approximately 50% of precipitates, independently on the time of aging, were observed being glued, either due to the CI protocol or due to the real coagulation of precipitates.

Figure 3.3.7 displays the temporal evolution of the precipitate number density, N_{ν}^{prec}, involved solute fraction, f_s, (as defined in Section 3.2.5), and the mean number of solute atoms per precipitate, $\langle N \rangle_s^{prec}$. The mean number of solute atoms per precipitate, $\langle N \rangle_s^{prec}$, is calculated by the equation $\langle N \rangle_s^{prec} = N_s^{prec}/N^{prec}$, where N_s^{prec} and N^{prec} are the number of solute atoms in precipitates and number of precipitates in the investigated volume, respectively. Thus, the error $\Delta\langle N \rangle_s^{prec}$ is given by $\langle N \rangle_s^{prec}\sqrt{\alpha^2 + 1/N^{prec}}$, where α provides the relative error made in the measurement of N_s^{prec}. It is set equal to 0.1.

The precipitate concentration as investigated by the cluster identification is significantly lower ($\sim$ 4at.%) than the expected one, due to the reasons listed and discussed in previous section. The real (unbiased) concentration of the secondary phase measured at late stages of aging (864 h and 1300 h) using the correction method similar to described in Section 3.2.5[5]. The corrected precipitate compositions are provided in Table 3.3.2. They are comparable with those measured in the Mg-Nd sample aged at 190°C for 24 h.

The β''-precipitate nanostructural properties determined by APT analysis are summarized in Table 3.3.2.

Time, h	N_{ν}, $\times 10^{23}\mathrm{m}^{-3}$	f_s, a.u	c_{Nd}^{prec}, %	Width, nm	Length, nm	$\langle N \rangle_s^{prec}$
54	35.0 ± 3.8	0.52 ± 0.07	–	2.4 ± 0.9	3.4 ± 1.6	21 ± 3
101	23.8 ± 3.2	0.53 ± 0.08	–	3.1 ± 1.4	4.3 ± 1.8	40 ± 6
216	19.6 ± 2.9	0.60 ± 0.09	–	3.2 ± 1.1	4.9 ± 1.8	62 ± 11
432	15.4 ± 2.5	0.73 ± 0.10	–	4.4 ± 1.5	6.3 ± 2.5	75 ± 15
864	6.3 ± 1.6	0.74 ± 0.11	13.1 ± 3.3	5.6 ± 2.9	9.9 ± 3.6	149 ± 41
1324	5.8 ± 1.6	0.79 ± 0.11	14.7 ± 2.2	7.9 ± 1.8	16.2 ± 4.9	220 ± 62

Table 3.3.2: Temporal evolution of the nanostructural properties of precipitates determined by APT for Mg-Nd alloy aged at 150°C. The precipitate number density, N_{ν}^{prec}, involved solute fraction f_s, measured precipitate concentration c_{Nd}^{prec}, width, length and mean number of solute atoms per precipitate are given. The standard errors are provided for all quantities.

Precipitates that intersected the sample volume contributed to the precipitate number density and were included in the estimates of precipitate compositions and atomic fractions, and not in the measurement of sizes. Since the precipitates are found to be plate-shaped, their size should

[5]At early stages precipitates are not large enough to build a concentration profiles across them, thus, the correction method is unappropriable.

be characterized by three dimensions (Figure 3.3.8). Sizes: the thickness, width and length of plate-like precipitates were also measured manually, the definition of these quantities is given in Figure 3.3.8.

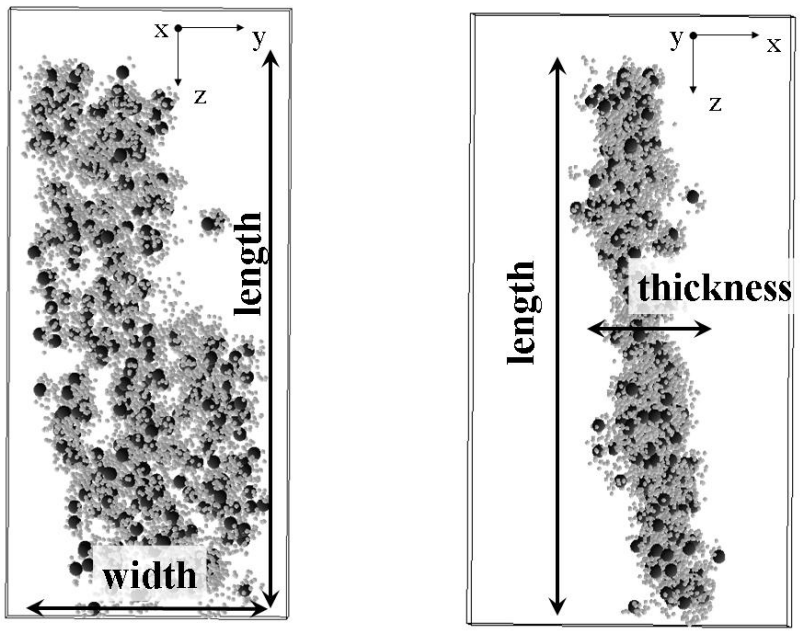

Figure 3.3.8: Schematic definition of parameters called thickness, width and length of plate-like precipitates typically observed in Mg-RE alloys.

The thickness of precipitates was found to be quite small ($\sim$ 2 nm) and not evolve significantly during annealing. The precipitate growth was found to appear mainly by extension of two precip-

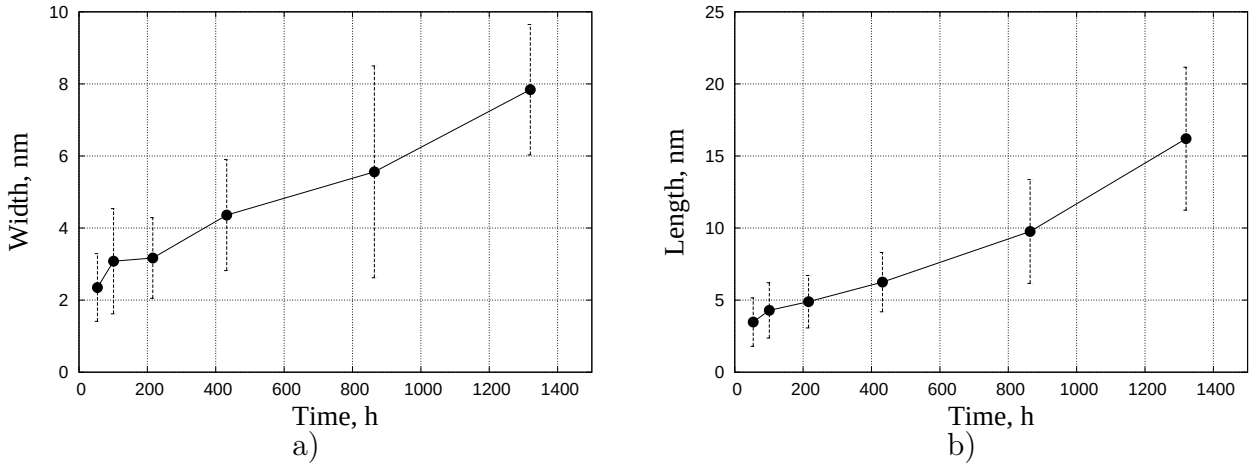

Figure 3.3.9: Evolution of a) width and b) length characteristics of plate-like precipitates formed in binary Mg-Nd alloy during aging at 150°C.

itate dimensions, which were earlier named width and length. The evolution of these parameters

is presented in Figure 3.3.9.

The errors made in the measurements of precipitate sizes were calculated as standard deviations: $\Delta a = \sum_i \sqrt{(a_i - \langle a \rangle)^2/N}$, where $\langle a \rangle$ is the mean value of a size and summation is performed over all N measured precipitates. Due to the fact, that the observed precipitates have a big variation of sizes and the number of analyzed precipitates is limited (from several tens to one hundred), the values of errors are significant. Still it is possible to conclude that both precipitate dimensions demonstrate a monotonous growth during aging. The ratio between width and length deviates in the range $0.5 - 0.7$.

3.3.2 Discussion

During all aging period, the value of N_ν drops from the maximum value of $(35.0 \pm 3.8) \times 10^{23}$ m^3 at 54 h, to $(5.8 \pm 1.6) \times 10^{23}$ m^3 at 1324 h as a result of coarsening. Note that the value of f_s increases from 2.4 ± 0.9 to $7.9 \pm 1.8\%$ over this range of time, thus precipitate growth is ongoing, involving the new solute atoms into precipitation. As a result the number of atoms per precipitate, $\langle N \rangle_s^{prec}$, also increases (Figure 3.3.7).

These precipitates are most probably the ordered *GP zones* which existence earlier was discussed in binary Mg-Nd alloy [Pik73, Kar85, Lor86, His02]. As distinct from results of Pike and Noble [Pik73], who suggested needle-shaped form for the GP zones and {0002}-plane as habit, we show here that they are rather plate-like and lie in $\{10\bar{1}0\}$ plane. Except two-dimensional coarsening, we do not observe any significant changes in precipitate morphology, crystalographic relationships or composition. Thus, we claim that the GP zones are in fact tiny β'' precipitates which exist in the Mg-Nd precipitation sequence as the second precipitating metastable phase.

The observed precipitate shape and orientation should allow to minimize their elastic strain energy [Kha83]. The latter, obviously, plays a major role for precipitate morphology, distribution and orientation relationships. The elastic term in the expression for the free energy of the solid solution should be significant. Due to the latter fact, analysis of the kinetics of the system in terms of the simple nucleation theories seems to be not possible.

The effect of elastic interaction on the formation and dynamic evolution of multidomain microstructures during a hexagonal to orthorhombic transformation[6] was investigated numerically

[6]Formation of coherent precipitates enriched in solute elements leads to differences in lattice parameters of precipitate and matrix phases. GP zones, for example, in cubic matrices are slightly tetragonal. It is expected that coherent precipitates in hexagonal lattice should be slightly orthorhombic.

using phase field model in work of Wen and co-workers [Wen99]. These authors have shown that the nucleation and growth of a new phase produces thin plates of the orthorhombic domains with definite habit planes. However, the approximations used in the works (two-dimensional case, absence of volume change for the transformation) give a family of habit planes different from those observed in our experiments.

Habit plane of orthorhombic precipitates in hexagonal close-packed parent matrix. According to Khachaturyan [Kha83] and as it was already mentioned in Section 1.1.3, the determination of the habit plane orientation of a coherent plate-like precipitate is reduced to the minimization of the function $B(\vec{n})$ defined by

$$B(\vec{n}) = \lambda_{ijkl}\varepsilon^0_{ij}\varepsilon^0_{kl} - n_i\sigma^0_{ij}\Omega_{jl}(\vec{n})\sigma^0_{lm}n_m \tag{3.3.1}$$

with respect to the unit vector $\vec{n} = (n_1, n_2, n_3) = \vec{k}/k$ ($\vec{k}$ being a reciprocal vector). Where ε^0_{ij} is an arbitrary stress-free transformation strain

$$\sigma^0_{ij} = \lambda_{ijkl}\varepsilon^0_{kl}$$

$\Omega_{ij}(\vec{n})$ is the inverse tensor to

$$\Omega^{-1}_{ij}(\vec{n}) = \lambda_{ijkl}n_k n_l. \tag{3.3.2}$$

λ_{ijkl} is the elastic modulus tensor.

As it arises from Eq. 3.3.1 the function $B(\vec{n})$ can be split into two terms as follows

$$B(\vec{n}) = B_0 - B_1(\vec{n}), \tag{3.3.3}$$

where $B_0 = \lambda_{ijkl}\varepsilon^0_{ij}\varepsilon^0_{kl}$ and $B_1(\vec{n}) = n_i\sigma^0_{ij}\Omega_{jl}(\vec{n})\sigma^0_{lm}n_m$. Since B_0 is a constant, $B(\vec{n})$ reaches its minimum when the function $B_1(\vec{n})$ has the maximum value. The values $\vec{n}^{(i)}$ at which $B(\vec{n})$ has its minimum (or equivalently $B_1(\vec{n})$ — its maximum) define the normals to the habit planes of precipitates of a secondary phase.

The problem of apparent habit planes in the case of a coherent tetragonal phase inclusions in a cubic parent phase matrix has been solved by Wen et al. [Wen81]. Details on their solutions

may be found elsewhere [Kha83].

In our case, we consider an orthorhombic phase inclusion in a hexagonal parent phase matrix. The nonzero components of the elastic modulus of a hexagonal crystal λ_{ijkl} are

$$\begin{aligned} \lambda_{1111} = \lambda_{2222} &= c_{11} \\ \lambda_{1122} &= c_{12} \\ \lambda_{1133} = \lambda_{2233} &= c_{13} \\ \lambda_{1313} = \lambda_{2323} &= c_{44} \\ \lambda_{3333} &= c_{33} \\ \lambda_{1212} &= (c_{11} - c_{12})/2 \end{aligned} \quad , \tag{3.3.4}$$

where c_{ij} are the elastic moduli in Voigt notation (see e.g. [Lan86]). Using these constants and the symmetry relations for the tensor λ_{ijkl}, the tensor $\Omega^{-1}_{ij}(\vec{n})$ (Eq. 3.3.2) can be written as:

$$\hat{\Omega}^{-1} = \begin{pmatrix} c_{11}n_1^2 + \frac{c_{11}-c_{12}}{2}n_2^2 + c_{44}n_3^2 & \frac{c_{11}+c_{12}}{2}n_1n_2 & (c_{13}+c_{44})n_1n_3 \\ \frac{c_{11}+c_{12}}{2}n_2n_1 & \frac{c_{11}-c_{12}}{2}n_1^2 + c_{11}n_2^2 + c_{44}n_3^2 & \frac{c_{13}+c_{44}}{2}n_2n_3 \\ (c_{13}+c_{44})n_3n_1 & \frac{c_{13}+c_{44}}{2}n_3n_2 & c_{44}n_1^2 + c_{44}n_2^2 + c_{33}n_3^2 \end{pmatrix}. \tag{3.3.5}$$

Transformation strain tensor can be expressed by a symmetrical matrix. It is well known that any symmetrical matrix can be reduced to a diagonal form by a proper choice of the coordinate system. Thus, without loosing a generality, the stress-free transformation strain tensor, stress-free transformation strain tensor, ε^0_{ij}, for a hexagonal to orthorhombic transformation is given by diagonal matrix:

$$\hat{\varepsilon}^0 = \begin{pmatrix} \varepsilon_a & 0 & 0 \\ 0 & \varepsilon_b & 0 \\ 0 & 0 & \varepsilon_c \end{pmatrix}, \tag{3.3.6}$$

where the relations between components of the tensor and the lattice parameters of hexagonal matrix and orthorhombic inclusion are following: $\varepsilon_a = \frac{a_{ort}}{a_{hcp}} - 1$, $\varepsilon_b = \frac{b_{ort}}{b_{hcp}} - 1$ and $\varepsilon_c = \frac{c_{ort}}{c_{hcp}} - 1$.

Due to the higher complexity of a hexagonal lattice in comparison to a cubic one, the problem of finding the habit planes in the case of plate-like coherent orthorhombic precipitates in a hexagonal parent phase matrix cannot be solved analytically in three dimensions. That is why, we will preform the quantitative analysis in two-dimensional system.

If we assume that the lattice misfit between the hexagonal and orthorhombic phases along the c-direction can be neglected, the transformation strain (Eq. 3.3.6) becomes

$$\hat{\varepsilon}^0 = \begin{pmatrix} \varepsilon_a & 0 \\ 0 & \varepsilon_b \end{pmatrix}. \tag{3.3.7}$$

With the particular form of the transformation strain (Eq. 3.3.7), the domain structure during the hexagonal $\rightarrow$ orthorhombic transformation can be quantitatively modeled in two dimensions, and then qualitatively compared to the three-dimensional case.

The two-dimensional Green function, $\hat{\Omega}$, (where $\hat{\Omega}\hat{\Omega}^{-1} = I$, and I being the unit matrix) becomes

$$\hat{\Omega} = \begin{pmatrix} \frac{\alpha n_1^2 - n_2^2 - 1}{(\alpha-1)c_{11}} & \frac{(\alpha+1)n_1 n_2}{(\alpha-1)c_{11}} \\ \frac{(\alpha+1)n_1 n_2}{(\alpha-1)c_{11}} & \frac{n_1^2 - \alpha n_2^2 + 1}{(\alpha-1)c_{11}} \end{pmatrix}, \tag{3.3.8}$$

where $\alpha = c_{12}/c_{11}$. Substitution of tensors Ω_{ij} and ε^0_{ij} in $B_1(\vec{n})$ yields:

$$B_1(\vec{n}) = c_{11}^2 \left\{ (\varepsilon_a + \alpha\varepsilon_b)^2 n_1^4 + 2[(\varepsilon_a - \varepsilon_b)^2 + \varepsilon_a\varepsilon_b(1+\alpha^2)] n_1^2 n_2^2 + (\alpha\varepsilon_a + \varepsilon_b)^2 n_2^4 \right\}. \tag{3.3.9}$$

The extremums of the function $B_1(\vec{n})$ can be found by the solution of the following set of equations:

$$\begin{cases} \frac{\partial B_1(\vec{n})}{\partial n_1} = 0 \\ \frac{\partial B_1(\vec{n})}{\partial n_2} = 0 \end{cases}$$

with the additional condition $n_1^2 + n_2^2 = 1$. These solutions are following:

$$\vec{n}^{(1)} = (0,\ 1) \tag{3.3.10}$$

$$\vec{n}^{(2)} = \left(\sqrt{\tfrac{\varepsilon_a}{\varepsilon_a - \varepsilon_b}}, \sqrt{\tfrac{-\varepsilon_b}{\varepsilon_a - \varepsilon_b}} \right) \tag{3.3.11}$$

$$\vec{n}^{(3)} = \left(-\sqrt{\tfrac{\varepsilon_a}{\varepsilon_a - \varepsilon_b}}, \sqrt{\tfrac{-\varepsilon_b}{\varepsilon_a - \varepsilon_b}} \right), \tag{3.3.12}$$

we add also the fourth point

$$\vec{n}^{(4)} = (1,\ 0), \tag{3.3.13}$$

as the function $B_1(\vec{n})$ may have a maximum value at the limiting point.

Values of the function $B_1(\vec{n})$ at its exteremum points, $\vec{n}^{(i)}$, are following:

$$B_1(\vec{n}^{(1)}) = (\varepsilon_b^2 + 2\varepsilon_a\varepsilon_b\alpha + \varepsilon_a^2\alpha^2)c_{11}^2 \tag{3.3.14}$$

$$B_1(\vec{n}^{(2)}) = (\varepsilon_a^2 + 2\varepsilon_a\varepsilon_b\alpha + \varepsilon_b^2)c_{11}^2 \tag{3.3.15}$$

$$B_1(\vec{n}^{(3)}) = (\varepsilon_a^2 + 2\varepsilon_a\varepsilon_b\alpha + \varepsilon_b^2)c_{11}^2 \tag{3.3.16}$$

$$B_1(\vec{n}^{(4)}) = (\varepsilon_a^2 + 2\varepsilon_a\varepsilon_b\alpha + \varepsilon_b^2\alpha^2)c_{11}^2. \tag{3.3.17}$$

It is obvious, that the position of a maximum of the function $B_1(\vec{n})$ depends on the ratio α as well as on the relation between components of the strain tensor ε_a and ε_b. Coordinates of the normals to the habit planes and conditions at which they appear are listed in Table 3.3.3.

Condition	Normal vector(s), $\vec{n}^{(i)}$
$\alpha > 1$, $\lvert\varepsilon_a\rvert > \lvert\varepsilon_b\rvert$	$(0, 1)$
$\alpha > 1$, $\lvert\varepsilon_a\rvert < \lvert\varepsilon_b\rvert$	$(1, 0)$
$\alpha < 1$	$\left(\sqrt{\frac{\varepsilon_a}{\varepsilon_a-\varepsilon_b}}, \sqrt{\frac{-\varepsilon_b}{\varepsilon_a-\varepsilon_b}}\right)$ $\left(-\sqrt{\frac{\varepsilon_a}{\varepsilon_a-\varepsilon_b}}, \sqrt{\frac{-\varepsilon_b}{\varepsilon_a-\varepsilon_b}}\right)$

Table 3.3.3: Habit plane normals and conditions at which they occur. The case when $\varepsilon_a = -\varepsilon_b$ (which corresponds to the third row of the table) has been considered by Wen et al. [Wen99] in their two-dimensional phase-field model.

It is worth mentioning that habit planes of precipitates with normals $\vec{n}^{(1)} = (0,\ 1)$ and $\vec{n}^{(4)} = (1,\ 0)$ can be realized also when $\alpha < 1$. This requires the components of stress-free strain tensor to have special values: $\vec{n}^{(1)}$ is realized when $\varepsilon_a = 0$ and $\vec{n}^{(4)}$ — when $\varepsilon_b = 0$.

Up to now we considered only habit planes for precipitates generated by the transformation strain given by Eq. 3.3.7. However, taking into account the symmetry of the hexagonal lattice, we have to consider two other orientation variants. These two variants can be obtained by rotations

at a 120° and a 240°. The stress free strain tensors for all three variants are given by

$$\hat{\varepsilon}(1)^0 = \begin{pmatrix} \varepsilon_a & 0 \\ 0 & \varepsilon_b \end{pmatrix} \tag{3.3.18}$$

$$\hat{\varepsilon}(2)^0 = \begin{pmatrix} -\varepsilon_a/2 & -\sqrt{3}\varepsilon_b/2 \\ \sqrt{3}\varepsilon_a/2 & -\varepsilon_b/2 \end{pmatrix}$$

$$\hat{\varepsilon}(3)^0 = \begin{pmatrix} -\varepsilon_a/2 & \sqrt{3}\varepsilon_b/2 \\ -\sqrt{3}\varepsilon_a/2 & -\varepsilon_b/2 \end{pmatrix}.$$

The tensors leads to the formation of the plate-like precipitates with the same degree of orthorhombicity, but the plates are turned with respect to each other on the angle equal to 120°.

A coherent new phase particle in a constrained state has a crystal lattice different from that of the particle in the stress-free state. The difference between the lattices corresponding to constrained and stress-free states is due to elastic strain caused by crystal lattice mismatch along interphase boundaries.

Any coherent plate-like inclusion undergoes homogeneous elastic strain to restore the habit plane to the state it had before the transformation occurred, to provide the exact coincidence of the habit planes of the new phase particle and the undistorted matrix. The total strain within the inclusion is by definition an invariant plane strain, the habit plane strain being the invariant plane. According to [Kha83], any crystal lattice translation $\vec{r}$ of the parent phase is transformed into $\vec{r}'$ after the phase transition

$$\vec{r}' = \vec{r} + \vec{S}(\vec{n}^{(i)})(\vec{n}^{(i)}\vec{r}), \tag{3.3.19}$$

where $\vec{S}(\vec{n}^{(i)})$ is the shear vector given by $\vec{S}(\vec{n}^{(i)}) = \hat{\Omega}(\vec{n}^{(i)})\hat{\sigma}^0\vec{n}^{(i)}$. Equation 3.3.19 determines the orientation relations between the crystal lattices of the inclusion and parent phase.

As it was mentioned above, an analytical classification of precipitate habit planes in the three-dimensional case of a hexagonal to orthorhombic transformations cannot be done, due to the complexity of the Green function $\hat{\Omega}$. These calculations may be performed in every particular case, when numerical values of elastic constants, λ_{ijkl}, and transformation strain of new phase, ε^0_{ij}, are known. Here we confine ourself to the calculation of lattice parameters of the orthorhombic precipitates.

For the habit plane orientations observed in different Mg-RE alloys [7] the lattice parameters of the secondary phase in three-dimensional case have been calculated and presented in Table 3.3.4.

Normal vector(s), $\vec{n}^{(i)}$	Lattice parameters
$(0,1,0)$	$a_p = a_0$ $b_p = a_0\left(1+\frac{3}{4}(\varepsilon_a\frac{c_{12}}{c_{11}}+\varepsilon_b+\varepsilon_c\frac{c_{13}}{c_{11}})\right)$ $c_p = c_0$ $\gamma = 180^\circ - 57.30^\circ \arccos\left\{\frac{1}{2}\left[1-\frac{3}{4}(\varepsilon_a\frac{c_{12}}{c_{11}}+\varepsilon_b+\varepsilon_c\frac{c_{13}}{c_{11}})\right]\right\}$
$(1,0,0)$	$a_p = a_0\left(1+(\varepsilon_a+\varepsilon_b\frac{c_{12}}{c_{11}}+\varepsilon_c\frac{c_{13}}{c_{11}})\right)$ $b_p = a_0\left(1+\frac{1}{4}(\varepsilon_a+\varepsilon_b\frac{c_{12}}{c_{11}}+\varepsilon_c\frac{c_{13}}{c_{11}})\right)$ $c_p = c_0$ $\gamma = 180^\circ - 57.30^\circ \arccos\left\{\frac{1}{2}\left[1+\frac{3}{4}(\varepsilon_a+\varepsilon_b\frac{c_{12}}{c_{11}}+\varepsilon_c\frac{c_{13}}{c_{11}})\right]\right\}$
$(0,0,1)$	$a_p = a_0$ $b_p = a_0$ $c_p = c_0\left(1+(\varepsilon_a\frac{c_{13}}{c_{33}}+\varepsilon_b\frac{c_{13}}{c_{33}}+\varepsilon_c)\right)$ $\gamma = 120^\circ$

Table 3.3.4: Lattice parameters of an orthorhombic phase (a_p, b_p, c_p) as functions of lattice parameter of the parent phase (a_0, c_0), elastic constants and components of transformation strain in case of three-dimensional hexagonal to orthorhombic transformation. The most common cases of habit planes are considered. In these formulas we supposed that components ε_a, ε_b, ε_c are small, and thus only linear terms can be kept. γ is the angle between base vectors $\vec{a}_1^p$ and $\vec{a}_2^p$ of the orthorhombic phase.

In order to clarify the obtained results, the visualizations are given in Figure 3.3.10. As an example in Figures 3.3.10a and b, the correspondence between parent phase and precipitate one is shown. It is clearly seen, that the orthorhombic phase should have a limited thickness in order to keep the correspondence with the matrix. The latter is the reason for the formation of thin precipitates during a hexagonal to orthorhombic transformation. In Figures 3.3.10 c and d, the different types of orthorhombic precipitates (mentioned in Table 3.3.3) are shown embedded into the hexagonal matrix.

Atomic structure of precipitates. The TEM investigation of Mg-Nd sample revealed the complex thin-platelet morphology of the precipitate as shown in Figure 3.3.11a. It was observed by TEM that thin plate-like precipitates laying in $\{1\bar{1}00\}$ planes, consist in fact of very tiny fragments. These fragments, observed at high magnifications, form the 15°-angle with the precipitate growth

[7] The habit planes of precipitates $\{10\bar{1}0\}$ ($\vec{n}(0,1,0)$), $\{11\bar{2}0\}$ ($\vec{n}(1,0,0)$), $\{0001\}$ ($\vec{n}(0,0,1)$ were observed in such alloys as Mg-Nd [His02], Mg-Y-Nd [Ant06] and Mg-RE-Zn-Zr [Pin03], respectively.)

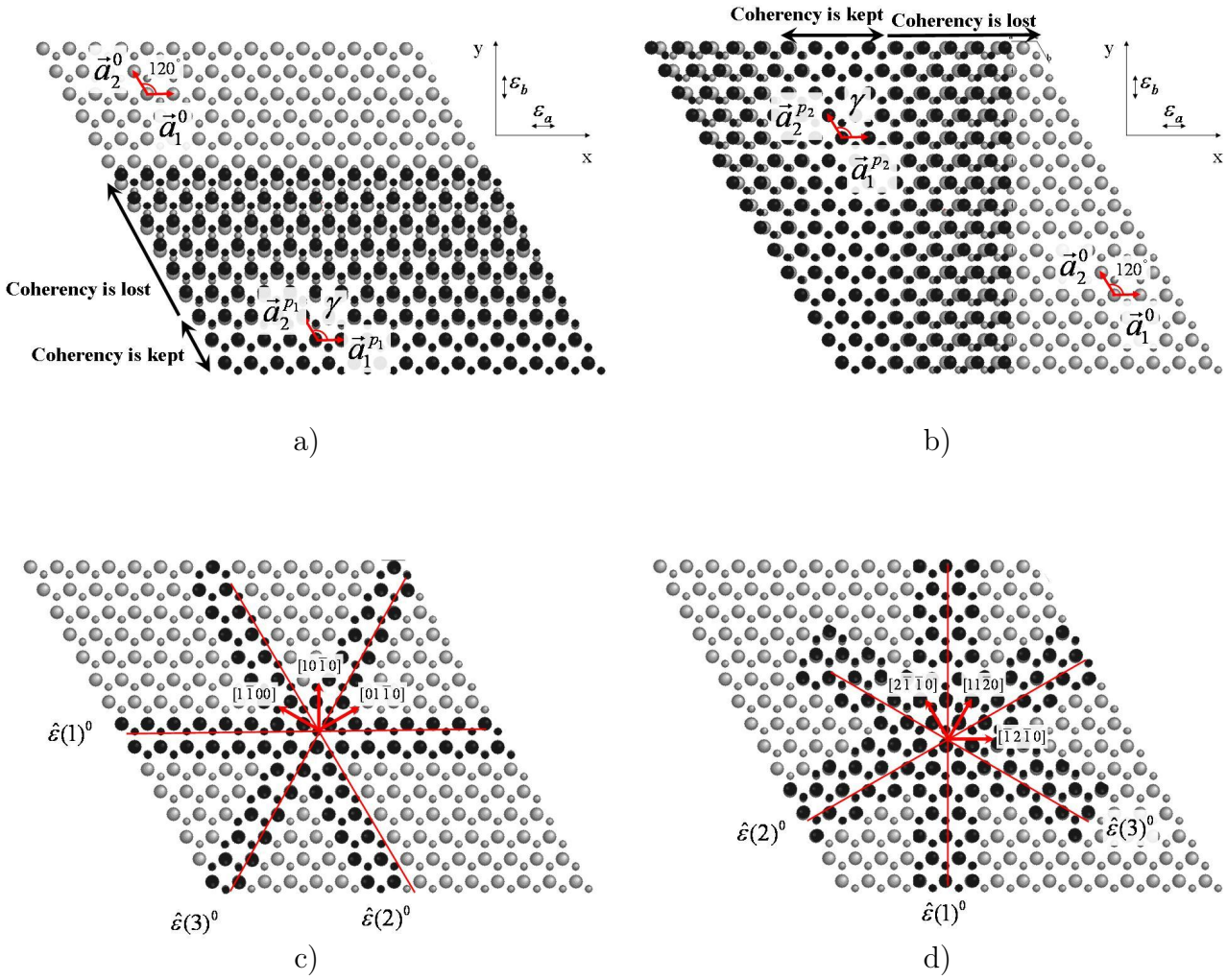

Figure 3.3.10: Visual examples of the formation of plate-like orthorhombic precipitates with a) $\{10\bar{1}0\}$ and b) $\{11\bar{2}0\}$ habit planes. Three possible orientations of precipitates c) for the case a) and d) for the case b). The parameters used in the calculations are following: a) $\varepsilon_a = 0.011$, $\varepsilon_b = 0.010$, $\varepsilon_c = 0$ and b) $\varepsilon_a = 0.010$, $\varepsilon_b = 0.011$, $\varepsilon_c = 0$. Matrix lattice parameters $a_0 = 0.321$ nm, $c_0 = 0.521$ nm.

direction.

A scheme of atomic structure of precipitates consistent with our TEM observations was proposed by Hisa et al. [His02]. Authors analyzed the TEM diffraction patterns (DP) obtained for the aged Mg-Ce alloy. Then, for different model atomic structures, a simulation of diffraction patterns was carried out. A good agreement of the simulated DP with the real ones was obtained for the structure presented in the Figure 3.3.11b. The proposed atomic model structure suggested to appear in the early stage of aging of all Mg alloys containing rare-earth elements from the Ce subgroup (which includes neodymium).

According to Hisa and co-workers [His02], the precipitate has its own ordered structure.

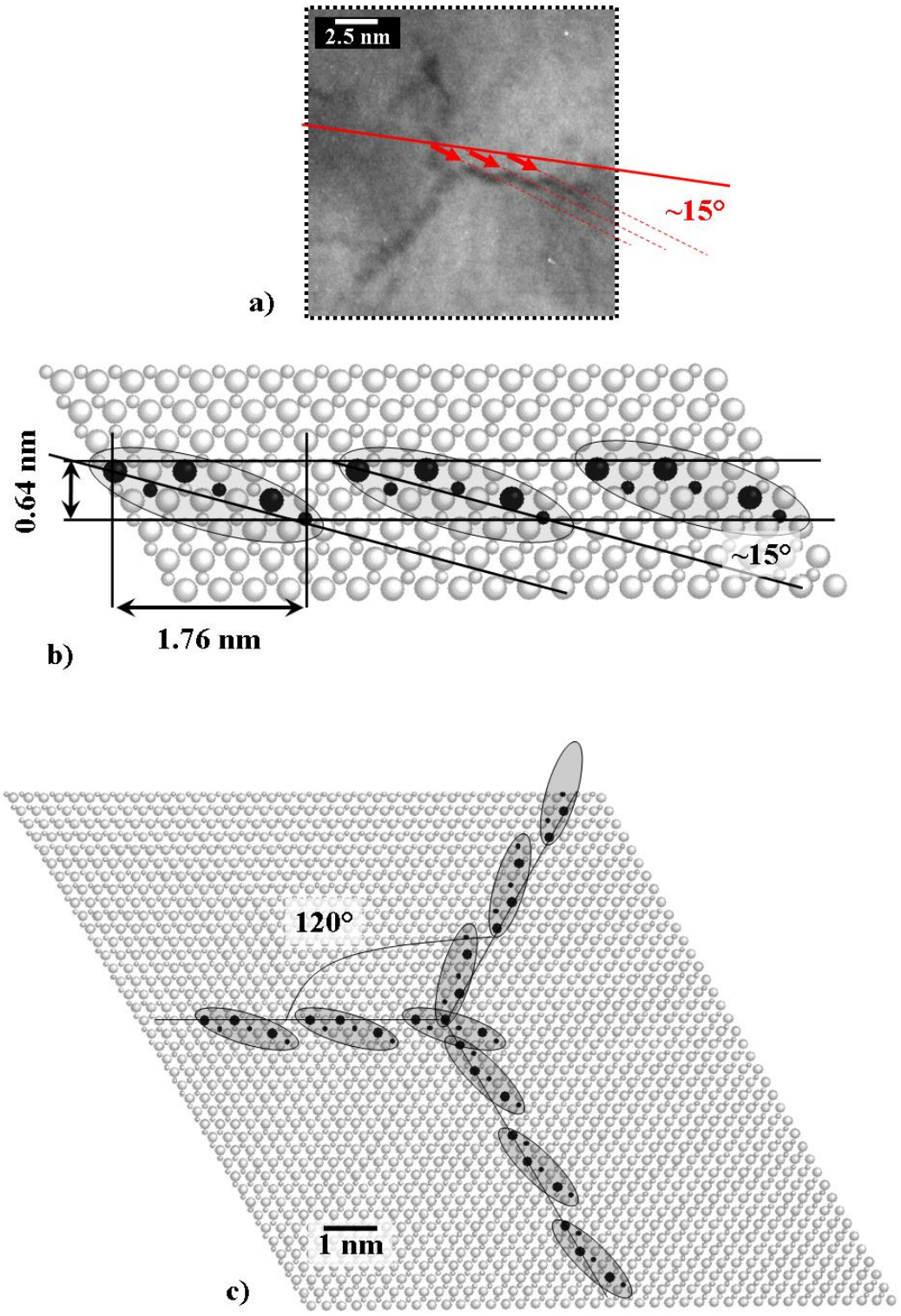

Figure 3.3.11: a) TEM micrograph demonstrating the fine structure of a precipitate in the Mg-Nd alloy aged for 864 h at 150°C. b) The APB-like $D0_{19}$-ordered atomic structure of the precipitate from (a) as proposed by [His02]. c) The schematic presentation of 3 possible variants of complex precipitates.

In this ordered structure, Nd columns are aligned in such a way that they occupy every second

atomic column in the matrix with some periodic steps. These matrix steps are similar to anti-phase boundaries (APBs) in ordered alloys. It is impossible, however, to define the phase shift in atomic configuration introduced by the atomic steps because of the two-dimensional nature of the precipitate. These atomic steps are, therefore, called APB-like steps.

The ordering periodicity of the Nd columns in the structure of the precipitate along $\langle 11\bar{2}0\rangle$ resembles the atomic configuration of the $D0_{19}$ superlattice (see Appendix D). However, because of its two-dimensional morphology, the precipitate cannot form a complete $D0_{19}$; no periodicity can be defined in its thickness direction. This ordered structure containing periodically arranged APB-like steps was named a stepped quasi-$D0_{19}$ structure.

The precipitate has three crystallographically equivalent variants on $\{1\bar{1}00\}$ matrix prismatic planes. These variants are shown in Figure 3.3.11b. The latter is the visualization of precipitate arrangement, which form the 120° angle relationships demonstrated previously on TEM micrograph and APT atomic maps. Typically this type of microstructure was reported in many TEM studies of early stages of phase decomposition in Mg-RE alloys [Wei96, Ant03, Ant06] and, in particular, in Mg-Nd alloy [Wil03].

The suggested above complicated precipitate structure cannot be confirmed by the atom probe investigations due to the strong ion evaporation and reconstruction artifacts. The proposed model, however, may explain the reported above comparably low concentration of Nd (15-18at.%) even in the well developed precipitates. As the structure of precipitate is not the conventional DO_{19} superlattice, but two-dimensional quasi-DO_{19} structure containing APB boundaries, the loss of some solute atoms in the precipitate plane occurs. The latter lowers the concentration from the stoichiometric value equal to 25 at.% to the measured (15-21 at.%). For example, the concentration of Nd in the two Nd-containing planes in the structure from the Figure 3.3.11c is equal to 17.8 at.% and agrees good with the measured values.

3.3.3 Conclusion

A comparison was obtained of the nanostructural and compositional evolution of Mg-Nd during phase separation at 150°C for aging times ranging from 54 h to 1324 h, employing atom probe tomography technique. This alloy was designed to study precipitate formation, their morphology and orientation relationships, leading to the following results:

- The Atom probe technique revealed that the precipitation in the investigated alloy starts by the formation of one-plane precipitates, which are (ordered) GP-zones.
- The precipitates are plates laying on the $\{10\bar{1}0\}$ planes and are elongated along the [0001] direction.
- The composition of precipitating phase was found to range in the interval from 15 to 20 at.% of Nd. It correlates with the composition of APB-like structure of precipitates proposed by Hisa et al. [His02]. This complex structure of precipitates has been revealed by TEM investigations.
- Growth of precipitates is observed during the studied times of aging. The growth mostly proceeds in two directions. The thickening of precipitates is negligible or absent. At late stages, when precipitates become relatively large, some spontaneous change of precipitate growth direction was revealed.

3.4 Precipitation kinetics in ternary Mg-Y-Nd alloy aged at 150°C.

3.4.1 Results

Temporal evolution of the precipitate morphology of the model Mg-2.6Y-2.7Nd (wt.%) alloy is displayed in a series of $10 \times 10 \times 45$ nm^3 APT reconstructions (Figure 3.4.1), each containing approximately 120 thousands atoms. A visual analysis of the distribution of Nd and Y atoms did not produce any evidence for the formation of clusters. However, according to works of Antion et al. [Ant03, Ant06] we should expect in our model ternary alloy the formation of tiny nano-scale precipitates at this temperature and times of aging. In order to examine the reconstructed volumes and explore the existence of an evolution in atomic distributions, the method of radial pair-correlation functions (Section 2.3.3) was applied. The results are presented in Figure 3.4.2.

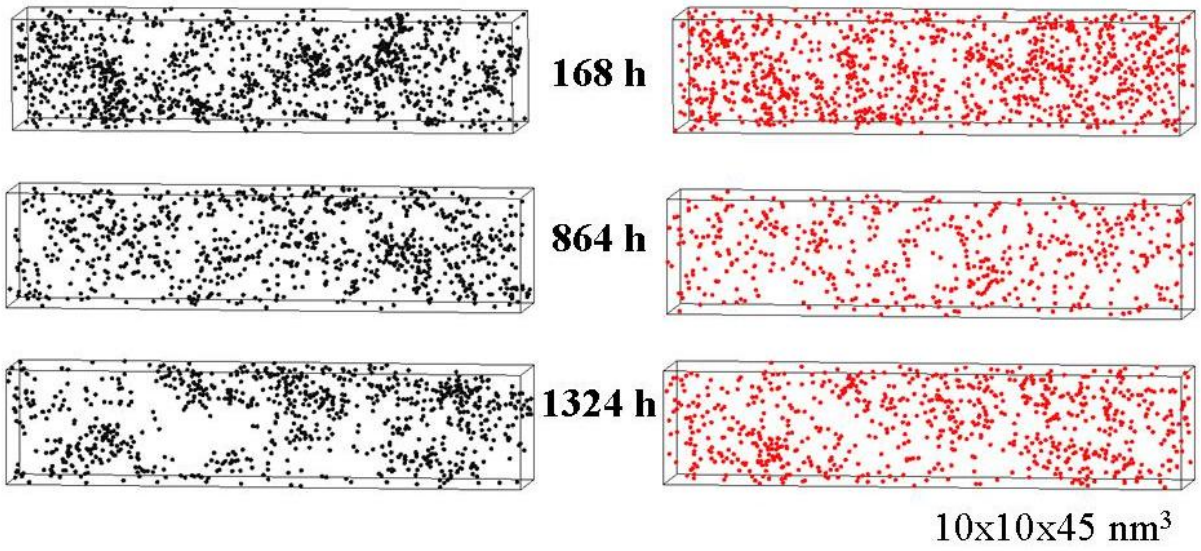

Figure 3.4.1: APT elemental maps of Nd (left) and Y (right) in samples aged at 150°C for various times indicated in the figure.

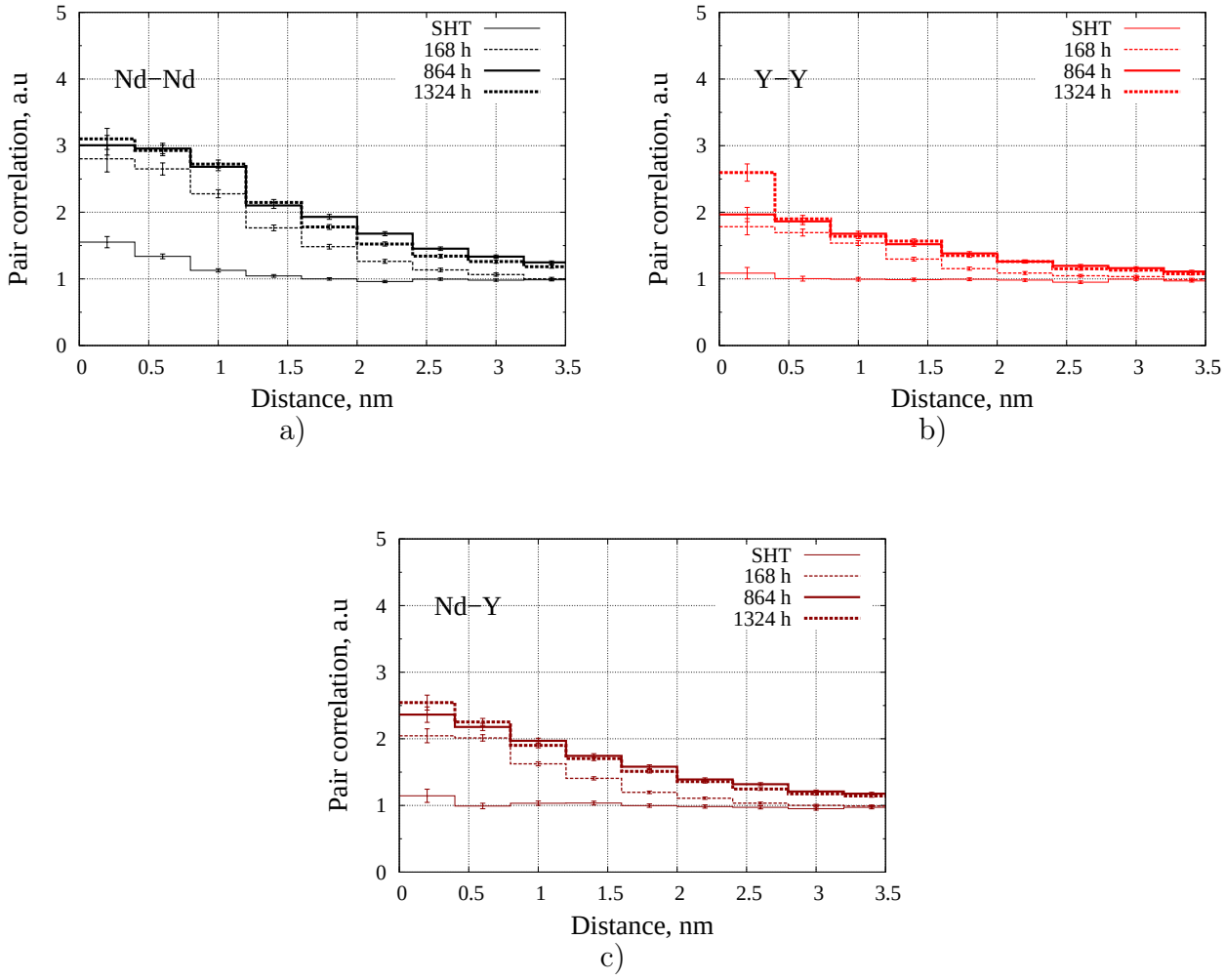

Figure 3.4.2: a) Nd-Nd, b) Y-Y c) Nd-Y pair correlation functions for Mg-Y-Nd samples aged at different temperatures.

The pair correlation function showed that both the Nd and Y exhibit positive autocorrelation, which develops with time of aging. The Nd-Nd autocorrelation is the most pronounced. The existence of Nd-Y cross-correlation should be also noted.

The increase and extension of positive correlation between solute atoms during aging is an indication of the evolution of precipitation. However, positive correlation extends up to a typical radius equal to $\sim$ 3 nm, claiming the existence of nanometer-scale solute-enriched clusters. In order visualize the expected solute inhomogeneities, the standard cluster identification algorithm has been applied (Section 2.3.1) to the reconstructed volumes. The parameters used for cluster identification procedure are provided in Table 3.4.1.

$c_N^{min}d$, %	R^{max}, nm	N^{min}
2	0.1	50

Table 3.4.1: Parameters used for the cluster identification.

Typical treated 3D-atomic maps are displayed in Figure 3.4.3, where solute atoms identified as clustered are presented as spheres with larger radii.

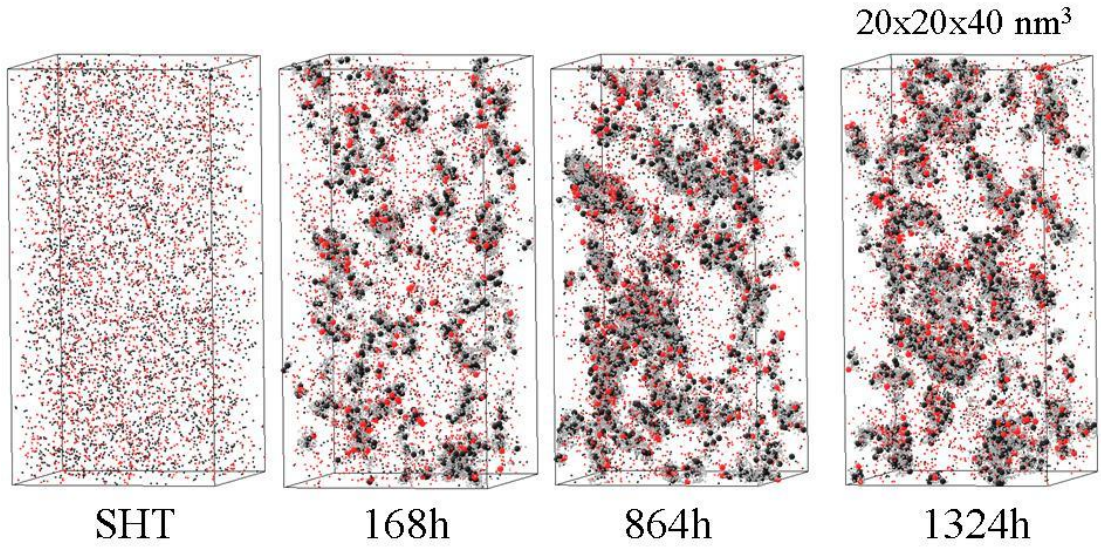

Figure 3.4.3: APT elemental maps of the Mg-Y-Nd alloy aged at 150°C for various times indicated under the corresponding volumes. Nd solute atoms of the matrix are shown as black points; Y solute atoms of the matrix are shown as red points; Mg solvent atoms are omitted for clarity. The nanometer-sized precipitates identified by CI algorithm are highlighted by using spheres of larger radii Mg (gray), Nd (black) and Y (red) atoms.

3.4.2 Discussion

Due to the small size of precipitates which form at the investigated temperature and aging times, the local magnification effect mixes the precipitate atoms with the matrix ones, fuzzing the concentration differences. Then, the applied cluster identification algorithm inevitably includes matrix atoms in clusters because of low concentration gradients between the matrix and clusters in the reconstructed dataset, their small size and nonspherical shape. As a result the measured cluster compositions become very low. In the present case, composition correction procedures are not efficient either. It is however possible to get an indication of the precipitates stoichiometry via the calculation of the ratio between solute atoms involved in the precipitation. The analysis of volumes to which the cluster identification algorithm has been applied, showed that the N_Y^{prec}/N_{Nd}^{prec} ratio is ranges in interval 0.30—0.35. The latter is not in agreement with the stoichiometric formula for the β''-phase $Mg_3(Y_{0.85}Nd_{0.15})$ reported in work of Lorimer [Lor99] for commercial alloys WE43 (4.0wt.% Y, 3.3wt.% RE, 0.5wt.% Zr) and WE54 (5.0wt.% Y, 3.3wt.% RE, 0.5wt.% Zr), where RE consists of mischmetal (essentially Nd). If we suppose, that analyzed precipitates have in reality DO_{19} crystallographic structure, then, the stoichiometric formula for them must be written as $Mg_3(Y_{0.25}Nd_{0.75})$ according to our measurements.

The stoichiometric formula $Mg_3(Y_{0.25}Nd_{0.75})$ enables us to calculate the apparent atomic fractions of precipitated phases as follows:

$$f_a = \frac{N_{prec}^{(Mg)} + N_{prec}^{(Y)} + N_{prec}^{(Nd)}}{N_{tot}} = \frac{N_{prec}^{(Nd)}\,(1 + 0.25/0.75 + 3/0.75)}{N_{tot}}, \tag{3.4.1}$$

where $N_{prec}^{(Mg)}$, $N_{prec}^{(Y)}$, $N_{prec}^{(Nd)}$ is the number of Mg, Y, Nd atoms involved into precipitation, respectively; N_{tot} total number of atoms in the investigated volume.

If one supposes that only Nd atoms were identified correctly by the CI method, then the number of Y and Mg atoms inside precipitates then can be adjusted to the pre-assumed stoichiometry $Mg_3(Y_{0.85}Nd_{0.15})$ and apparent atomic fraction is calculated as follows:

$$f_a = \frac{N_{prec}^{(Nd)}\,(1 + 0.85/0.15 + 3/0.15)}{N_{tot}}. \tag{3.4.2}$$

The atomic fractions calculated for the different stoichiometric formulas are given in Table 3.4.2.

Time, h	Eq. 3.4.1 $Mg_3(Y_{0.25}Nd_{0.75})$ f_a, %:	Eq. 3.4.2 $Mg_3(Y_{0.85}Nd_{0.15})$ f_a, %:	WE43 [Ant03] f_v, %:	N_ν, $\times 10^{23}$nm^{-3}
168	0.6	2.7	-	24.4 ± 3.9
864	1.2	5.4	5.4	21.9 ± 3.7
1324	1.3	6.1	6.7	23.1 ± 3.8

Table 3.4.2: Evolution of atomic fraction, f_a, of precipitates during aging calculated from the number of solute elements involved into precipitation using the two stoichiometric formulas according to Eq. 3.4.1 and 3.4.2. Third column gives the precipitate volume fraction measured by Antion et al. [Ant03] for commercial WE43 alloy under the supposition of $Mg_3(Y_{0.85}Nd_{0.15})$ precipitate stoichiometry. In the last column the measured precipitate number density, N_ν, is provided.

It is worth noting that the presented atomic fractions can be confronted to volume fractions of Antion et al. [Ant03] obtained under similar heat treatments for commercial WE43 alloy[8]. In their work, Antion et al. [Ant03] have calculated the volume fractions from SAXS data using the Lorimer's [Lor99] stoichiometry: $Mg_3(Y_{0.85}Nd_{0.15})$. As it can be seen from Table 3.4.2, our values of atomic fractions are very close to Antion's one in case of usage of the same composition formula. However, we think that the ratio N_Y^{prec}/N_{Nd}^{prec} calculated directly from APT data is more truthful. There are several reasons to think so:

- pair correlation functions (Figure 3.4.2) show that Nd-Nd pairs demonstrate the strongest positive correlations;
- visual observations of reconstructed APT volumes reveal that Nd atoms form a core of thin precipitates, whereas Y atoms are distributed around (Figure 3.4.4).

The thin slice of reconstructed volume in Figure 3.4.4 also clearly demonstrates that precipitates are elongated in certain direction. Another visualization provided by Figure 3.4.5 gives evidence that precipitates exhibit a plate-like shape, which makes them morphologically similar to those observed in the binary Mg-Nd alloy. The plate-like shape of precipitates in ternary Mg-Y-Nd alloy, which form at the early stages of precipitation, is indicative of the fact that the strain energy effect is far more manifest than the surface effect [Kha83]. In the present study, orientation relationships between precipitates and the matrix could not be identified. However, the strong analogy between precipitation in the model ternary Mg-Y-Nd alloy and that observed in more complex commercial alloy WE43 [Ant03] is expected. In the commercial alloys, thin plate-like

[8]Actually, the comparison is rather approximative because of local magnification affect.

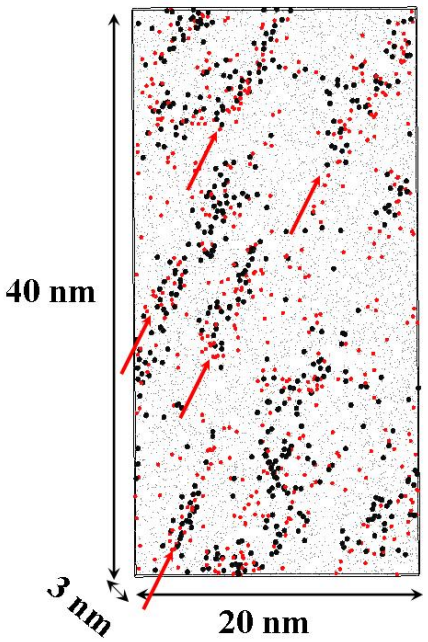

Figure 3.4.4: Thin APT volume reconstructed from an analyzed sample aged at 150°C for 864 h demonstrating the elongation of thin solute-rich precipitates in one certain direction (the crystallographic direction could not be determined from this dataset). Mg atoms are shown as gray points; Nd and Y atoms are black and red spheres, respectively.

DO_{19} precipitates formed in $(1\bar{1}00)$ and $(11\bar{2}0)$ magnesium planes were observed after the same heat treatment. Thus, precipitate morphology detected by APT technique is consistent with TEM results of Antion et al. [Ant03, Ant06].

In Table 3.4.2 the precipitate number density was also given for different aging times. Number of precipitates in every reconstructed volume was calculated manually, as the cluster identification led to the gluing of precipitates due to their high density and blurred interfaces. Value of precipitate number density ranging in the interval 20–25 $\times$ 10^{23}nm^{-3} was found in the analyzed samples. This high and stable value of number density of nano-scale precipitates in ternary alloy, in comparison to that measured in the binary alloy (provided in the previous section), probably explains its improved mechanical properties.

3.4.3 Conclusion

A comparison of the nanostructural and compositional evolution of Mg-Y-Nd during phase separation at 150°C for aging times ranging from 168 h to 1324 h was obtained, employing atom probe tomography technique. This binary alloy was designed to study precipitate formation, and subsequently growth and coarsening, leading to the following results:

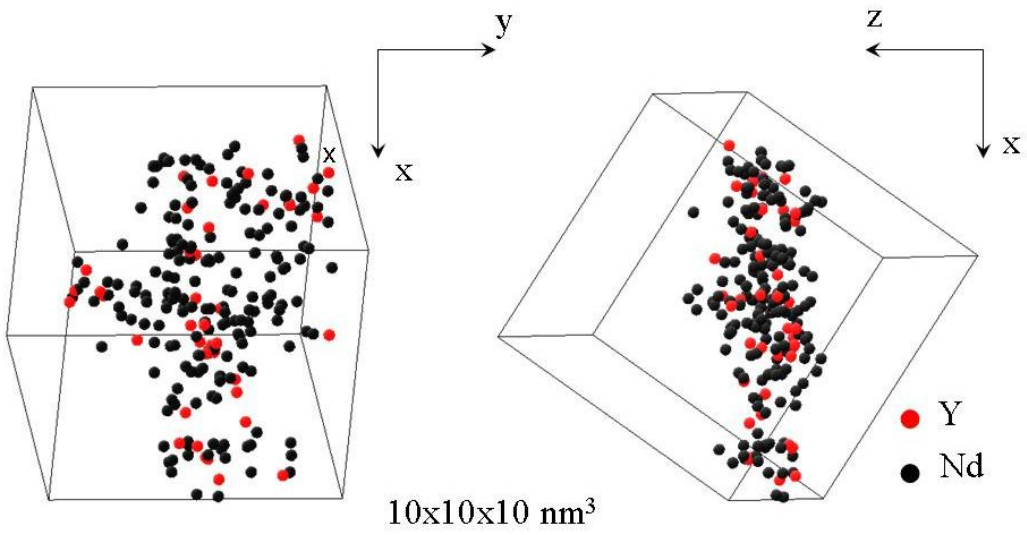

Figure 3.4.5: Typical plate-like solute-enriched precipitate observed in Mg-Y-Nd samples aged at 150°C for times greater than 864 h. Mg atoms are not shown for clarity.

- Both Neodymium and Yttrium are involved into formation of atomic heterogeneities and later precipitates in the Mg-Y-Nd alloy.
- The plate-like shape of particles formed at late aging times (> 864 h) can be recognized.
- Y atoms significantly slow down the phase separation process in comparison to the one in binary alloy. The participation of Y atoms in the formation of atomic heterogeneities becomes evident only after a very long aging times, typically after 864 h.

References

Ant03. C. Antion, P. Donnadieu, F. Perrard, A. Deschamps, C. Tassin, A. Pisch, *Acta Materialia*, **51**(18):5335 (2003).

Ant06. C. Antion, P. Donnadieu, C. Tassin, A. Pisch, *Philosophical Magazine*, **86**(19):2797 (2006).

Del90. S. Delfino, A. Saccone, R. Ferro, *Metallurgical and Materials Transactions A*, **21**(8):2109 (1990).

Dri63. M. Drits, Z. Sviderskaya, L. Rokhlin, *Met. Metalloved., Fiz. Khim. Metody Issled.*, **12**:143 (1963).

Geu05. F. D. Geuser, Ph.D. thesis, Université de Rouen (2005).

Gor05. S. Gorsse, C. Hutchinson, B. Chevalier, J.-F. Nie, *Journal of Alloys and Compounds*, **392**(1-2):253 (2005).

Gra70. K. Gradwell, Ph.D. thesis, University of Manchester (1970).

Has09. H. S. Hasting, A. G. Froseth, S. J. Andersen, R. Vissers, J. C. Walmsley, C. D. Marioara, F. Danoix, W. Lefebvre, R. Holmestad, *Journal of Applied Physics*, **106**(12):123527 (2009).

His02. M. Hisa, J. Barry, G. Dunlop, *Philosophical Magazine A*, **82**(3):497 (2002).

Kar85. H. Karimzadeh, Ph.D. thesis, University of Manchester (1985).

Kha83. A. G. Khachaturyan, *Theory of structural transformations in solids*, Wiley, 1983.

Kin82. D. R. Kingham, *Surface Science*, **116**(2):273 (1982).

Lan86. L. Landau, E. Lifshitz, *Theory of Elasticity*, volume 7 of *Course of Theoretical Physics*, Pergamon Press, Oxford, 1986, 3 edition.

Lor86. G. Lorimer, in *Proc. London Conf. on Magnesium Technology*, edited by G. L. C. Baker, W. Unsworth, p. 47, The Institute of Metals, London, 1986.

Lor99. G. Lorimer, R. Azari-Khosroshahi, M. Ahmed, in *Japan Institute Of Metals, Proceedings, (jimic-3), Pts 1 And 2 - Solid - Solid Phase Transformations*, edited by M. Koiwa, K. Otsuka, T. Miyazaki, volume 12, pp. 185–192, Japan Inst Metals, 1999.

Men07. F. gui Meng, H. shan LIU, L. bin LIU, Z. peng JIN, *Transactions of Nonferrous Metals Society of China*, **17**(1):77 (2007).

Mil02. M. Miller, *Atom Probe Tomography Plenum Publishers*, New York, 2002.

NH88. A. Nayeb-Hashemi, J. Clark, *Journal of Phase Equilibria*, **9**(5):618 (1988).

Nic71. R. Nicholson, *Strengthening Methods in Crystals*, Elsevier, London, 1971.

Oka91. H. Okamoto, *Journal of Phase Equilibria*, **12**(2):249 (1991).

Oka07. —, *Journal of Phase Equilibria and Diffusion*, **28**(4):405 (2007).

Par57. J. Park, L. Wyman, *Phase relationships in magnesium alloys*, Wacd, Wright Patterson Air Force Base, Ohio (1957).

Pik73. T. Pike, B. Noble, *Journal of the Less Common Metals*, **30**(1):63 (1973).

Pin03. D. H. Ping, K. Hono, J. F. Nie, *Scripta Materialia*, **48**(8):1017 (2003).

Rok62. L. Rokhlin, *Izv. Akad. Nauk. SSSR, Otd. Tekh. Nauk, Met. Toplivo*, **2**:126 (1962).

Sav58. Y. Savitskii, V. Terekhova, I. Novikova, *Zh. Neorg. Khim.*, **3**(9):2138 (1958).

Vur00. F. Vurpillot, A. Bostel, D. Blavette, *Applied Physics Letters*, **76**(21):3127 (2000).

Wau76. A. Waugh, E. Boyes, M. Southon, *Surface Science*, **61**(1):109 (1976).

Wei96. L. Wei, G. Dunlop, H. Westengen, *Journal Of Materials Science*, **31**(2):387 (1996).

Wen81. S. Wen, E. Kostlan, M. Hong, A. Khachaturyan, J. W. Morris, *Acta metall*, **29**:124 (1981).

Wen99. Y. H. Wen, Y. Wang, L. Q. Chen, *Acta Materialia*, **47**(17):4375 (1999).

Wil03. R. Wilson, C. Bettles, B. Muddle, J. Nie, in *Magnesium Alloys 2003, Pts 1 And 2*, edited by Y. Kojima, T. Aizawa, K. Higashi, S. Kamado, volume 419-4 of *Materials Science Forum*, pp. 267–272, Trans Tech Publications Ltd, 2003.

4 Monte-Carlo simulation technique.

4.1 Master equation

Let us consider an isolated macroscopic system at a moment t. The probability to observe a state $\aleph$ of the system at time t is $P(\aleph, t)$. The evolution of the probabilities $P(\aleph, t)$ is given by the master equation:

$$\frac{\partial P(\aleph, t)}{\partial t} = \sum_{\aleph'} W(\aleph' \to \aleph) P(\aleph', t) - \sum_{\aleph}{}' W(\aleph \to \aleph') P(\aleph, t), \tag{4.1.1}$$

where $W(\aleph \to \aleph')$ (respectively $W(\aleph' \to \aleph)$) gives the probability of transition by unit time from the state $\aleph$ to the state $\aleph'$ (respectively $\aleph'$ to the state $\aleph$). Once the mechanism of atomic exchange is chosen the transition probabilities can be calculated, as it will be explained in next section.

At equilibrium, the probability to find the system in a state $\aleph$ does not depend on time, hence $\frac{dP(\aleph,t)}{dt} = 0$ and the distribution of probabilities of the equilibrium state is the stationary solution of the master equation:

$$\sum_{\aleph} W(\aleph \to \aleph') P(\aleph, t) = \sum_{\aleph} W(\aleph' \to \aleph) P(\aleph', t).$$

This equation is called the *the detailed balance condition.* If the transition probabilities $W(\aleph \to \aleph')$ respects this condition and "H theorem" of Boltzmann (which shows that the spontaneous evolution of an out-of-equilibrium microscopic system tends uniquely towards equilibrium) the master equation converges toward the equilibrium state whatever the initial distribution is.

One of the ways to get the solution of the master equation 4.1.1 is to use a Monte-Carlo method. Under its dynamical interpretation, the Monte-Carlo method provides a numerical solution to the Eqn. 4.1.1.

4.2 Cohesive model.

To have a success in the solution of the master equation (4.1.1) by a Monte-Carlo method, one should determine the transition probabilities $W(\aleph \to \aleph')$, which are closely related to the energy of the system.

The energy associated to each configuration of the system is calculated obeying following

hypothesis:

1. The internal energy of a system is a sum of three independent terms:

$$E = E_{conf} + E_{vib} + E_{electr},$$

where E_{conf} is the configuration energy which actually depends on the distribution of atoms, E_{vib} is the vibration energy of atoms and E_{electr} is internal energy of atoms originates from the interaction of constituents of an individual atom (in particular electron-core interactions).

In practice, we suppose that E_{vib} and E_{electr} do not change with the atomic configuration of a system. In this case, the important member is E_{conf}. In order to determine the configuration energy of a system, it is necessary to know interactions (or cohesive model) between atoms.

2. Cohesive model: confining ourself to the Ising type models on the rigid lattices we suppose that the configuration energy is equal to the sum of pair potentials:

$$E_{conf} = \frac{1}{2}\sum_{i}^{n}\sum_{X,Y} N_{XY}^{(i)} V_{XY}^{i},$$

where $N_{XY}^{(i)}$ and V_{XY}^{i} represent the number and interaction potentials of pairs of atoms $X-Y$ respectively placed on i^{th} neighboring sites. The summation is performed by first neighbors taken into the consideration and by all atomic species presented into the system.

4.3 The Monte-Carlo method in the semi-grand canonical ensemble (MCGE).

The Monte-Carlo methods consists of generating a series of equilibrium configurations of a finite-sized computer crystal. Using the present MC method, for a given thermodynamic of a system, the phase boundaries of the existing phases can be determined by a series of calculations. Hence, the phase diagram can be constructed.

In the semi-grand canonical ensemble the system is opened: the total number of sites (volume) is fixed, but it can exchange A and B atoms with the reservoirs. The composition of the system can therefore change. Hence, the set of external parameters consists of the temperature, the numbers of atoms of every type and the chemical potentials of species. The phase diagram boundaries can

be directly evaluated (without calculation of additional parameters, like order parameters, etc.) in this ensemble and, hence, the phase diagram can be plotted.

At equilibrium, the probability to observe a configuration ℵ is given by:

$$P(\aleph) = \exp\left(-\frac{E_{conf} - \sum N_i \mu_i}{k_B T}\right), \tag{4.3.1}$$

where μ_i and N_i are the chemical potential and number of atoms of element of type i, respectively.

Knowing $P(\aleph)$, it is possible to determine the probability to exchange an atom A situated on a particular site of the lattice by an atom B from the reservoir of particles. This probability is given by:

$$P_{AB} = \exp\left(-\frac{\Delta E - \Delta\mu_{AB}}{k_B T}\right), \tag{4.3.2}$$

where $\Delta\mu_{AB} = \mu_B - \mu_A$ is the difference between chemical potentials of the two species. The term ΔE corresponds to the difference of configuration energy induced by the exchange. It can be expressed in terms of the ordering energies ω^j defined as follows

$$\omega^j = V^j_{AA} + V^j_{BB} - 2V^j_{AB}, \tag{4.3.3}$$

where V^j_{XY} is pair potential interaction between atoms of type X and Y. Index j here denotes the atomic shell.

At a constant temperature T, varying the value of $\Delta\mu_{AB}$ and calculating the composition of the system after equilibration, which is defined by the slope of Gibb's free energy ,as it is seen from Figure 4.3.1, i.e. by $\Delta\mu_{AB}$, one can plot the dependence of the composition from the chemical potential difference. The tie-line is then obtained as shown in Figure 4.3.1b. Figure 4.3.1b demonstrates that, when the value of $\Delta\mu_{AB}$ is less than the equilibrium value, $\Delta\mu^{eq}_{AB}$, only one phase is stable. In the other case, when it is higher than the equilibrium value the other phase is observed. At the certain point, where $\Delta\mu_{AB} = \Delta\mu^{eq}_{AB}$ we observe a composition jump. It is worth to mention here that for first order transition the hysteresis is usually observed, i.e. a shift of the composition jump appears depending on if we perfrom our simulation from disordered state of the system to the ordered one or vice versa. This question will be highlighted in the section of results.

The algorithm to simulate a tie-line is following:

1. Chose a random site on the rigid lattice. This site is occupied by an atom of type X.

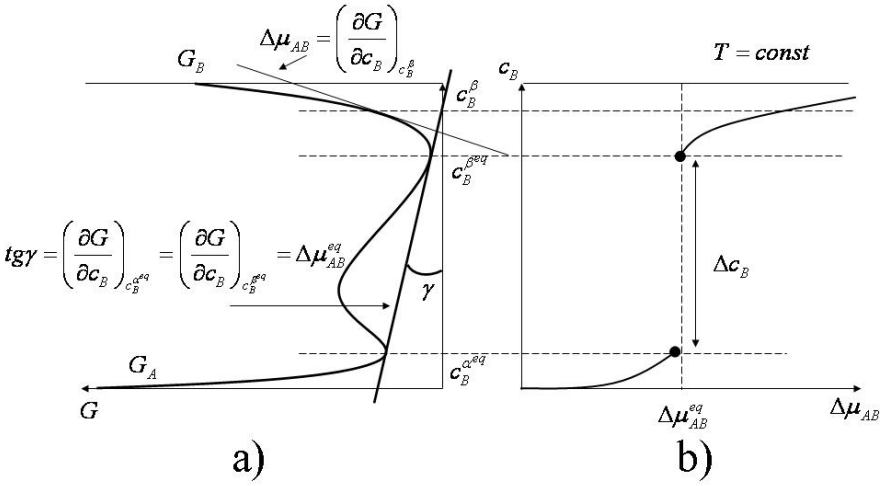

Figure 4.3.1: a) schematic curve of Gibb's free energy of an $A-B$ system at a temperature T; b) corresponding tie-line construction.

2. Calculate the probability P_{XY} to exchange X by Y.

3. Generate a random number r from the interval]0..1[.

4. If $r < P_{XY}$ perform the exchange.

5. Come back to the first step until the system asymptotically reaches the equilibrium composition fixed by $\Delta\mu_{AB}$.

6. Change the $\Delta\mu_{AB}$ value and repeat steps 1-5.

If one generates a sequence of tie-lines at different temperatures, the phase diagram can be then plotted.

4.4 The Kawasaki dynamics.

4.4.1 Principle of the Kawasaki dynamics.

Kawasaki dynamics deals with a system consisting of an array of N coupled atoms. The coupling between the atoms is represented by a set of probabilities of atomic exchange. The atoms may undertake direct exchange with their nearest neighbors, and in this way the system

evolves while the total concentration remains conserved. By fixing the temperature of the system, we are then able to model the canonical ensemble of particles.

The change of configuration energy of the binary system due to the atomic flip in case of our cohesion model (see Sec. 4.2) can be described in terms of pair interactions:

$$\Delta E_{conf} = \omega^1(n^{(1)}_{B(A)} - n^{(1)}_{B(B)} - 1) + \sum_{i>1} \omega^i(n^{(i)}_{B(A)} - n^{(i)}_{B(B)}), \tag{4.4.1}$$

where ω^i are ordering energies given by Eqv. (4.3.3); $n^{(i)}_{B(A)}$ and $n^{(i)}_{B(B)}$ are the numbers of B atoms in the i^{th} shell of an atom A or B respectively before an exchange. Here the summation goes by atomic shells.

The described procedure pushes the system toward its equilibrium. However, intermediate states obtained during the simulation normally do not necessarily correspond to the real physical kinetic pathways, as the mechanism of the direct atomic exchange is highly unlikely.

4.4.2 The Metropolis algorithm.

In order to carry out one atomic exchange in the Kawasaki dynamics, the well known Metropolis algorithm [Met53] can be used. To perform the transition from a state $\aleph$ to the state $\aleph'$ of the system according to the algorithm one needs compute the energy change $\Delta E_{conf} = E(\aleph') - E(\aleph)$ resulting from the configurational change. The transition probability

$$P = \exp\left(-\frac{\Delta E_{conf}}{k_B T}\right),$$

is then compared to a random number r, chosen uniformly from the interval $]0..1[$. If $P > r$ the transition is performed; otherwise the old configuration $\aleph$ is kept and another transition is tried.

One Monte-Carlo step (MCS) corresponds to the following sequence of operations:

1. Choose a nearest-neighbor pair of atoms at random.
2. Calculate the energy change ΔE_{conf} that the atomic exchange would entail.
3. If $\Delta E < 0$ carry out the exchange, else generate a random number r and if $\exp\left(-\frac{\Delta E}{k_B T}\right) > r$ carry out the exchange.
4. Come back to the step 1.

4.5 Atomistic kinetic Monte-Carlo method (AKMC).

4.5.1 Atomistic kinetic model.

The atomic diffusion in metallic materials usually occurs by the vacancy mechanism. In a real crystal the jump of an atom toward the neighboring vacancy site is carried out by the lattice vibration. The atom is able to jump once it has enough thermal energy to overcome the energy barrier which exists between its position and the saddle-point position. From the theory of rate processes, in quasi-harmonic approximation at constant temperature and volume, the jump frequency of an atom X on a neighboring vacant site is given by [Boc96]

$$W_{XV} = \nu_X \exp\left(-\frac{\Delta E^{act}_{XV}}{k_B T}\right), \tag{4.5.1}$$

Here ν_X is pre-exponential term:

$$\nu_X = \frac{\prod_{k=1}^{3N-3} \nu_k^{init}}{\prod_{k=2}^{3N-3} \nu_k^{sp}},$$

where N is the number of atoms in the system; ν_k^{init} are the $3N-3$ normal modes in the initial (stable) position and ν_k^{sp} are the $3N-4$ modes in the saddle-point position. The pre-exponential term cannot be directly estimated because of the rigid lattice restriction, so it is replaced by constant value, ν_X, (the attempt frequency), which in our model depends only on the nature of a jumping atom. ΔE^{act}_{XV} is the activation barrier of the jump. It is considered as it is shown by Figure 4.5.1 to be equal to $\Delta E^{act}_{XV} = E_{sp} - E_i$. Equivalently, the latter can be rewritten in the form $\Delta E^{act}_{XV} = e^X_S - \Delta E_{conf}$, where e^X_S is the binding energy of the atom X at the saddle-point position.

ΔE_{conf}, according to our cohesive model is the energy of the bonds which are broken during the jump. In this cut bond model [SP97,Bou02,Soi96] the activation energy can be finally written in the form:

$$\Delta E^{act}_{XV} = e^X_S - \sum_Y V_{XY} - \sum_{Y \neq X} V_{VY}, \tag{4.5.2}$$

the summations correspond to the bonds which are broken during the jump.

In the method described above, only initial state and height of the energy barrier to overcome

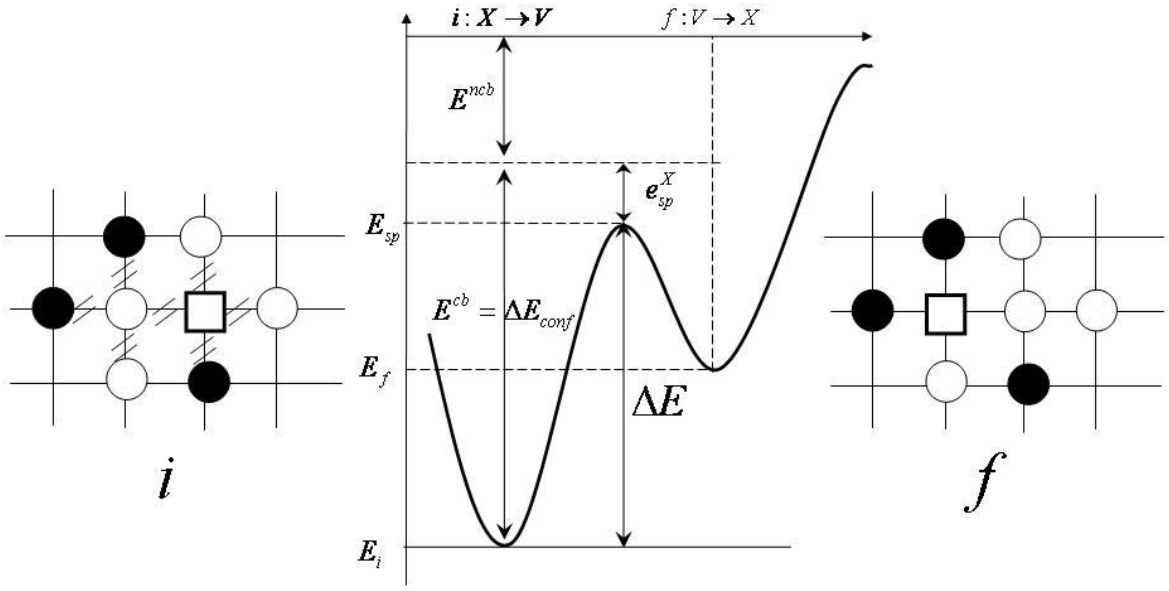

Figure 4.5.1: The activation energy for the jump frequency. "**cb**" means "cut bonds" and "**ncb**" - not cut bonds.

are taken into account. The final state of the system after the jump is ignored. Hence, the value of the energy barrier controls the frequency of the jumps.

4.5.2 Residence time algorithm.

The diffusion occurs by vacancy exchanges with nearest-neighbor atoms. The corresponding jump frequencies W_{XV} are given by Eqn. (4.5.1). At each Monte-Carlo step, one of the Z possible vacancy jumps is chosen according to the residence time algorithm [Soi96]: to leave a given configuration $\aleph$, the system can undergo Z possible vacancy jumps of frequencies: $W_1(\aleph)$, $W_2(\aleph) \ldots W_Z(\aleph)$ (normally Z is the number of first nearest neighbors of a lattice site). After a time t, the probability that the system is still in the configuration $\aleph$ is given by

$$P(\aleph, t) = \exp\left\{-\frac{t}{\tau(\aleph)}\right\}$$

with

$$\tau(\aleph) = \left\{\sum_{i=1}^{Z} W_i(\aleph)\right\}^{-1}.$$

Thus, at every step one can either add a mean increment $\tau(\aleph)$ or generate a random number $r =]0..1[$ and add an increment $t = -\tau(\aleph)\ln r$. For a sufficiently large system the two methods

are equivalent.

Finally the algorithm can be described as follows:

1. Calculate all the Z possible transition probabilities $\{W_i, i = 1..N\}$;
2. Generate a random number r from the interval $]0..1[$;
3. Choose the k^{th} transition among N possible, so that $\frac{\sum_{i=1}^{k} W_i}{W} \leq r < \frac{\sum_{i=k+1}^{N} W_i}{W}$, where $W = \sum_{i=1}^{N} W_i$.
4. Come back to the step 1.

In the standard Metropolis algorithm, a vacancy jump is randomly chosen, and exchange is carried out according to the procedure described in Sec.4.4. The rejection rate dramatically increases at low temperature and then the Metropolis algorithm becomes inefficient. On the contrary, with the residence time algorithm, one transition is performed at each step even at very low temperature: so it stays efficient. In addition, a physical time is attached to every MC step.

4.5.3 Absolute time scale.

A kinetic pathway of a simulated system is defined by the sequence of configurations the system goes through and the time at which the system reaches each of these configurations. In turn, the time scale depends on the jump frequencies (Eqn. (4.5.1)) and also on the vacancy concentration. Therefore, to relate the physical time to the time obtained in a Monte-Carlo simulations, we have to take into account that the vacancy concentration in the simulation box is usually greater than the experimental one. Under the usual assumption that the vacancy-vacancy interaction can be neglected, the physical time t_S related to one Monte-Carlo step is

$$t_S = \tau \frac{c_V^{MC}}{c_V^{expt}}, \tag{4.5.3}$$

where c_V^{expt} and c_V^{MC} are the vacancy concentration in the matrix of real alloy and in a simulation box, respectively.

During isothermal aging, we may assume that the vacancy concentration in the matrix is

always close to the equilibrium one, so that

$$c_V^{expt} \simeq \exp\left[-\frac{E_V^f}{k_B T}\right], \tag{4.5.4}$$

where E_V^f is the vacancy formation energy in matrix.

In our simulation box, we introduce only one vacancy. So the average vacancy concentration in the simulation box is then simply

$$c_V^{MC} = 1/N, \tag{4.5.5}$$

where N is the number of atomic sites of the box.

4.6 Description of Monte-Carlo data treatment methods.

In order to characterize the simulated data, it is quite important to have proper data treatment techniques. Since processes of ordering and phase separation, even in binary system may be quite complex, it is necessary to use several methods simultaneously and to compare their results in order to obtain a physical comprehension of the kinetics. Moreover, one class of methods can be useful and informative at, for example, first stages of phase transition process and others — at later ones.

4.6.1 Warren-Cowley parameters.

Warren-Cowley parameters [Cow50] are defined to characterize the short-range order (SRO) in alloys. Discrete SRO parameters for the i^{th} shell of B are defined as following:

$$\alpha_{AB}^i = 1 - \frac{P^i(A|B)}{P^i(A)}, \tag{4.6.1}$$

where $P^i(A|B)$ is the probability to observe an atom A in the i^{th} shell of an atom B and $P^i(A)$ is the probability to observe an atom A in a random system with the same composition.

If an alloy has a tendency to ordering then α_{AB}^1 is negative, in case of clustering α_{AB}^1 is positive.

The short-range order parameters being initially defined in this way for convenience in consideration of the x-ray diffraction effects for alloys above the critical temperature of ordering, were found to be also useful for thermodynamic considerations and for various Monte-Carlo simulations

above the critical temperature and below as-well [Cow50, Cow60, Cow65, Fli61, Par99].

In case of appearance of ordered $D0_{19}$ structure, which is studied in this work, one can predict the limiting values of Warren-Cowley parameters in a binary system with compositions c_A and c_B of elements A and B, respectively. The limit values of α's until the third atomic shell are presented in Table 4.6.1.

α^1_{AB}	α^2_{AB}	α^3_{AB}
$-\frac{c_B}{c_A}$	1	1

Table 4.6.1: Limit values of Warren-Cowley SRO parameters for in a system with DO_{19} type ordering.

4.6.2 Long-range order parameter and diffraction pattern.

According to the general theory of x-ray diffraction on crystals [Kri69, Kha83], the scattered radiation intensities are proportional to squares of scattered wave amplitude moduli:

$$I(\vec{q}) = |Y(\vec{q})|^2 , \tag{4.6.2}$$

where $\vec{q}$ is the diffraction vector (the vector difference between the wave vectors of the incident and scattered waves) and the mean scattering amplitude for a binary substitutional solution is given by the relation:

$$\langle Y(\vec{q})\rangle = \bar{f}\sum_{\vec{r}} e^{-i\vec{q}\vec{r}} + (f_B - f_A)\sum_{\vec{r}}(n(\vec{r}) - c)e^{-i\vec{q}\vec{r}}. \tag{4.6.3}$$

Where c is the atomic fraction of solute atoms, f_A and f_B are the atomic scattering factors of solvent and solute atoms respectively, $\bar{f} = (1-c)f_A + cf_B$ is the average atomic scattering factor and $n(\vec{r})$ is the occupation probability of finding a solute atom at the site $\vec{r}$.

Let us consider a case of Bravais lattice (in case of a complex lattice consisting of several inter-penetrated lattices, like *hcp*-lattice, theory is simply expendable). The first term in Eq. 4.6.3

$$Y_0(\vec{q}) = \bar{f}\sum_{\vec{r}} e^{-i\vec{q}\vec{r}}$$

then describes the coherent amplitude responsible for the disordered crystal reflections (fundamental reflections) since $Y_0(\vec{q})$ is independent of atomic configurations and, hence, takes nonzero

values at fundamental reciprocal lattice points only.

The second term in Eq. 4.6.3

$$Y_1(\vec{q}) = (f_B - f_A) \sum_{\vec{r}} (n(\vec{r}) - c) e^{-i\vec{q}\vec{r}} \tag{4.6.4}$$

describes the coherent scattering amplitude corresponding to the superlattice reflections that vanish in the disordered state, when $n(\vec{r}) = c$.

In an ordered solution, the function $n(\vec{r})$ becomes dependent on the site coordinates, r, and can be expanded in a Fourier series:

$$n(\vec{r}) = c + \sum_j Q(\vec{k}_j) e^{i\vec{k}_j\vec{r}}, \tag{4.6.5}$$

where k_j are the wave vectors and $Q(\vec{k}_j)$ the Fourier coefficients. Substituting Eq. 4.6.5 into Eq. 4.6.4, it is possible to obtain:

$$Y_1(\vec{q}) = (f_B - f_A) \sum_j Q(\vec{k}_j) \sum_{\vec{r}} e^{-i(\vec{q}-\vec{k}_j)\vec{r}}. \tag{4.6.6}$$

One can see that, since

$$\sum_{\vec{r}} e^{-i(\vec{q}-\vec{k}_j)\vec{r}} = \begin{cases} N & \text{if } q - \vec{k}_j = 2\pi\vec{H} \\ 0 & \text{otherwise} \end{cases}$$

the scattering amplitude is nonzero only at reciprocal lattice points:

$$\vec{q} = 2\pi\vec{H} + \vec{k}_j,$$

where $\vec{H}$ is the reciprocal lattice vector related to the set of crystal lattice sites. The latter expression describes the superlattice reflections. Also Eq. 4.6.6 reveals a very important fact: the amplitude of a superlattice reflection is always proportional to the amplitude of the corresponding static concentration wave $Q(\vec{k}_j)$ which in turn is proportional to the corresponding long-range order parameter $\eta_{\vec{k}_j}$ [Kha83].

Thus, to follow the evolution of the LRO in the system, one needs to compute the structure

factor, i.e. the Fourier transform of atomic-site occupancies:

$$S(\vec{q}) = |Y_1(\vec{q})|\,, \tag{4.6.7}$$

where summation goes over all atomic sites. The integrated intensity of the superlattice reflection is given by

$$I_{\vec{q}_{ss}} = \sum_{\vec{q}\in\omega} S(\vec{q}), \tag{4.6.8}$$

where the volume ω is chosen so as to contain vectors such as $\left|\vec{k} - \vec{k}_{ss}\right| < \xi \left|\vec{k}_{ss}\right|$ and ξ is chosen in such a way to cover all region of superstructure reflection. The degree of order η is then defined by $\eta = \sqrt{I/I_{po}}$, where I_{po} is the superstructure intensity of a perfectly ordered superstructure.

The Fourier transform of a configuration of atoms obtained in a Monte-Carlo simulation described by the Eq. 4.6.4 can be done using the effective Fast Fourier Transform (FFT) algorithm.

4.6.3 Local order parameter.

In order to follow the evolution of the order field, one has to define this field by performing some local averaging of atomic occupancies. This averaging is performed here on the first three shells of neighbors.

The parent *hcp*-lattice may be subdivided into 8 simple hexagonal sublattices. Then, in order to describe the symmetry of the ordered $D0_{19}$ superstructure one need to define 6 α- and 2 β-sublattices, which in case of the perfect $D0_{19}$ would be occupied by only A- and only B-atoms, respectively. There are 4 translation equivalent ways to define α- and β-sublattices, as shown in Figure 4.6.1.

Around a site i, we define a cell Ω_i formed by the site itself, its twelve first-, six second- and two third nearest neighbors. Partial order η_i on a site i is then given by:

$$\eta^i = \frac{1}{4}\frac{r_B^i - c_B}{c_A} + \frac{3}{4}\frac{r_A^i - c_A}{c_B}, \tag{4.6.9}$$

where $r_A^i = N_A^\alpha/N^\alpha$ and $r_B^i = N_B^\beta/N^\beta$ are the relative probabilities of occupation of α-sites by A-atoms, and β-sites by B-atoms, respectively; c_A and c_B the concentrations of A- and B-atoms in the alloy, respectively. Due to existence of 4 translation variants of $D0_{19}$ superstructure (4 ways to

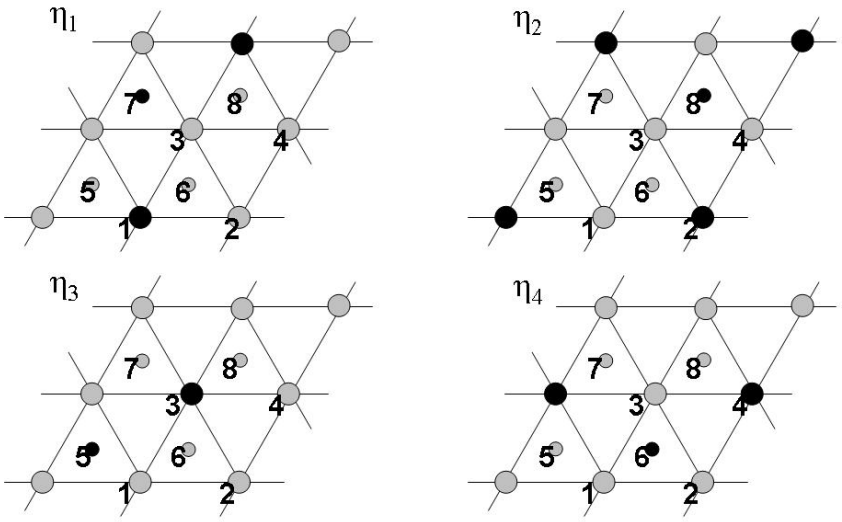

Figure 4.6.1: The 4 translation variants of the $D0_{19}$ superstructure are shown, as defined relatively to the parent *hcp*-lattice. The atoms of an elementary DO_{19} supercell are marked by figures (from 1 to 8). Every atom from the supercell, being shifted on $2\vec{a}_1$, $2\vec{a}_2$ or $\vec{a}_3$, where $\vec{a}_i$ are the *hcp* base vectors, generates a simple hexagonal sublattice, of the parent *hcp*-lattice. In case of perfectly ordered DO_{19} every sublattice is monoatomic (occupied either by A- or by B-atoms). A-atoms are shown as gray circles, B atoms are in black. Small circles correspond to lower basal plane of *hcp*-lattice and the bigger ones to upper one.

define α and β sublattices), then for every site one can calculate 4 local order parameters. Among this 4 parameters the one which has the largest value is associated with the atomic site. This way, the calculated according to Eq. 4.6.9 local order parameter ranges in the interval 0..1.

4.6.4 Precipitate analysis.

Once the precipitation reaction goes for a long time and the formation of precipitates becomes evident, one is able to identify the individual clusters of the new phase. When clusters are identified, it is possible to measure their composition, volume fraction, size characteristics and other useful parameters.

In the presented work, we used the standard cluster identification (CI) algorithm (see Section 2.3.1), which have been tested and successfully used for years in the analysis of Tomographic Atom probe data and in general can be applied to the data simulated by the Monte-Carlo methods.

Once clusters of the new phase(s) are identified, the sizes of these clusters may be estimated from the distances of the atoms from the center of the body. One common measure is the *gyration*

radius (which is a good characteristics for spherically shaped particles). It is given by

$$R_g = \sqrt{\frac{\sum_i m_i(\vec{R}_i - \vec{R}_c)^2}{\sum_i m_i}}, \tag{4.6.10}$$

where $\vec{R}_i$ are the coordinates of an i^{th} atom, $\vec{R}_c = \frac{1}{N}\sum_i m_i \vec{R}_i$ are the coordinates of center of masses of the cluster and m_i are the masses associated with atoms. The summation is performed over all atoms of the cluster. In all cases, unless mentioned, we put m_i equal to 1 independently on the atomic nature. The Eq. 4.6.10 then becomes as follows

$$R_g = \sqrt{\frac{\sum_i (\vec{R}_i - \vec{R}_c)^2}{N}}. \tag{4.6.11}$$

where N is the number of atoms in the cluster. The radius of gyration provides a parameter that is slightly smaller than the actual size of the feature. Therefore, it is common to convert the radius of gyration to an alternative parameter, the Guinier radius, r_G, which represents the actual size of the feature with the use of the following equation

$$r_G = \sqrt{\frac{5}{3}} R_g. \tag{4.6.12}$$

4.6.5 Characteristic length.

The information about clusters size evolution obtained in the direct space is intuitively understandable, but usually is also hardly measurable. Because of the periodic boundary conditions, a precipitate can consist of several parts which are situated by different sides of the simulated box. Another problem, which appears is the cluster coagulation due to the CI procedure. This makes the estimation of the precipitate size a quite tricky task. We are obliged to filter out "split clusters" and manually separate the coagulated ones. Both cases are presented on Figure 4.6.2. These problems may have a dramatic influence on the determination of the mean cluster size, the cluster size distribution and the cluster density.

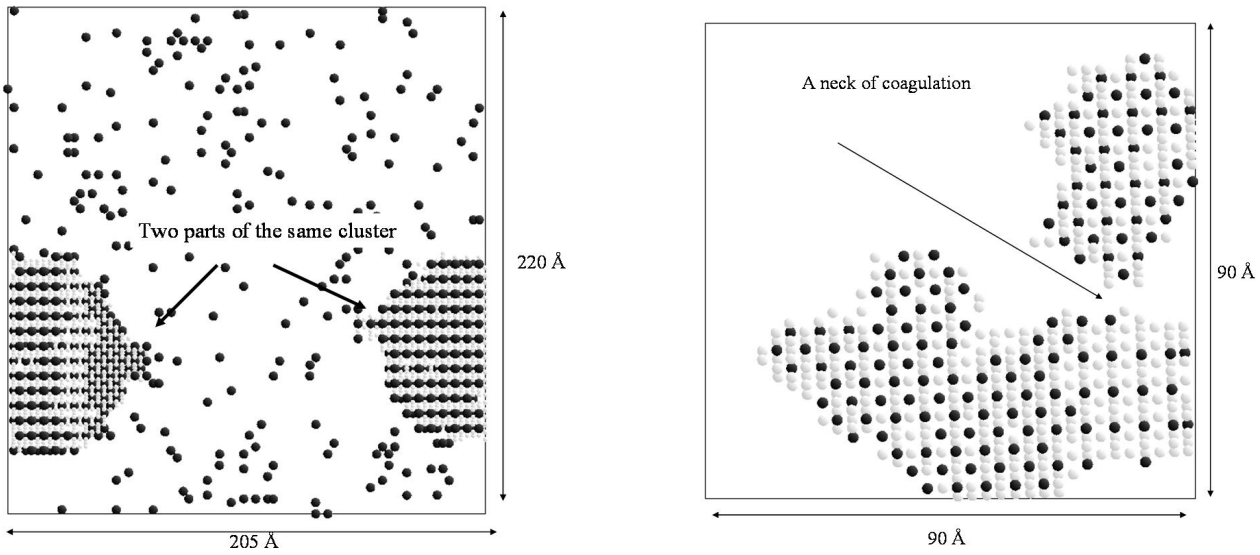

a) b)

Figure 4.6.2: Thin slice of simulated 3D-box representing a) a split cluster due to the boundary conditions b) two clusters identified as one by the CI routine. Black atoms are of type A and the gray ones are of type B. Only B atoms are presented outside clusters for clarity.

An alternative way to measure the characteristic length in a two-phase system is to calculate so-called correlation radius, R_c, defined here as the first zero of the two-point spherically averaged correlation function, $g(r)$. In turn, normally the correlation function is defined as follows:

$$G(\vec{r},t) = \sum_{\vec{r}'} \left(\eta(\vec{r},t) - \bar{\eta}\right)\left(\eta(\vec{r}+\vec{r}',t) - \bar{\eta}\right), \tag{4.6.13}$$

where $\eta(\vec{r},t)$ is the atomic occupation number of the site with coordinates $\vec{r}$ in time t. The occupation number here is equal to 1 if the site is occupied by atom A and -1 if it is occupied by B. And $\bar{\eta} = \frac{1}{N}\sum_{\vec{r}}\eta(\vec{r})$ describes the average composition of the system. To evaluate the spherically averaged correlation function, one needs to carry out the summation over vectors $\vec{r}$ of same modulo:

$$g(r) = \sum_{|\vec{r}|=r} G(\vec{r}). \tag{4.6.14}$$

But in case of the ordered precipitates (Figure 4.6.3a) this direct definition leads to the split of the correlation function in two parts as shown in Figure 4.6.3c. The latter makes impossible the definition of correlation radius.

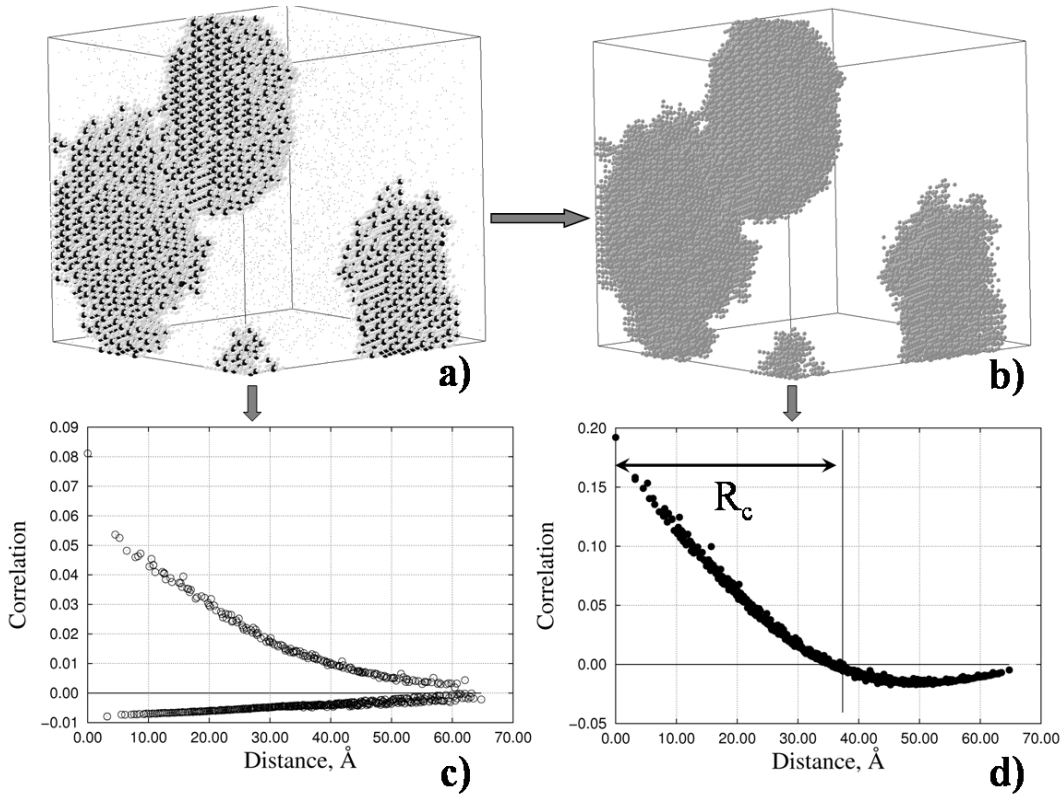

Figure 4.6.3: a) and b) Schematic explanation of a new definition of occupations numbers in a system with ordered precipitates for the correlation function calculation (see text); c) and d) corresponding spherically averaged functions.

In order to calculate the correlation radius, R_c, we first do a cluster identification and then redefine the occupation variables η, according to the following ruler (Figure 4.6.3a and 4.6.3b):

$$\sigma(\vec{r}) = \begin{cases} 1 & \text{if atom at } \vec{r} \text{ inside a cluster} \\ -1 & \text{if atom at } \vec{r} \text{ outside a cluster} \end{cases} .$$

This definition of σ allows to calculate the spherically averaged correlation function and estimate the correlation radius as shown in Figure 4.6.3d.

References

Boc96. J.-L. Bocquet, G. Brebec, Y. Limoge, *Physical Metallurgy*, chapter 7, North-Holland, Amsterdam, 1996.

Bou02. Y. L. Bouar, F. Soisson, *Phys. Rev. B*, **65**(9):094103 (2002).

Cow50. J. M. Cowley, *Phys. Rev.*, **77**(5):669 (1950).

Cow60. —, *Phys. Rev.*, **120**(5):1648 (1960).

Cow65. —, *Phys. Rev.*, **138**(5A):A1384 (1965).

Fli61. P. A. Flinn, G. M. McManus, *Phys. Rev.*, **124**(1):54 (1961).

Kha83. A. G. Khachaturyan, *Theory of structural transformations in solids*, Wiley, 1983.

Kri69. M. A. Krivoglaz, *Theory of X-ray and Thermal-neutron Scattering by Real Crystals*, Plenum, New York, 1969.

Met53. N. Metropolis, A. W. Rosenbluth, M. N. Rosenbluth, A. H. Teller, E. Teller, *The Journal of Chemical Physics*, **21**(6):1087 (1953).

Par99. C. Pareige, F. Soisson, G. Martin, D. Blavette, *Acta Materialia*, **47**(6):1889 (1999).

Soi96. F. Soisson, A. Barbu, G. Martin, *Acta Materialia*, **44**(9):3789 (1996).

SP97. C. Schmuck-Pareige, Ph.D. thesis, Université de Rouen (1997).

5 Monte-Carlo simulation results.

5.1 Phase diagram.

A phase diagram is defined by a set of ordering energies (Eq. 4.3.3). Having an appropriate set of those energies, one can calculate (or simulate) the phase diagram using MCGE. Next section is devoted to the discussion of results obtained by Monte-Carlo simulations in the semi-grand canonical ensemble.

5.1.1 Phase transitions in the close packed hexagonal (*hcp*) lattice. Literature review.

Order-disorder reactions have been studied extensively for binary alloys with the cubic structures, using various methods of simulations and calculations, in particular by MC simulations [Bin81]. Very little work has been done so far for hexagonal alloys.

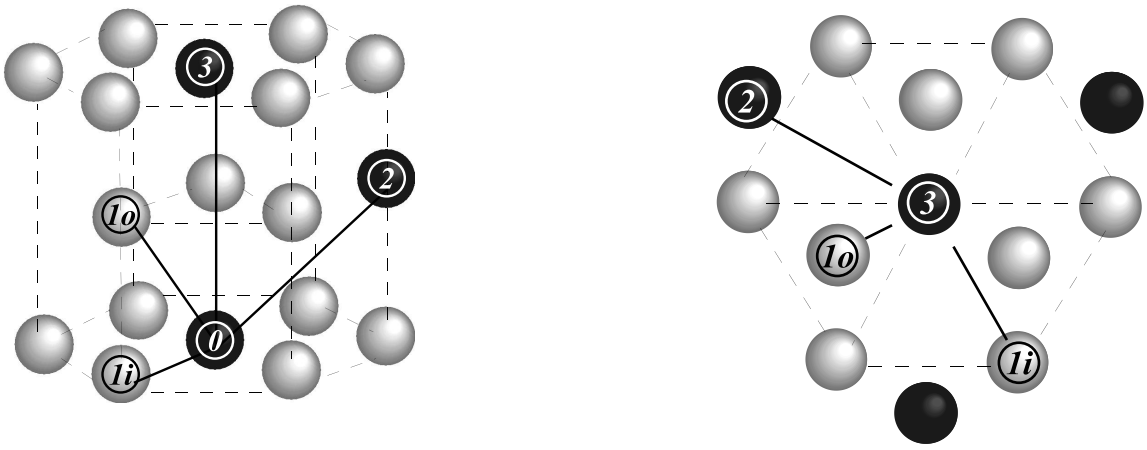

a) b)

Figure 5.1.1: Perspective view a) and top view b) of the $D0_{19}$ ordered structure. The i^{th} neighbors of the 0-atom are denoted by the encircled number i. Black atoms are of type A and the gray ones are of type B.

In the work of Bichara et al. [Bic92], phase diagrams of binary alloys with hexagonal crystal structure have been calculated by means of Monte-Carlo simulations taking into account anisotropic nearest-neighbor interactions. The hcp structure with the ideal ratio $c_0/a_0 = 1.633$ (where a_0, c_0 are the lattice parameters) is topologically equivalent to the *fcc* structure and does not

have difference between the nearest neighbors within the basal plane (0001) (the atom marked "**1i**" on the Fig. 5.1.1) and those between such planes (the atom marked "**1o**" on the Fig. 5.1.1). The equivalence is broken for c_0/a_0 ratios different from the ideal value. The ratio $\xi = \omega_{1o}/\omega_{1i}$, where ω_{1o} and ω_{1i} are the ordering energies corresponding to the in-plane and inter-plane nearest neighbors, may then be taken as a measure of the anisotropy of the system.

Various values of the anisotropy ratio ξ have been assumed in order to produce a series of prototype diagrams. New ordered phases have been revealed (but which have not been observed so far in real systems). However, in the isotropic case ($\xi = 1.0$), the $D0_{19}$ phase (and B19 at high concentrations) is the only coherent stable phase.

In the work of Shimono and Onodera [Shi00], the order-disorder transition in *hcp* binary alloys has been investigated by Monte-Carlo simulations and the renormalization-group methods. Authors complicated the model described above introducing next-nearest neighbor interactions. A set of phase diagrams containing the phase boundary between disordered solid solution (A3) and the two phase region (A3 + $D0_{19}$) has been simulated. The performed Monte-Carlo simulations showed that the second-neighbor interactions play an important role in describing the phase equilibria in *hcp* binary alloy systems: the phase boundary shape was drastically broadening with increasing the modulo of second-neighbor interaction.

We took this work as a reference to obtain the ordering energies to simulate the $A3 \rightarrow A3 + DO_{19}$ reaction by the kinetic Monte-Carlo method.

5.1.2 Results of MC simulations in the semi-grand canonical ensemble.

In our own MC simulations, we have confined ourself to the isotropic case ($\xi = 1$) and supposed the pair interactions going till the third nearest neighbors (Figure 5.1.1). From Figure 5.1.1, it is clearly seen that the $D0_{19}$ structure should appear if the ordering energy of first neighbors is anti-ferromagnetic ($\omega^1 > 0$) and of second and third are ferromagnetic ($\omega^{2,3} < 0$).

An example of simulated tie-line is given Fig. 5.1.2b. For $\Delta\mu$ lower than $\Delta\mu^{eq}$ the disordered phase is observed (Fig. 5.1.2a). For greater values of $\Delta\mu$, the ordered DO_{19}-phase is stable (Fig. 5.1.2c). As expected for a first-order phase transition, a hysteresis is observed. The equilibrium composition of the phases are deduced from the composition jump Δc. The width of the hysteresis gives the uncertainties on these equilibrium compositions. Depending on the tempera-

ture they may have an amplitude of 1 at.%.

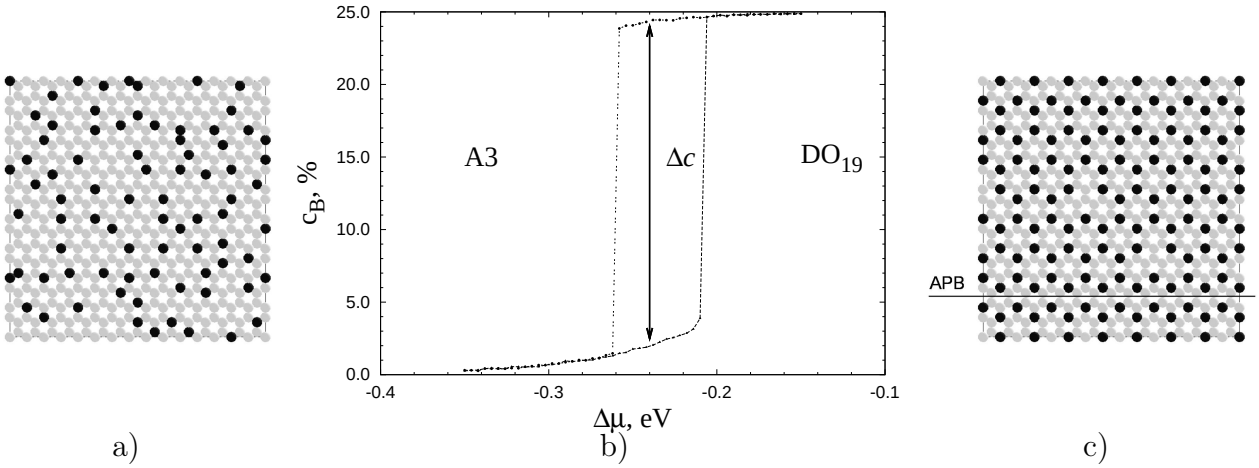

Figure 5.1.2: b) Simulated tie-line as obtained by MC simulation in the semi-grand canonical ensemble at $700K$. Size of the box 27000 atoms; ordering energies: $\omega^1 = 0.14$ eV, $\omega^2 = -0.07$ eV, $\omega^3 = -0.03$ eV. Simulated atoms distributions: a) corresponding to the disordered state of the system; c) corresponding to the ordered state of the system. Two basal planes are shown. A atoms are in gray and B atoms are in black.

Fig. 5.1.2c reveals the presence of an anti-phase boundary (APB) which is marked by a line. This can also (together with the hysteresis effect) affect the determination of the position of the $(A3 + DO_{19})/DO_{19}$ boundary.

In the Monte-Carlo simulations, we have mainly used a simulated box of $30 \times 30 \times 15 \cdot 2 = 27000$ atomic sites with periodic boundary conditions. A larger system ($50 \times 50 \times 25 \cdot 2 = 125000$) has been also used to check possible finite-size effects.

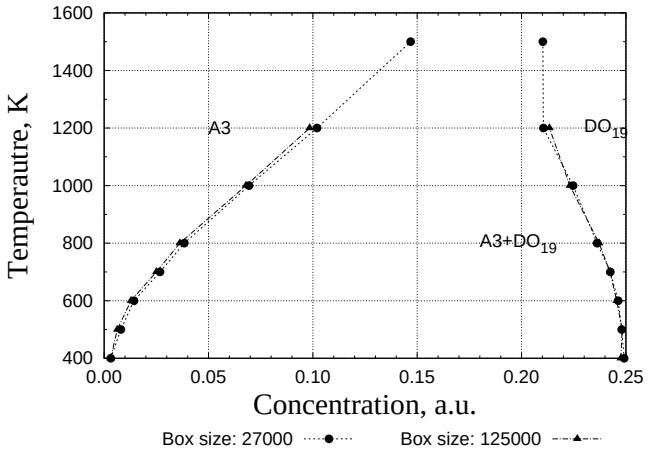

Figure 5.1.3: Dependence of positions of phase boundaries of the phase diagram on the size of the simulation box.

As shown in Figure 5.1.3, comparison of results obtained for $N = 27000$ atoms are in good

agreement with the one obtained in the larger system. This justifies the use of the smaller box, $N = 27000$, for further phase diagram simulations. A smaller box requires a smaller number of MC exchanges to equilibrate the MC system.

Several sets of ordering energies were used to see the influence of next-nearest neighbors interactions on the change of the phase boundaries. These energy sets are listed in Table 5.1.1.

Set	ω^1, eV	ω^2, eV	ω^3, eV
Set 1:	0.14	0.00	0.00
Set 2:	0.14	-0.05	0.00
Set 3:	0.14	-0.07	0.00
Set 4:	0.14	-0.07	-0.03

Table 5.1.1: Tested sets of ordering energies to simulate the phase diagram.

Simulated results (see Fig. 5.1.4) are in a good qualitative agreement with the work of Shimono and Onodera [Shi00]: the addition of second and third neighbor interactions significantly decreases the solubility limit of the $A3$ phase, enlarging the two-phase area of a phase diagram. This effect is quite strong for the second neighbor interactions. This is due to the fact that the number of second neighbor atoms is equal to 6 whereas for third neighbors, only 2 atoms are involved. This induces a large energy gain in case of perfectly ordered structure, and hence makes the decomposition into two phases at a given temperature more energy effective.

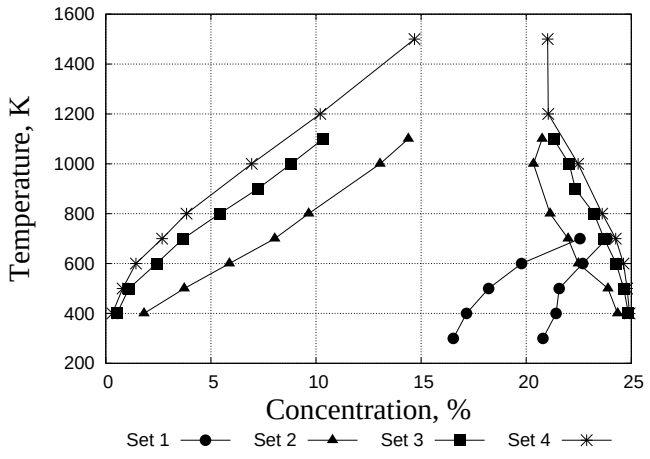

Figure 5.1.4: Phase diagrams simulated for the sets of energies listed in Table 5.1.1

The low solubility of rare-earth atoms in the *hcp*-magnesium indicates the major importance of the next-nearest neighbor effective interactions in those kind of systems.

The set of parameters (**Set 4**, Figure 5.1.4): $\omega^1 = 0.14$ eV, $\omega^2 = -0.07$ eV and $\omega^3 = -0.03$ eV has been chosen to simulate the kinetics because it presents the smallest solubility limit. This

choice is dictated by the wish to be as close as possible to a real Mg-RE system, where we observe quite low solubilities. It is worth to mention here, that the use of the third shell effective interaction breaks the topological similarity between *hcp* and *fcc* lattices, as the number of first and second nearest neighbors in this lattices are the same, whereas we have 2 atoms in the third shell of an *hcp* lattice and 24 in *fcc*.

5.2 AKMC parameters.

The kinetics Monte-Carlo method being based on the realistic temperature-activated vacancy diffusion mechanism needs in addition to the thermodynamic parameters (ω^i) also kinetic parameters. In our current study, we used kinetic parameters which had been estimated from the physical characteristics of the *hcp*-magnesium and neodymium metals so that in future to simulate the behavior of a binary Mg-Nd system. The description of those parameters is given below.

The energy of interaction of atoms of the same nature in the first shell: Interaction energy V^1_{XX} can be deduced from the cohesive energy of pure metals:

$$V^1_{XX} = \frac{2 \times E^{pur(X)}_{coh}}{Z_1},$$

where Z_1 is the number of atoms in the first shell. The cohesive energies are -1.51eV and -3.4 eV for Mg and Nd respectively [Kit87]. The parameters V^i_{XX} are considered equal to zero for $i > 1$.

The energy of interaction between atoms of different natures are given by the equation:

$$V^i_{XY} = \frac{V^i_{XX} + V^i_{YY} - \omega^i}{2},$$

where ω^i are the thermodynamic parameters used for the phase diagram simulation: $\omega^1 = 0.14$ eV, $\omega^2 = -0.07$ eV, $\omega^3 = -0.03$ eV.

The interaction energy between the vacancy and atoms. These "ghost" energies enable to describe the strain interaction of an atom with a vacancy defect in its neighborhood. They can be deduced from values of the vacancy formation energies of pure metals by means of the

equation:

$$E^X_{f(V)} = Z_1 V_{XV} - \frac{Z_1}{2} V^1_{XX}.$$

This information is available for Mg [Kri00]: $E^{Mg}_{f(V)} = 0.85$ eV. The latter gives the value of the effective atom-vacancy interaction parameter, V_{MgV}, equal to -0.057 eV, which is quite small.

For Nd, the data is not available. However, according to Athénes et al. [Ath96] the values of V_{XV} should not change the path performed by the vacancy, but only the time spent at each configuration. That's why in this study we set both V_{MgV} and V_{NdV} equal to zero.

The saddle-point energies. The binding energies at the saddle-point position can be deduced from migration energies of X in A as follows:

$$E^A_{mig(X)} = e^X_{sp} - (Z_1 - 1)V^1_{XA} - (Z_1 - 1)V^1_{AV} - V^1_{XV} - \sum_{i>1} Z_i V^i_{XA}, \tag{5.2.1}$$

The migration energy for Mg is known and equal to $E^{Mg}_{mig(Mg)} = 0.45$ eV [Kri00]. The value of migration energy of Nd is not available from experiments. In futher simulations, it will be set equal to the value of magnesium $E^{Mg}_{mig(Nd)} = 0.45$ eV.

The attempt frequency: This value can be estimated from the pre-exponential factor of the diffusion coefficient of X in A as follows:

$$\nu_X = \frac{D^A_{0(X)}}{a_0^2}, \tag{5.2.2}$$

where a_0 is the lattice parameter. This formula, however, is used in cubic lattices, where only one lattice parameter exists. The *hcp* lattice is described with two lattice parameters: a_0 and c_0, so in general we are obliged to use a matrix of diffusion coefficient and, hence, a matrix of pre-exponential factor.

In a Cartesian system with z-axis parallel to the 6-fold symmetry axis of *hcp*-crystall, the diffusion matrix becomes diagonal:

$$\hat{D} = \begin{pmatrix} D_\perp & 0 & 0 \\ 0 & D_\perp & 0 \\ 0 & 0 & D_\parallel \end{pmatrix}$$

where values $D_\perp$ and $D_{||}$ give diffusion coefficients in basal planes and between them respectively. In all others directions diffusion coefficient can be found from equation:

$$D(\theta) = D_{||}\cos^2(\theta) + D_\perp \sin^2(\theta), \tag{5.2.3}$$

where θ is the angle between the 6-fold symmetry axis and the direction of diffusion. For inter-plane first neighbors in *hcp* lattice one has:

$$\cos(\theta_{1o}) = \frac{1}{2\sqrt{\frac{1}{4} + \frac{1}{3}\frac{a_0^2}{c_0^2}}}.$$

In our study, vacancy jumps are allowed towards the first nearest neighbors of the *hcp* lattice, i.e. towards the in-plane ones as well as towards the inter-plane ones. As it was mentioned in previous section, the distance between in-plane and inter-plane neighbors are equivalent in *hcp*-magnesium, and equal to the lattice parameter a_0. By-turn, from [Meh90], the coefficients are equal to: $D_\perp = 1.5 \times 10^{-4}\ m^2/s$, $D_{||} = 1.0 \times 10^{-4}\ m^2/s$, which gives according to Eq. 5.2.3, $D(\theta_{1o}) \approx D_\perp = 1.4 \times 10^{-4}\ m^2/s$ for the inter-plane jump. Thus, in case of magnesium, we can use only one value of attempt frequency, calculated from the slightly modified equation Eq. 5.2.2:

$$\nu_X = \frac{D^A_{0(X)}}{a_0^{hcp\,2}},$$

where $D^A_{0(X)} = D_\perp$.

Because of the lack of experimental data, the attempt frequency of Nd is supposed to be the same as for Mg.

From the explanations given above, it is seen that not so much information is available to simulate a binary Mg-Nd system. Almost all the parameters of neodymium are not accessible for the moment. Moreover, the experimental results have demonstrated (see Section 3.2), that in this binary system the strain-induced interactions and effects linked are of major importance. As kinetic MC method is not able at present to take into account these elastic effects, we simulate by means of AKMC method an A-B binary system on the *hcp* lattice, where A would be as close as possible by its kinetic and thermodynamic properties to magnesium and B — a "variable" element of the alloy.

5.3 The activation energy of vacancy jump.

In the Section 4.5.1, the activation energy of vacancy jump has been given by the Eq. 4.5.2. In the cohesive model used, this expression can be rewritten using some mathematical transformations and represented in a slightly different explicit form:

$$E_{VX}^{act} = \begin{cases} \breve{E}_{mig(A)}^{A} - \frac{1}{2}u_V m_B^1 + \frac{1}{2}un_B^1 + \frac{1}{2}\sum_i \omega^i n_B^i & \text{if } X = A \\ \breve{E}_{mig(B)}^{A} - \frac{1}{2}u_V m_B^1 - \frac{1}{2}un_B^1 - \frac{1}{2}\sum_i \omega^i n_B^i & \text{if } X = B \end{cases}, \tag{5.3.1}$$

where $\breve{E}_{mig(A)}^{A} = E_{mig(A)}^{A} + V_{AV}$ and $\breve{E}_{mig(B)}^{A} = E_{mig(B)}^{A} - V_{AV} + 2V_{BV}$ are the configuration independent parameters, which can be considered as modified migration energies; $u_V = V_{BV} - V_{AV}$ is the atom-vacancy asymmetry interaction factor; $u = V_{BB}^1 - V_{AA}^1$ is the atom-atom asymmetry interaction factor; m_B^1 is the number of B atoms in the 1^{st}-shell of the vacancy V and n_B^i is the number of B atoms in the i^{th}-shell of the atom X exchanged with the vacancy V.

For sake of simplicity, the Eqs. 5.3.1 can be simplified. As it is explained in the previous section, we consider the case where $E_{mig(A)}^{A} = E_{mig(B)}^{A} = E_{mig}$ and $V_{BV} = V_{AV} = 0$. These assumptions lead to the following simplified version of the Eqs. 5.3.1:

$$E_{VX}^{act} = \begin{cases} E_{mig} + \frac{1}{2}un_B^1 - \frac{1}{2}\sum_i \omega^i n_B^i & \text{if } X = A \\ E_{mig} - \frac{1}{2}un_B^1 - \frac{1}{2}\sum_i \omega^i n_B^i & \text{if } X = B \end{cases}. \tag{5.3.2}$$

Eqs. 5.3.2 are equivalent to those used by Athènes et al. [Ath96] in their atomistic Monte-Carlo simulations of precipitation and B2 ordering in a binary alloy on a *bcc* lattice performed using a vacancy mechanism. The authors carried out simulation in supersaturated systems with a wide range of solute concentrations: $c_B = 10 - 40\%$. By means of the analysis of concentration and order fields, they found that for a composition close to the A2 (disordered *bcc* phase) solubility limit, precipitation and ordering proceed simultaneously and lead to a subsequent formation and growth of ordered B2 precipitates. At higher concentrations, a rapid short-range ordering of the whole volume was observed before any significant modification of the composition field. This regime was termed by authors as congruent ordering. At late stages of precipitation, for all concentrations, the rate of growth of the mean precipitate size was consistent with the classical Lifshitz-Slyozov-Wagner (LSW) [Lif61, Wag61] theory.

In addition, for a given alloy thermodynamics, the influence of atom-vacancy mobility (controlled by the asymmetry energy, u) has been studied. The authors showed that, for long aging times, consequence of variation of u is mainly accounted for by a simple change in the time scale. However, for the very early stages of alloy ordering, changing the asymmetrical energy induced a change of the kinetic pathway. Depending on the relative exchange frequency of the vacancy with A and B atoms (defined by u), and depending on the composition, two extreme regimes of ordering were identified, leading either to localized or delocalized ordering.

More recently, the influence of the asymmetry parameter, u, in the case of binary alloys undergoing decomposition has been investigated by several authors [Ath96, Ath00, Soi00, Rou01, Bou02]. It has been shown, that the precipitation kinetics may be considerably affected by changing the u-value, due to the change in single solute atom and small cluster mobilities, both during the nucleation stage [Ath00, Soi00] and during the coarsening stage [Ath00, Bou02]. These effects have been further studied in details and rationalized by Roussel and Bellon [Rou01]. Their results and conclusions will be analyzed and discussed later in the context of our results.

Most of the Monte-Carlo studies of the phase transformation kinetics in alloys were performed on cubic lattices: *sc*, *bcc*, *fcc*. To our knowledge, no works studying phase separation kinetics and ordering in *hcp* lattice have been undertaken. In the present work, in the framework of the atomistic kinetic Monte-Carlo simulation method, we study the precipitation kinetics of a model binary alloy on the *hcp*-lattice undergoing A3→A3+$D0_{19}$ ordering reaction. We pay attention to the investigation of the influence of atom-vacancy mobilities on the kinetic pathways of the phase separation as Athènes et al. [Ath96] have done in *bcc* lattice in case of ordering and phase separation and as Bellon and Roussel [Rou01] in case of phase separation only in *fcc* lattice. Both the early and late stages of precipitation are considered.

5.4 Influence of the atomic asymmetry parameter on the kinetic pathways.

Kinetic Monte-Carlo simulations were performed at $T = 700K$ in a model A-5.5%B alloy (marked by the square in Figure 5.4.1). According to the simulated phase diagram presented in Figure 5.4.1 a volume fraction of $D0_{19}$ equal to ~ 0.13 is expected.

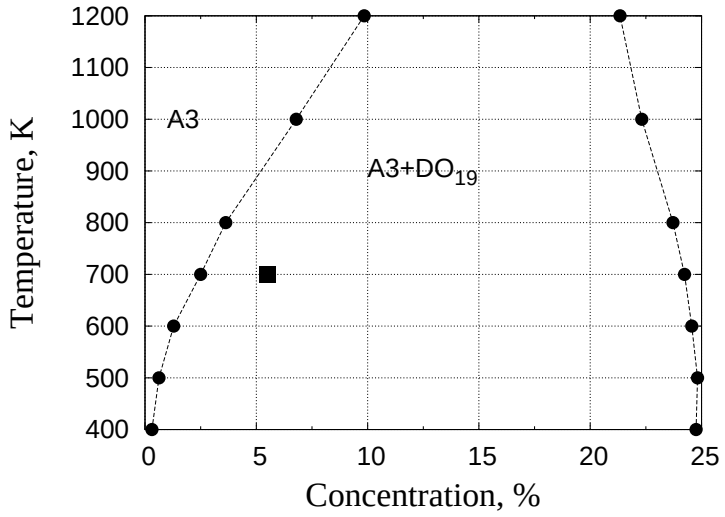

Figure 5.4.1: The simulated phase diagram (previously shown in Section 5.1) and the point corresponding to the present study by KMC method.

The standard size of the *hcp* box used for simulations in this work was equal to $80 \times 80 \times 40$ *hcp*-cells or 512000 atoms, unlike another is mentioned.

The thermodynamics of the system if fixed by the choice of ordering energies, ω^i, which give the phase diagram presented in Figure 5.4.1. As it was explained in the previous part, the migration energy, E_{mig} is also fixed(which is believed to result only in a shift of the time scale for a given temperature), whereas the atomic interaction asymmetry parameter, u, is allowed to vary.

Figure 5.4.2 presents successive positions of the vacancy for five different values of u in the alloy A-5.5%B which contains some $D0_{19}$ precipitates.

As clearly revealed by Figure 5.4.2, depending on the value of u, the vacancy resides preferentially in one of the two phases. For values of $u < \omega^1$ (Figure 5.4.2 a, b, c), the vacancy mainly resides inside the solute-depleted regions (i.e. in the matrix), whereas for $u \geqslant \omega^1$ (Figure 5.4.2 d, e) vacancy is mostly located inside the solute-enriched regions (i.e. in the precipitates). Also one has to note, that the trapping of vacancy on the interphase interfaces (the case observed in alloys decomposing into pure phases) has not been observed.

The preferencial vacancy location depending on the value of asymmetry parameter being clarified, let us now investigate the influence of this parameter on the overall kinetics.

All the results given in the following sections have been obtained for two asymmetrical energies $u = -0.2$ eV and $u = 0.2$ eV, representing the two extreme cases: preferencial location of vacancy inside the matrix ($u = -0.2$ eV) and inside precipitates ($u = 0.2$ eV). For all presented simulations,

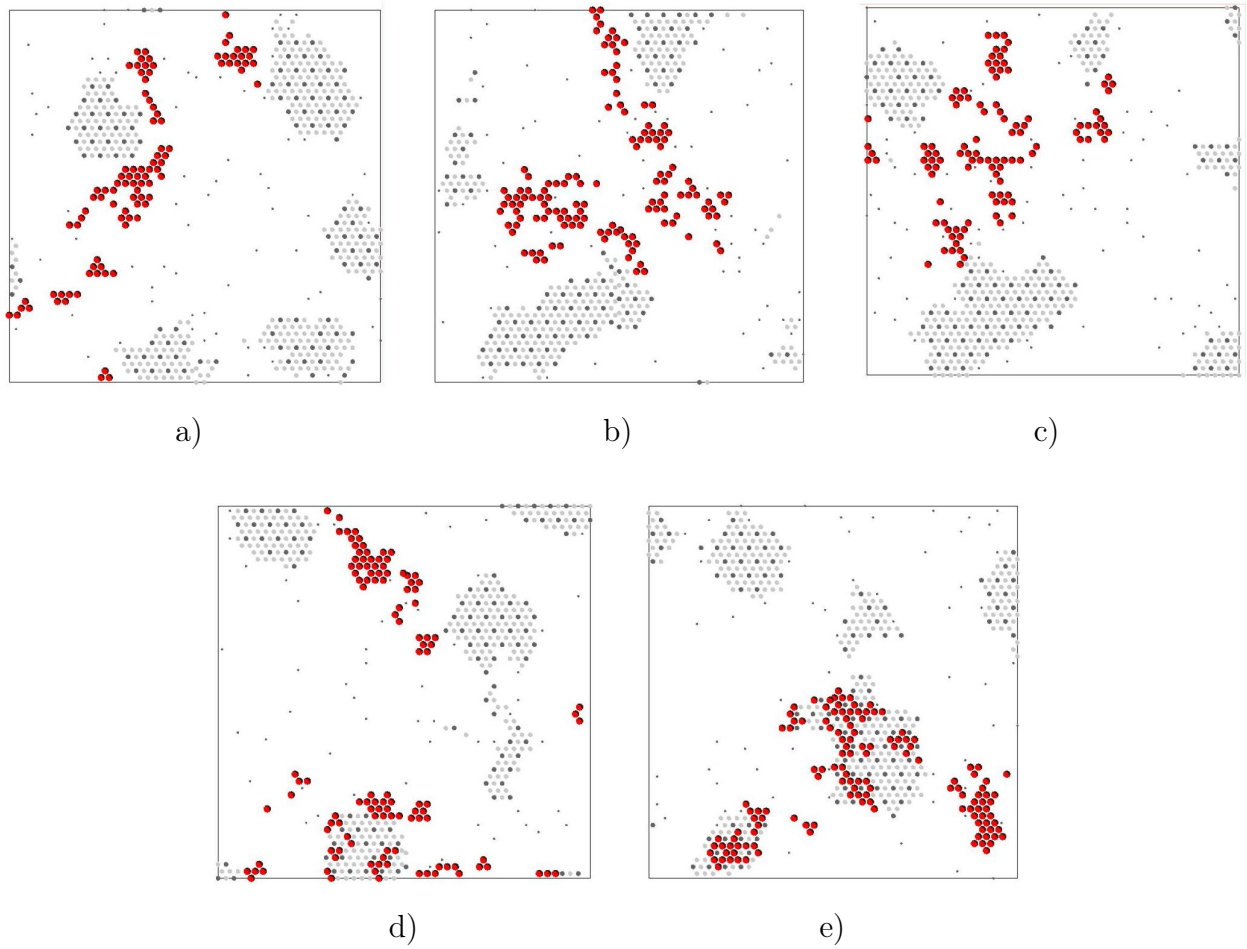

Figure 5.4.2: Two-dimensional visualizations of the vacancy location in an alloy with the composition $c_B = 5.5\%$ annealed for a long time and containing some ordered precipitates. Snapshots correspond to the value of asymmetric parameter u equal to a) -0.2eV ($< -\omega^1$), b) -0.14 eV ($= -\omega^1$), c) 0.0 eV, d) 0.14 eV ($= \omega^1$), e) 0.2 eV ($> \omega^1$). Vacancy positions are shown in red, A atoms in light-gray and B-atoms in dark-gray. A-atoms inside the matrix are not visualized for clarity.

the initial configuration was random.

5.4.1 Results.

The kinetics of decomposition and ordering for the simulated alloys was followed by means of 4 parameters: i)The SRO parameters up to the third neighbors, ii) the matrix concentration, iii) precipitate volume fraction and iv) the degree of long-range order. Some additional parameters as diffraction maps and small angle scattering intensities were also used to describe precisely the kinetics.

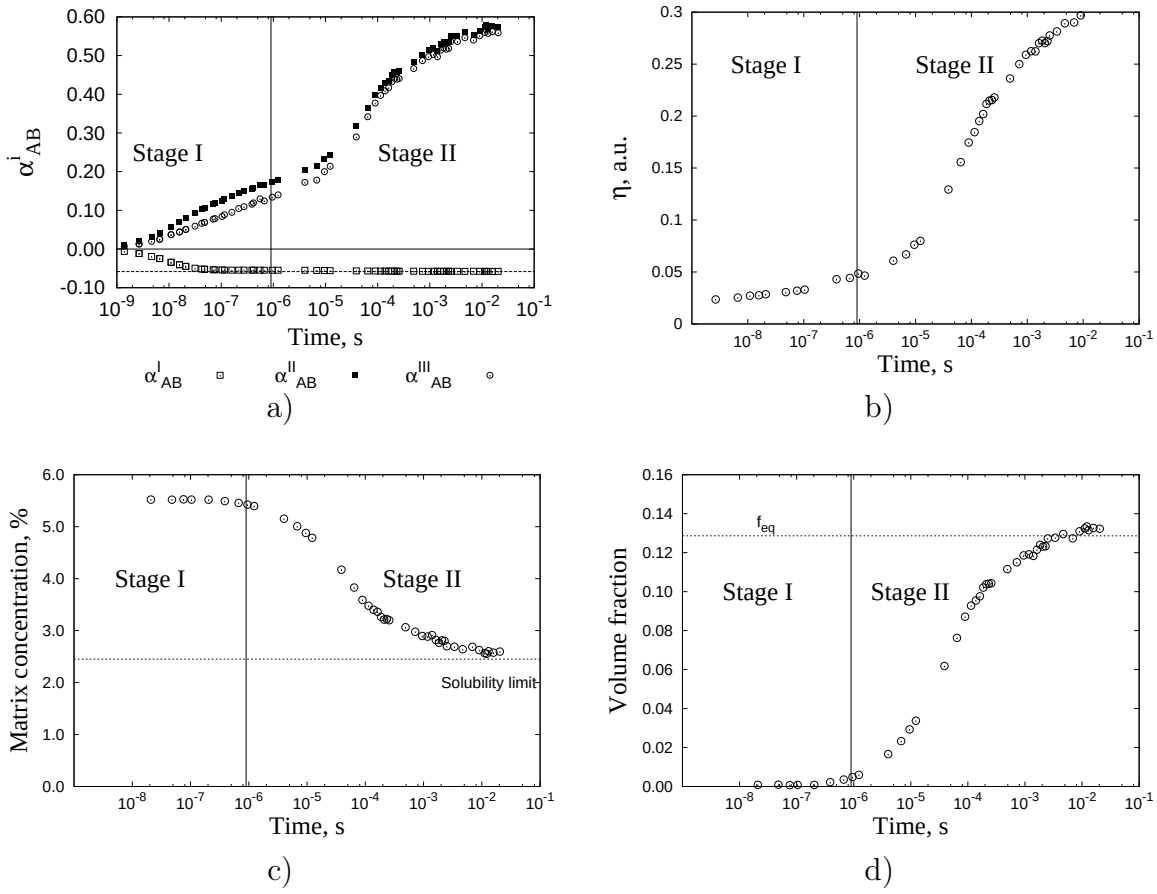

Figure 5.4.3: Evolution of a) three first Warren-Cowley parameters, b) degree of long-range order, c) matrix composition and d) precipitate volume fraction during phase transformation in the alloy with asymmetry parameter, u, equal to 0.2 eV.

Although the microstructure evolves in a continuous and progressive way, two distinct stages can be defined as qualitative guides. These stages do not correspond to any singular point in kinetics.

Kinetics for $u = 0.2$ eV ($u > \omega^1$).

Stage I: During this stage, the three first Warren-Cowley parameters (Figure 5.4.3a) increase and present signs characteristic of the $D0_{19}$ order ($\alpha^I_{AB} < 0$, $\alpha^{II}_{AB} > 0$, $\alpha^{III}_{AB} > 0$). $D0_{19}$ type of order develops in the system. The diffuse character of the intensity reinforcement of the diffraction pattern (Figure 5.4.4a, b) around the $\{0\ \frac{1}{2}\ 0\}$ superstructure positions of $D0_{19}$ structure shows that only short range order takes place. No small angle scattering in observed (Figure 5.4.4d), hence, no compositional changes occur. Matrix concentration does not evolve (Figure 5.4.3c), and consequently, the precipitate volume fraction stays equal to zero (Figure 5.4.3d).

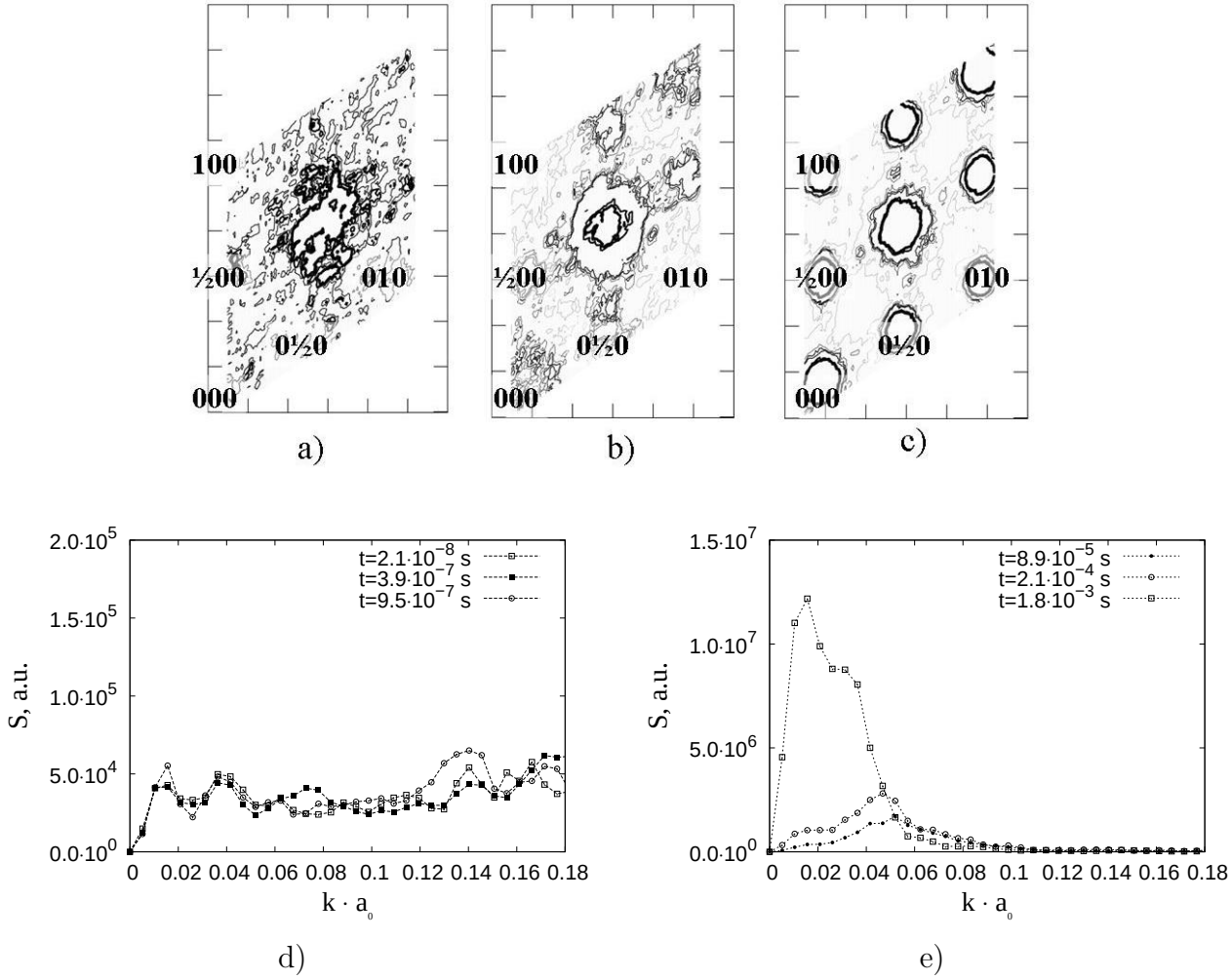

Figure 5.4.4: Diffraction maps obtained by Fourier transform of the atomic configuration a) at **Stage I**, b) close to the boundary between stages, c) at **Stage II**. The spherically averaged structure functions near (000) reciprocal point for atomic configurations d) at **Stage I** and e) at **Stage II**.

Stage II: Composition changes occur. Small angle scattering is observed, the peak height grows and shifts to the smaller $|\vec{k}|$ (Figure 5.4.4e). Some B-rich and ordered precipitates appear and develop, which gives raise to the increase of precipitate volume fraction and depletion in B of the matrix (Figure 5.4.3c, d). Diffraction pattern exhibits well defined intensity reinforcement associated to the development of long range order in the ordered $D0_{19}$ precipitates (Figure 5.4.3b and Figure 5.4.4c), which appear and develop. The superstructure intensity markedly increases (Figure 5.4.3b), signifying the development of long-range order.

Kinetics for $u = -0.2$ eV ($u < -\omega^1$).

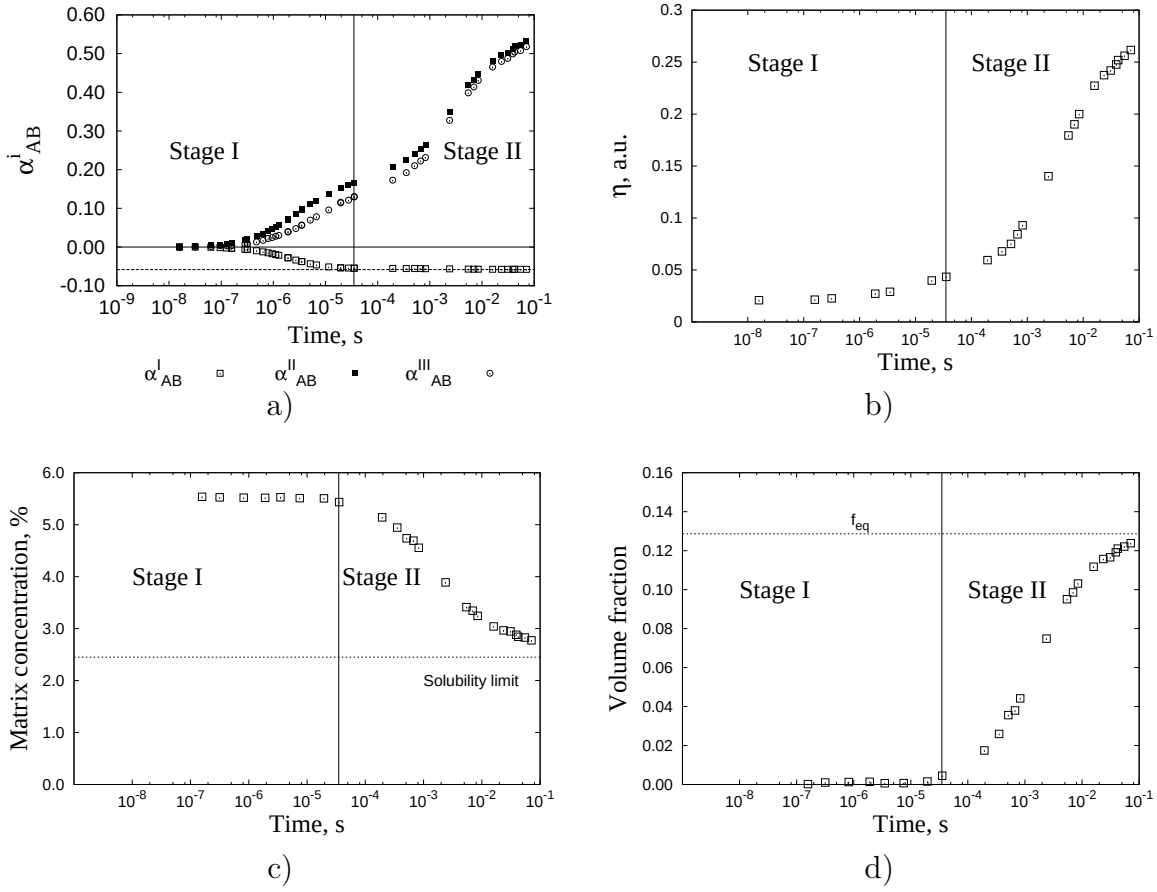

Figure 5.4.5: Evolution of a) three first Warren-Cowley parameters, b) degree of order, c) matrix composition and d) precipitate volume fraction during phase transformation in the alloy with asymmetry parameter, u, equal to -0.2 eV.

Unlike a time-scale shift, the same stages are observed in the case of the asymmetric parameter equal to $u = -0.2$ eV as shown by: the evolution of Warren-Cowley parameters (Figure 5.4.5a), the matrix composition (Figure 5.4.5b), the precipitate volume fraction (Figure 5.4.5c) and the degree of order (Figure 5.4.5d).

Nevertheless, regarding the evolution of the Warren-Cowley parameters, one can notice a minor distinction in stage I: the α^I_{AB}-parameter saturates at the transition point to the stage II, i.e. when the composition heterogeneities appear, whereas for the previous case the first Warren-Cowley parameter reaches the limit value far before the decomposition becomes evident (Figure 5.4.3a).

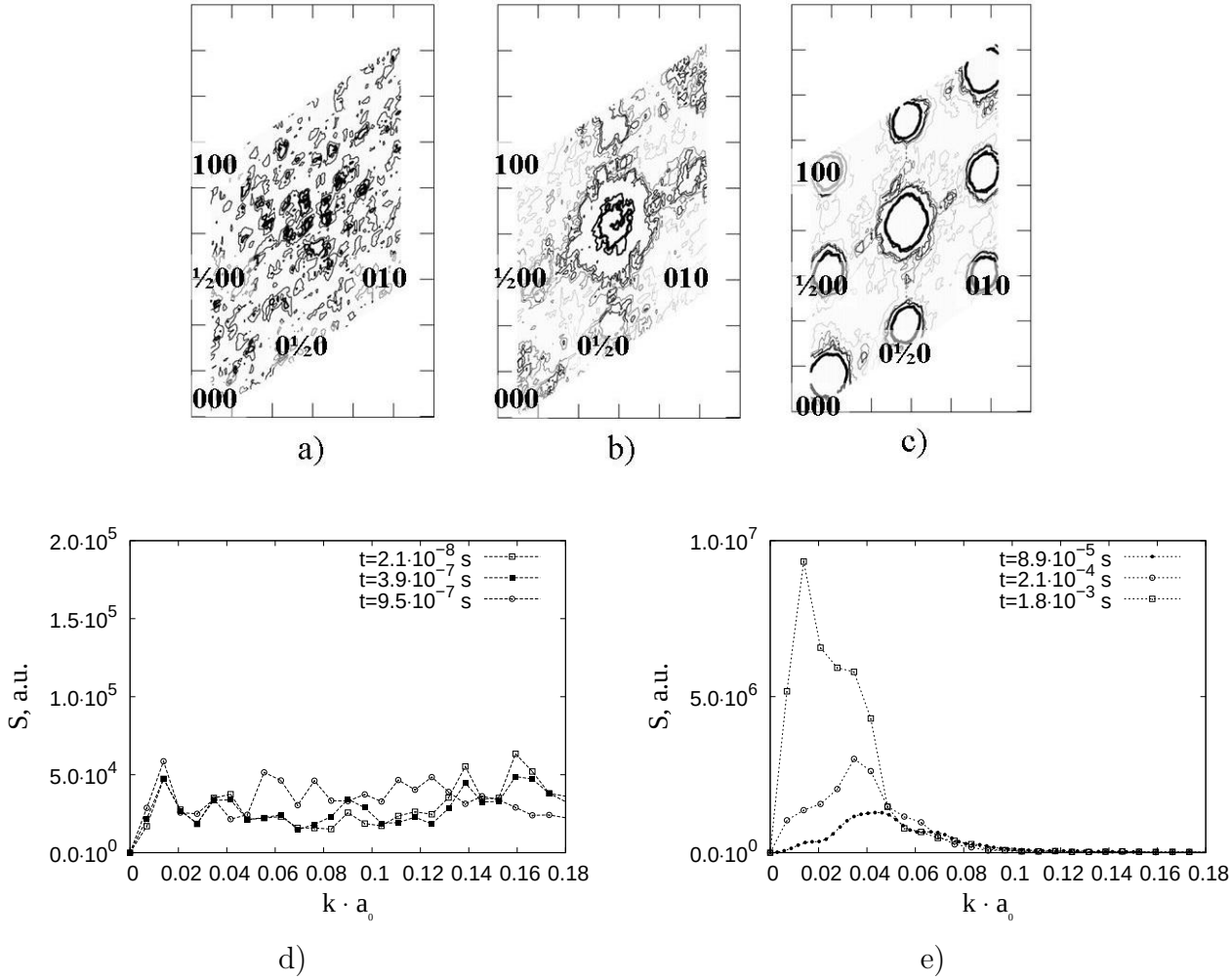

Figure 5.4.6: Diffraction maps obtained by Fourier transform of the atomic configuration a) at **Stage I**, b) close to the boundary between stages, c) at **Stage II**. The spherically averaged structure functions near (000) reciprocal point for atomic configurations d) at **Stage I** and e) at **Stage II**.

Significant modifications of the evolution of matrix composition or precipitate volume fraction have not been revealed in comparison with the value $u = 0.2$ eV. For both alloys the precipitates formed during the phase separation have the stoichiometric composition ($c_B^{prec} = 25\%$) during the phase separation.

5.4.2 Discussion.

Distinction in the evolution of the first short-range order parameter, α_{AB}^I, for two alloys ($u > 0$ and $u < 0$) comes not only from the trivial time-scale shift or from the ambiguity in the choice of the boundary between the two stages, but has rather a kinetic origin. This is confirmed by the graphs given in Figure 5.4.7, where α_{AB}^I and α_{AB}^{III} are plotted as functions of α_{AB}^{II} for the two

asymmetry parameters (time is eliminated).

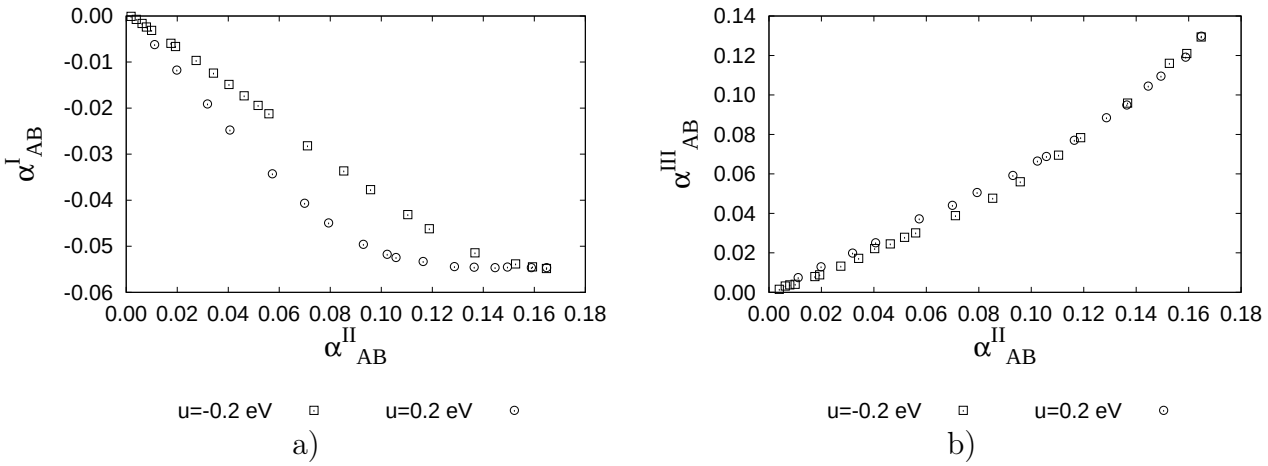

Figure 5.4.7: The evolution of a) α_{AB}^{II} and b) α_{AB}^{III} as a function of α_{AB}^{I} as presented for two asymmetrical energies.

One can see, that curves in Figure 5.4.7a are not superimposed, whereas superimposition of curves in Figure 5.4.7b is almost complete. This proves the nonequivalence between the evolution of α_{AB}^{I} in the two cases. In case of negative u, the short-range order in the first atomic shell develops slower than in the case of positive asymmetry parameter.

The differences in the short-range ordering found at **Stage I** of the precipitation kinetics in the two systems do not affect, however, the further ordering and decomposition behavior. For the studied intervals of time, the consequences of varying u are mainly accounted for by a simple change in time scale. It is easy demonstrated by eliminating the time between two independent characteristics of system, for example, between the matrix concentration and the long-range order parameter.

Figure 5.4.8 shows that for the two asymmetry parameters, plotted dependencies are superimposed onto a single curve. Moreover, conventional Kawasaki dynamics (see Section 4.4) simulations were performed in a system with the same number of atoms ($N = 512\,000$), the same atomic composition ($c_B = 5.5\%$) and thermodynamics (the same set of ordering energies, ω^i). Obtained kinetics show the same matrix composition-order parameter dependence (Figure 5.4.8, black squares). The curve is perfectly superimposed to the curves obtained by AKMC method. No effect of vacancy have been revealed.

Let us now check the influence of asymmetry parameter variation of the morphology of $D0_{19}$

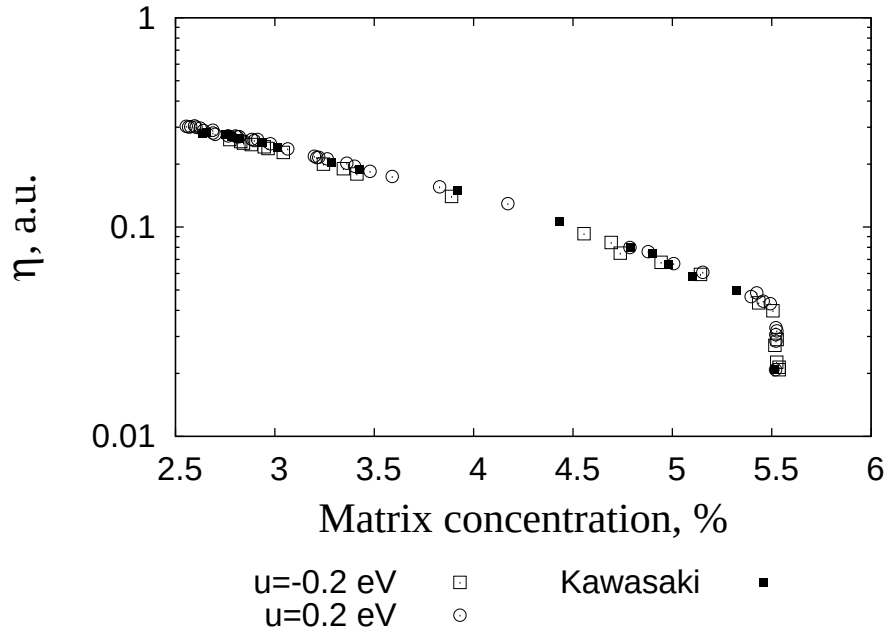

Figure 5.4.8: Time evolution of degree of order vs matrix composition for systems with the two different asymmetrical energies as obtained by AKMC simulations. Black squares correspond to the Kawasaki MC simulations performed in a system of the same composition, number of atoms and thermodynamics.

precipitates. Careful observation of the microstructures (Figure 5.4.9) confirms that at a given value of the matrix concentration (or precipitate volume fraction) obtained for different u values no qualitative differences can be found in the morphologies.

As we explained in part 5.3, influence of the u parameter on coarsening mechanisms has been intensively studied by Monte-Carlo methods in binary alloys undergoing a phase separation [Ath00, Rou01, Bou02]. Two mechanisms have been reported: the mechanism of evaporation-condensation of individual atoms and mechanism of diffusion and coagulation of atomic clusters.

Athènes et al. [Ath00] have shown that the asymmetry parameter, u, has a strong influence on the mobility of small solute atom clusters and, at a given annealing temperature, the change of sign of this parameter leads either to the diffusion-coagulation or to the evaporation-condensation mechanism. The work of Roussel and Bellon [Rou01] confirmed directly the results of Athènes et al. [Ath00]: when the vacancy mostly resides in the matrix a condensation-evaporation mechanism of individual atoms is observed. When the vacancy mostly diffuses inside precipitates ($u > 0$), the diffusion-coagulation mechanism of coarsening is expected.

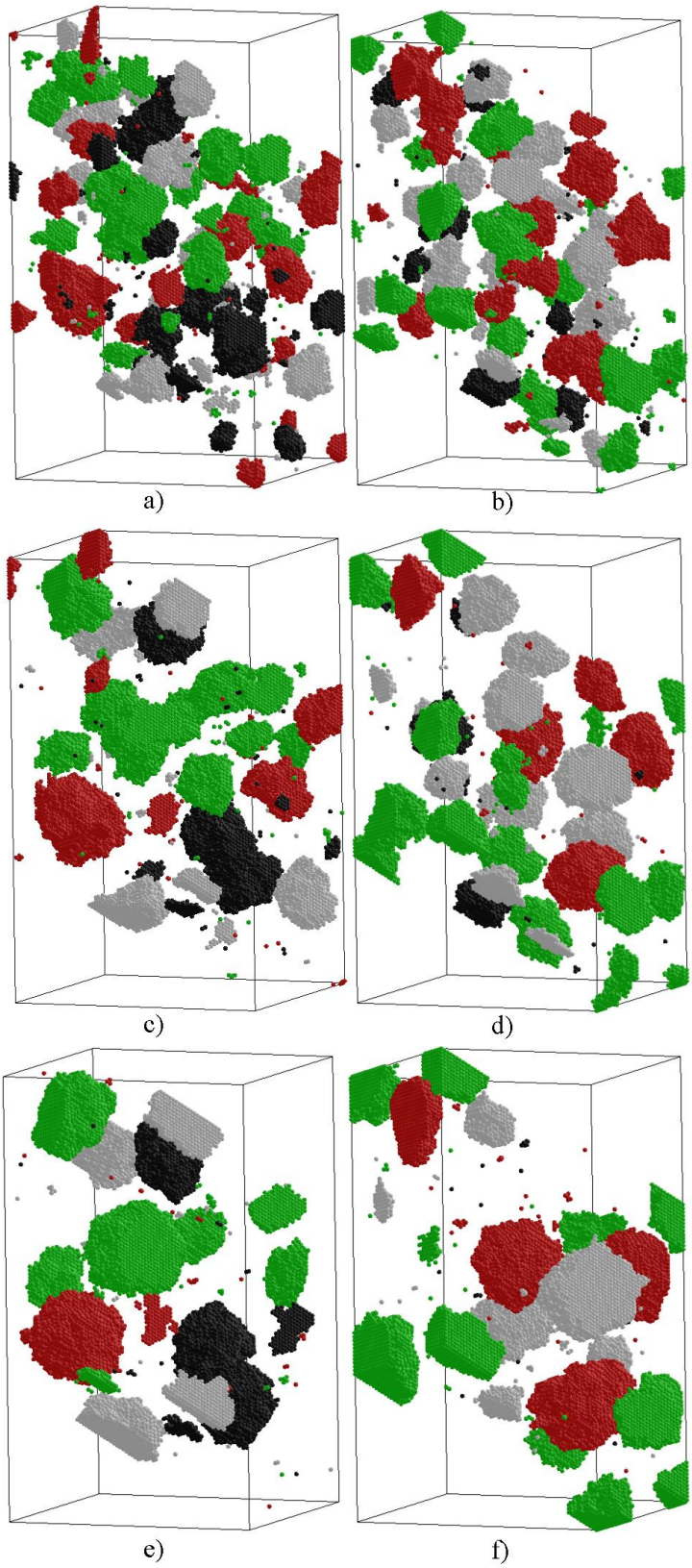

Figure 5.4.9: The multivariant precipitate microstructure for matrix composition $c_B = 3.3\%$ (a, b), $c_B = 3.0\%$ (d, c) and $c_B = 2.8\%$ (e, f) and for two asymmetrical energies (a, c, e)$u = 0.2$ eV and (b, d, f) $u = -0.2$ eV. Every point here correspond to one atom, for which the local degree of order as defined by Eq. 4.6.9 is major than 0.9. Atoms visualized in different colours correspond to different translation variants of $D0_{19}$.

In order to check if such kind of phenomena are observed in case of ordered precipitates, we, follow Roussel and Bellon [Rou01] and use the graphical method that is illustrated in Figure 5.4.10.

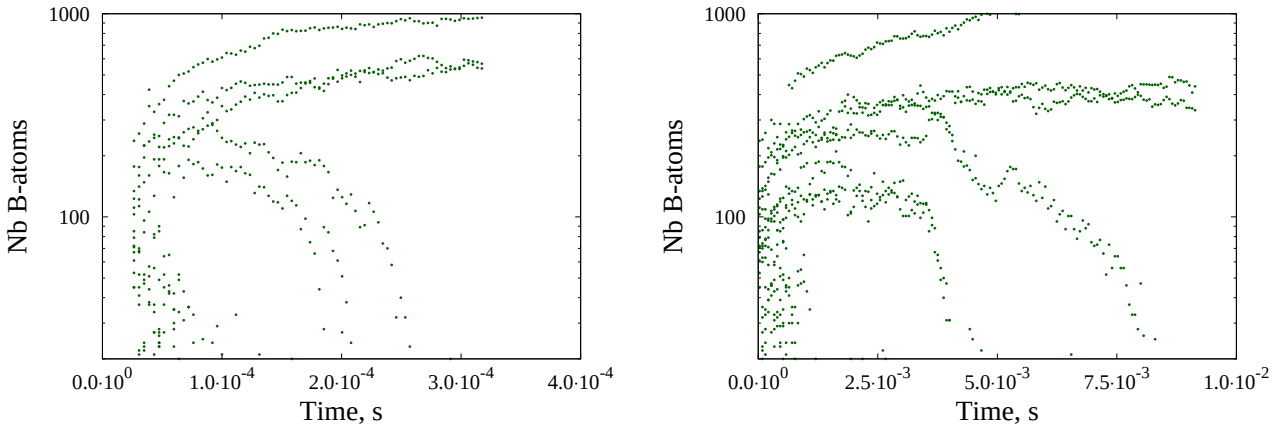

Figure 5.4.10: Illustration at late stages of the *fountainlike* evolution obtained by plotting Monte-Carlo time variations of all cluster sizes for a) $u = 0.2$ eV and b) $u = -0.2$ eV. Simulation box contains $2 \cdot 40 \times 40 \times 20$ *hcp* sites, concentration of solute atoms is $c_B = 5.5\%$. During the shown period of phase transformation the matrix concentration changed from 4.4 to 3.0%

It consists in reporting on a same graph the size evolution of all precipitates (in terms of number of B-atoms). If the coagulation-diffusion mechanism occurs, steps must be observed (these steps correspond to the coagulation of two precipitates). If the evaporation-condensation mechanism is observed, the size of precipitates varies by only one atom. This gives a so-called *fountainlike* evolution.

From Figure 5.4.10 one can distinguish a *fountainlike* evolution for both values of asymmetry parameter. The fountainlike behavior demonstrates the presence of a coarsening regime occurring by evaporation and condensation of solute atoms from small to larger ones (Ostwald ripening). This shows that even for $u > 0$, a condensation-evaporation mechanism is observed. There is no diffusion-coagulation mechanism for these ordered precipitates. This is not surprising. Indeed, diffusion of ordered precipitates should involve a local destruction of order which is clearly no energetically favorable.

In good agreement with these results, Figure 5.4.11a and b show that the Lifshitz-Slyozov-Wagner law [Lif61, Wag61]

$$R^3(t) = R_0^3 + B_{LSW}t, \tag{5.4.1}$$

based on evaporation-condensation mechanism, fits well the time evolution of the cube of the

precipitate size for both $u = 0.2$ eV and $u = -0.2$ eV.

Recently, Huse [Hus86] proposed another description of the mean precipitate size growth for high volume fraction taking into account the contribution of diffusion along the interfaces between phase domains. He obtained the following phenomenological growth law:

$$R(t) = A + B_H t^{1/3}, \tag{5.4.2}$$

where B_H corresponds to the contribution of the diffusion through the bulk whereas A is a constant which includes both the diffusion along the interface and through the bulk. At very late aging time, when A becomes negligible the same asymptotic behavior as the LSW one, $R \sim t^{1/3}$, is observed.

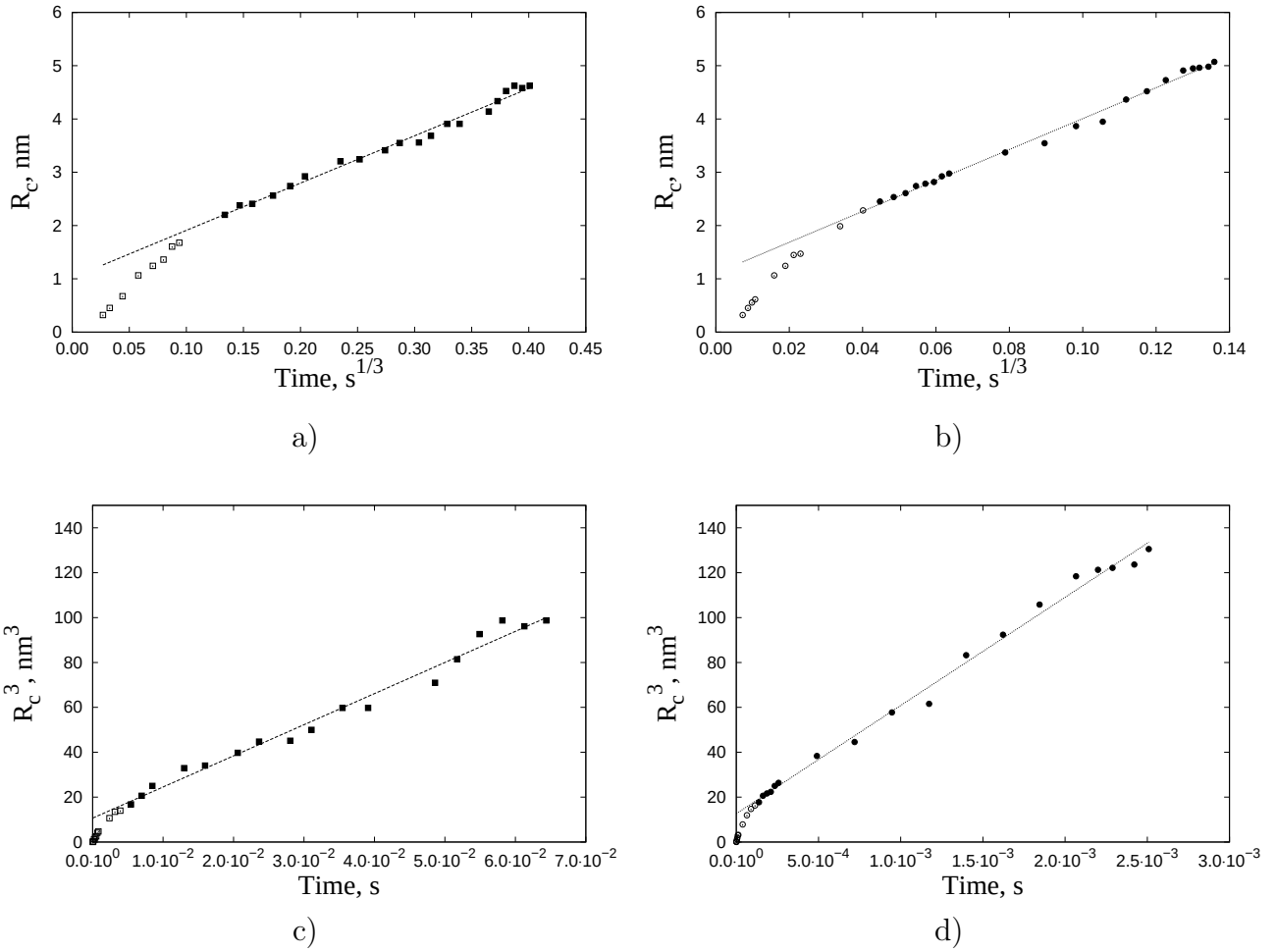

Figure 5.4.11: Evolution of R_c as function of $t^{1/3}$ for alloy with a) $u = 0.2$ eV and b)$u = -0.2$ eV. Evolution of R_c^3 as function of t for alloy with c) $u = 0.2$ eV and d)$u = -0.2$ eV. For every value of u, R_c is averaged over 3 idependent runs.

In Figure 5.4.11, $R_c = f(t^{1/3})$ (Figures 5.4.11a and b) is presented for the different asymmetry parameters. After the early stages of aging, a linear behavior of R_c vs $t^{1/3}$ is observed in both cases. Moreover, comparison of Figures 5.4.11a to b and c to d, shows that the R_c evolution starts to obey the Huse's (Eq. 5.4.1) and LSW law (Eq. 5.4.2) at the same time. The values of coefficients obtained by the fits are presented in Table 5.4.1.

Alloy	R_0, nm	B_{LSW}, nm/s^3	A, nm	B_H, nm/s$^{1/3}$	B'_H,nm/s$^{1/3}$
$u = 0.2$ eV	2.35 ± 0.04	41861 ± 809	1.16 ± 0.04	27.2 ± 0.7	34.7 ± 0.67
$u = -0.2$ eV	2.42 ± 0.05	1398 ± 20	1.12 ± 0.04	8.7 ± 0.1	11.18 ± 0.16

Table 5.4.1: Fit coefficients.

The values of B'_H deduced from the corresponding values of B_{LSW} using the simple relationship: $B'_H = B_{LSW}^{1/3}$ are close to those B_H obtained by the fit of the data. It means, in very good agreement with our previous observations, that the interfacial diffusion is negligibly small or absent in the two investigated systems at the late stages of precipitation.

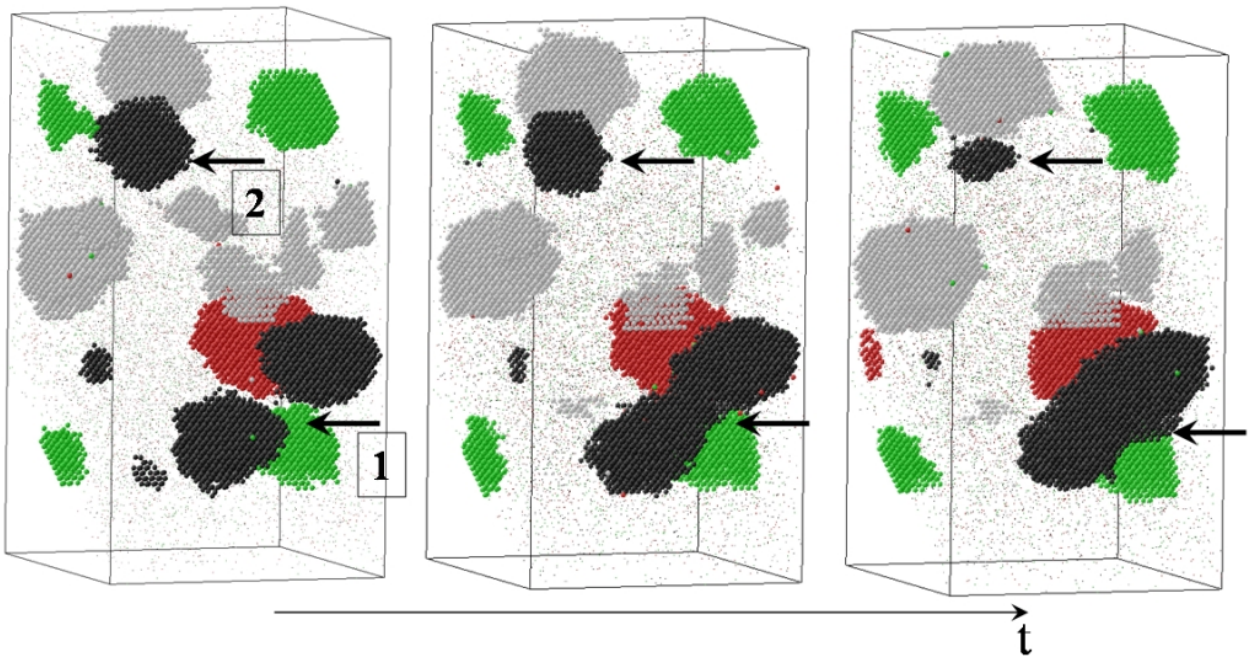

Figure 5.4.12: 3d atomic maps visualizing the multivariant microstructure of the alloy containing ordered precipitates with different ordering variants. The arrow **1** points the two precipitates which coagulate, the arrow **2** points a precipitate which gradually dissolutes during the coarsening.

We should mention that rare accidents of big precipitates coagulation happen, like it was found in the alloy with asymmetry parameter $u = 0.2$ eV (Figure 5.4.12, the arrow **1**). The presented case, strictly saying, does not demonstrate a mechanism of coarsening in the definitions which were given above. The coagulation of the two clusters happened not due to their relative movement,

but due to their intersection caused by growth. By-turn, their growth was governed (according to our analysis) by condensation of atoms, evaporated from surrounding precipitates which gradually shrink (like one shown in Figure 5.4.12 and marked by the arrow **2**).

This kind of coagulation events are rare due to the multivariant nature of precipitates in the ordered alloy. The evolution of alloy microstructure (described in terms of mean precipitate size, matrix concentration, precipitate volume fraction and degree of order) is not affected by them, as it has been demonstrated above.

5.4.3 Conclusions.

AKMC technique has been used to study in detail both the early and late stages during precipitation of a $D0_{19}$ ordered phase from a disordered supersaturated *hcp*-phase. The precipitation processes have been analyzed mainly in terms of the evolution of SRO parameters, matrix concentration, precipitate volume fraction, mean precipitate size and degree of long-range order. Some additional observations (diffraction maps, structure peak intensities intensities and direct observation microstructure) were also involved into analysis. The influence of the asymmetry parameter u on the kinetics of the phase separation in diluted alloys has been studied.

It was shown, that regardless of the value of asymmetry parameter

- The early stages of the phase transformation are characterized by the rapid development of short range order.
- Long-range order develops whereas composition field evolves.
- Once the matrix becomes depleted in solute atoms, evolution of the precipitate size obeys the classical LSW law. The growth of precipitates proceeds by the evaporation-condensation mechanism of individual atoms. The effect of surface diffusion is negligibly small or absent. No coagulation-diffusion mechanism is observed.
- No vacancy effect has been reported. Same results have been obtained by Kawasaki dynamics. The microstructure of the alloy evolves similarly with and without vacancy. This validates the use of such a diffusion mechanism to simulate phase transformation in simulation model which takes also into account elastic effects. Indeed, up to now, it is not possible to consider both, the vacancy diffusion mechanism and elastic effects.

It is worth noting, however, that (in addition to trivial time-scale shift) changing the asymmetrical energy induces a slight change of kinetic path for the early stages of alloy ordering: it was shown that the short-range ordering in the first shell is slowed down in the case of negative asymmetry parameter, in comparison to one for positive parameter. Nevertheless, the latter does not affect further kinetic pathway.

References

Ath96. M. Athènes, P. Bellon, G. Martin, F. Haider, *Acta Materialia*, **44**(12):4739 (1996).

Ath00. M. Athènes, P. Bellon, G. Martin, *Acta Materialia*, **48**(10):2675 (2000).

Bic92. C. Bichara, S. Crusius, G. Inden, *Physica B: Condensed Matter*, **179**(3):221 (1992).

Bin81. K. Binder, J. L. Lebowitz, M. K. Phani, M. H. Kalos, *Acta Metallurgica*, **29**(9):1655 (1981).

Bou02. Y. L. Bouar, F. Soisson, *Phys. Rev. B*, **65**(9):094103 (2002).

Hus86. D. A. Huse, *Phys. Rev. B*, **34**(11):7845 (1986).

Kit87. C. Kittel, *Introduction to Solid State Physics*, Wiley, New York, 1987, 6th ed. edition.

Kri00. H. Krimmel, M. Fähnle, *Phys. Rev. B*, **62**(9):5489 (2000).

Lif61. I. Lifshitz, V. Slyozov, *Journal of Physics and Chemistry of Solids*, **19**(1-2):35 (1961).

Meh90. H. Mehrer, N. Stolica, N. A. Stolwijk, *Diffusion in Solid Metals and Alloys, Landolt-Bυrnstein.*, volume 26, Springer-Verlag, Berlin, 1990.

Rou01. J.-M. Roussel, P. Bellon, *Phys. Rev. B*, **63**(18):184114 (2001).

Shi00. M. Shimono, H. Onodera, *Phys. Rev. B*, **61**(21):14271 (2000).

Soi00. F. Soisson, G. Martin, *Phys. Rev. B*, **62**(1):203 (2000).

Wag61. C. Wagner, *Z. Electrochem.*, **65**:581 (1961).

Conclusions and perspectives

The goal of the present work was to study the kinetics of the early stages of phase transformations in the model binary Mg-Nd and ternary Mg-Y-Nd alloys. From previous studies it was known that the kinetics includes the processes of ordering and decomposition. The tomographic atom probe had been used as the main experimental technique for the investigations of secondary phase precipitation in these alloys. This instrument (APT) of analysis offered the possibility to study the materials at the atomic scale, in the real space and in three dimensions. High analytical sensivity and spacial resolution provided the opportunity to study compositional evolution of precipitating phases and to obtain some crystallographic information on those phases.

Having the goal to follow the kinetics of phase transformation in the binary Mg-Nd alloy, we first performed a study of thermodynamics of the system. In the framework of the present investigation, the Mg-rich part of the Mg-Nd phase diagram has been clarified. The high temperature solid solubility limit of Nd in Mg has been assessed experimentally by means of atom probe tomography. The presented results aim at the correction of the disposal binary Mg-Nd diagram and might help for the extraction of thermodynamic quantities of the system.

Then, the study of the nanostructural and compositional evolution of Mg-Nd alloy has been carried out during phase separation at 150°C for aging times ranging from 54 h to 1324 h. The APT technique revealed that the precipitation in the investigated alloy starts by the formation of thin precipitates associated with (ordered) GP zones. By-turn, the GP zones continuously grow and evolve into the coherent β'' precipitates reported to appear in this system. These precipitates are plates laying on the $\{10\bar{1}0\}$ planes and are elongated along the [0001] direction of the host *hcp*-lattice. The results of atom probe study of late stages of microstructure evolution have been confronted to the TEM results. The multi-fragmented structure of precipitates has been revealed by TEM observations. The low solute content in precipitates (as compared to the stoichiometry of the fully ordered $D0_{19}$ phase) as investigated by APT, being confronted to the revealed complex structure, correlates well with the proposed earlier stepped APB-like $D0_{19}$ atomic structure. Monotonous growth of precipitates was observed during the studied times of aging. The growth mostly proceeded in two directions, whereas the thickening of precipitates was negligible or absent. At late stages, when precipitate sizes became relatively large, the shape of some precipitates was not longer plate-like: there were revealed precipitates consisting of several

plates turned one to each other on angle equal to 120°. The latter indicated that the precipitate growth direction might spontaneously change when the size of precipitate reached a big value.

In order to explain the apparent plate-like shape of coherent precipitates in the investigated alloy, a macroscopic continuous model considering elastic effects has been employed. It was shown in the framework of this model, that apparent shape of precipitates and crystallographic relationships between the matrix and precipitates might be analyzed if one supposes a difference between lattice parameters of the stress-free secondary phase and the matrix. The developed model allows to demonstrate at which conditions a certain family of habit planes appears. Relations between lattice parameters of constrained secondary phase inclusion and the lattice parameters of the matrix and inclusion's elastic modulus were calculated for some commonly observed habit planes.

A comparison of the nanostructural and compositional evolution of Mg-Y-Nd alloy during phase separation at 150°C for aging times ranging from 168 h to 1324 h was obtained employing the APT technique. It was shown that both Yttrium and Neodymium were involved into formation of atomic heterogeneities in the system. The particles formed at late aging times (after 864 h) revealed a plate-like shape. The additions of Yttrium atoms significantly slowed down the speed of the decomposition in the ternary alloy in comparison to the binary one. The pair-correlation analysis and direct observation of the alloy microstructure demonstrated that Yttrium also participated the precipitation but "weaker" than Neodymium.

Simulation of the kinetics of precipitation of $D0_{19}$ phase from *hcp* solid solution without strain energy has been undertaken by Monte-Carlo simulation. The latter is based on the fundamental diffusion mechanism most often observed in pure metals and alloys: the atomic diffusion by the vacancy mechanism.

These simulations were performed in a model binary system using some available physical parameters for a real Mg-based alloy. AKMC technique has been used to study the early and late stages of phase decomposition in diluted alloys. The pair-interaction model was employed and the influence of the asymmetry parameter $u = V^1_{BB} - V^1_{AA}$ on the kinetics of the phase separation has been studied. Regardless the value of asymmetry parameter, the early stages of the phase transformation are characterized by the rapid development of short-range order. Long-range ordering proceeds when the composition field evolves, i.e. simultaneously with decomposition. The growth of ordered precipitates is performed by the evaporation-condensation mechanism of

individual atoms. This leads to the classical LSW law in the evolution of the mean precipitate size. For comparison, the evolution of the system has been simulated by Kawasaki dynamics (direct exchanges between atoms). It was found that the microstructure of the alloy evolves similarly with and without vacancy. In addition to trivial time-scale shift, changing the asymmetrical energy induced a slight change of kinetic path for the early stages of alloy ordering: it was shown by eliminating the time scale, that the evolution of the short-range order parameters could not be superimposed in the systems with different u. Nevertheless, the latter does not affect further kinetic pathway.

———

Both binary and ternary systems are very interesting from the physical point of view. The substitutional alloys with hexagonal close-packed lattice (specific for pure magnesium and for its alloys) are not so much studied and described in the physical literature. Further deeper fundamental understanding of different processes occurred in these and similar systems at the meso- and micro-scales is needed. Further experimental investigation might include

- the Kinetics of X-ray (or thermal neutrons) diffuse scattering technique in order to study diffusion processes in such systems;
- the analytical high resolution TEM technique to confirm the atomic structure of the precipitates;
- the precise X-ray (or other sensitive) measurements in order to provide the information about lattice parameters of the formed (especially coherent) phases.

The small solubility of RE elements in magnesium and complex precipitation sequence of Mg-RE alloys make somewhat complicated the experimental estimation of physical parameters necessary for further simulations. That is why the relevant and precise ab-initio calculations of interactions, diffusion coefficients, lattice parameters and so on in such systems would be extremely useful.

Future theoretical studies and simulations should mandatory take into account the strain-induced effects appearing the the Mg-RE systems, which obviously play an significant role for phase transformation behavior and secondary phase morphology. As we have shown that no vacancy effect are observed, such simulations without vacancies could be undertaken and be physically acceptable.

A APT specimen preparation procedure.

To prepare the specimens for APT, blanks of approximately 300 μm×300 μm in cross section and 20 mm in length were cut. APT tips were prepared by a two-step electropolishing procedure: (i) rough polished in a solution of 25 pct perchloric acid in acetic acid at a voltage of 20 to 25 V at room temperature and (ii) fine polished using a solution of 2 pct perchloric acid in butoxyethanol at a voltage of 5 to 12 V DC. After fine polishing, specimens were immediately cleaned in ethanol (or isopropanol) and kept under vacuum until experiment is carried out.

B TEM specimen preparation procedure.

To prepare the specimens for TEM, alloy samples were sliced into approximately 300 μm thick strips. Discs of 3 mm diameter were punched out of the slices. Thin foils for TEM observations were prepared by twin jet electropolishing in a solution of 25% HNO_3 and 75% methanol cooled down to -35°C. Then, specimens were ion milled using the Precision Ion Polishing System (GATAN 691).

Conventional TEM observation were carried out using a JEOL 2000 FX operating at 200 kV.

C Crystallography of *hcp*-lattice.

The hexagonal close-packed lattice is a complex Ising lattice which can be considered as two interpenetrating hexagonal Bravais sublattices displaced with respect to each other by the vector $\rho = 2/3\vec{a}_1 + 1/3\vec{a}_2 + 1/2\vec{a}_3$, where $\vec{a}_1$, $\vec{a}_2$, $\vec{a}_3$ are the primitive-translation vectors of *hcp* lattice along the [100], [010], [001] directions, respectively, in the oblique (hexagonal) system of coordinates. The coordinates of the primitive-translation vectors (or basis vectors) in Cartesian coordinate system shown in Figure C.1 are given by

$$\begin{aligned} \vec{a}_1 &= a_0\vec{i} \\ \vec{a}_2 &= -\tfrac{a_0}{2}\vec{i} + \tfrac{\sqrt{3}a_0}{2}\vec{j} \\ \vec{a}_3 &= c_0\vec{k} \end{aligned} , \tag{C.1}$$

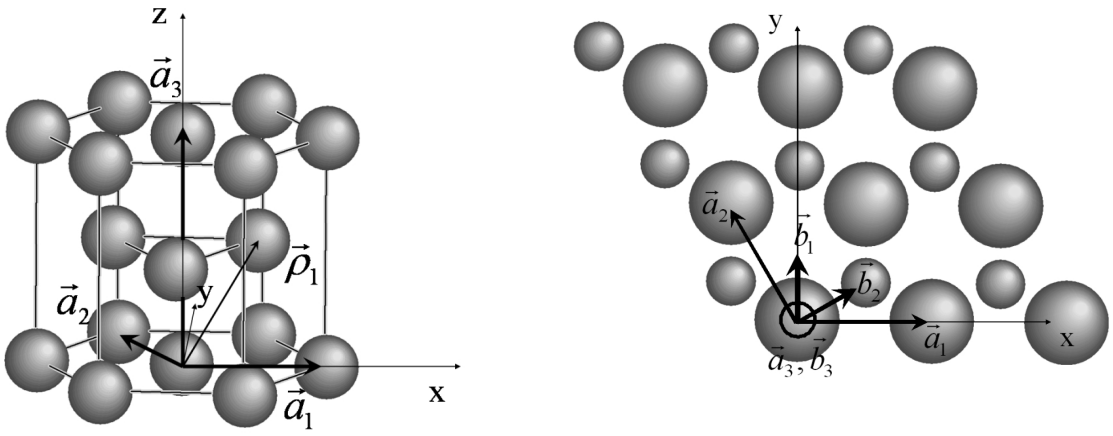

a) b)

Figure C.1: a) Back and b) top views of a unit cell of the hexagonal close-packed lattice.

where $\vec{i}$, $\vec{j}$ and $\vec{k}$ are the normalized basis vectors of the Cartesian coordinate system, a_0 and c_0 lattice parameters.

Each crystal lattice site $\vec{r}$ can be described by two vectors $\vec{R}$ and $\vec{h}_p$ ($\vec{r} = \vec{R} + \vec{h}_p$). Vector $\vec{R} = n_1\vec{a}_1 + n_2\vec{a}_2 + n_3\vec{a}_3$, where n_1, n_2 and n_3 are integers, refers to the unit-cell's origin position; vector $\vec{h}_p$ denotes the distance of a given site with respect to the unit-cell's origin, and p denotes the sublattice. From Figure C.1 one can see that $\vec{h}_0 = \vec{0}$ and $\vec{h}_1 = 2/3\vec{a}_1 + 1/3\vec{a}_2 + 1/2\vec{a}_3$.

The indexation of planes and directions, and also the analysis of diffraction data of crystals is performed using the concept of reciprocal space. The reciprocal basis vectors, $\{\vec{b}_i\}$, are related to the direct basis vectors through the equations of type

$$\vec{b}_i = \frac{\vec{a}_j \times \vec{a}_k}{\vec{a}_i \cdot (\vec{a}_j \times \vec{a}_k)}. \tag{C.2}$$

Using the definition given by Eq. C.2 one can find the Cartesian coordinates of reciprocal basis vectors shown in Figure C.1:

$$\begin{aligned} \vec{b}_1 &= -\tfrac{1}{a_0}\vec{i} + \tfrac{1}{a_0\sqrt{3}}\vec{j} \\ \vec{b}_2 &= \tfrac{1}{a_0}\vec{j} \\ \vec{b}_3 &= \tfrac{1}{c_0}\vec{k} \end{aligned} \quad . \tag{C.3}$$

It is worth to mention, that in the literature planes lie perpendicular to the six-fold symmetry axis are called *basal planes*, in contrast to the planes which lying parallel to this axis and are called *prismatic planes*. In Figure C.2 the most important prismatic planes and some crystallographic

directions in an *hcp*-lattice are shown.

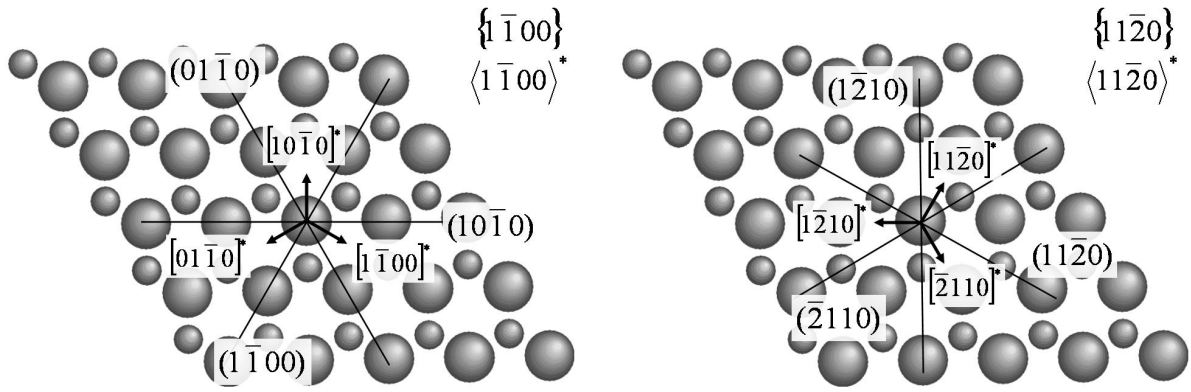

a) b)

Figure C.2: Prismatic planes of the *hcp*-lattice. The basal plane is parallel to the plane of the figure.

D Crystallography of $D0_{19}$ structure

Let us consider an ordered A_3B lattice, which is the $D0_{19}$-type structure — ordered distribution of A and B atoms at the *hcp*-lattice sites.

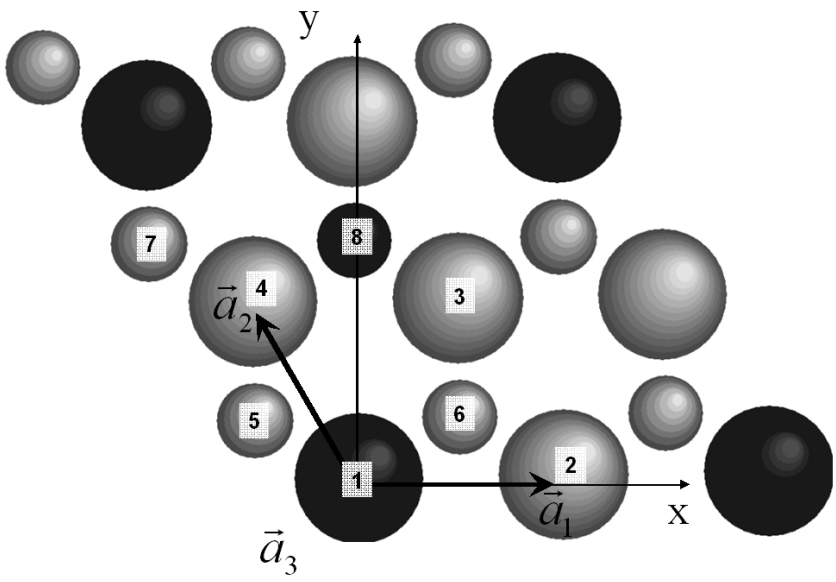

Figure D.1: Top view of two basal planes of an ordered $D0_{19}$ structure. Numbers denote the atoms of an elementary cell of the structure. A atoms are presented in gray, B-atoms are black.

An elementary cell of an ordered $D0_{19}$ alloy consist of four *hcp* cells that is of eight atoms at

the following positions given in hexagonal coordinate system (see Figure D.1):

$$\begin{array}{ll} (\mathbf{B})\ \vec{A}_1(0,0,0) & (\mathbf{A})\ \vec{A}_2(1,0,0) \\ (\mathbf{A})\ \vec{A}_3(0,1,0) & (\mathbf{A})\ \vec{A}_4(1,1,0) \\ (\mathbf{A})\ \vec{A}_5(-1/3,1/3,1/2) & (\mathbf{A})\ \vec{A}_6(2/3,1/3,1/2) \\ (\mathbf{A})\ \vec{A}_7(-1/3,4/3,1/2) & (\mathbf{B})\ \vec{A}_8(2/3,4/3,1/2) \end{array} . \tag{D.1}$$

These 8 atoms are marked in Figure D.1 by numbers. Any site of the $D0_{19}$ structure may be described by a reference vector:

$$\vec{r} = \vec{A}_i + 2n_1\vec{a}_1 + 2n_2\vec{a}_2 + n_3\vec{a}_3,$$

where $\vec{a}_i$ are the basis vectors of the parent *hcp*-lattice.

It exists four translation variants of the $D0_{19}$ cell, which can be generated by performing translation of the presented elementary cell (Figure D.1) by vectors $\vec{a}_1$, $\vec{a}_2$ or $\vec{a}_1 + \vec{a}_2$.

The $D0_{19}$-type structure (see Figure D.1) is generated by the rays of superlattice wave-vector $\vec{k}^M$ [Rad08]: $\vec{k}^1_M = (1/2, 0, 0)$, $\vec{k}^2_M = (0, 1/2, 0)$, $\vec{k}^3_M = (1/2, 1/2, 0)$. Hence, the single-site occupation-probability function, $n_q(\vec{R})$, of the stoichiometric perfectly-ordered DO_{19}-type superstructure can be presented as follows:

$$\begin{pmatrix} n_1(\vec{R}) \\ n_2(\vec{R}) \end{pmatrix} = \frac{1}{4} + \frac{1}{4}\left[\xi_1 \begin{pmatrix} 1 \\ 1 \end{pmatrix} e^{i\pi\vec{b}_1\cdot\vec{R}} + \xi_2 \begin{pmatrix} 1 \\ -1 \end{pmatrix} e^{i\pi\vec{b}_2\cdot\vec{R}} + \xi_3 \begin{pmatrix} 1 \\ -1 \end{pmatrix} e^{i\pi(\vec{b}_1+\vec{b}_2)\cdot\vec{R}}\right], \tag{D.2}$$

where $\xi_1 = \xi_2 = \xi_3 = 1$, $\xi_1 = -\xi_2 = -\xi_3 = 1$, $-\xi_1 = \xi_2 = -\xi_3 = 1$ and $-\xi_1 = -\xi_2 = \xi_2 = 1$. Every set of $\{\xi_i\}$ corresponds to a one of the four translation variants of the ordered structure. Function D.2 assumes two values, 0 and 1, which correspond to A and B atoms on the lattice site, respectively.

Then, the Fourier transform of a system which contains $D0_{19}$-type ordered domains should give on the diffraction map in addition to the fundamental peaks (formed by the reflections from planes of the parent *hcp*-lattice) also the superstructure peaks in the points corresponding to the reciprocal vectors $\{\vec{k}_M\}$ (see Figure D.2).

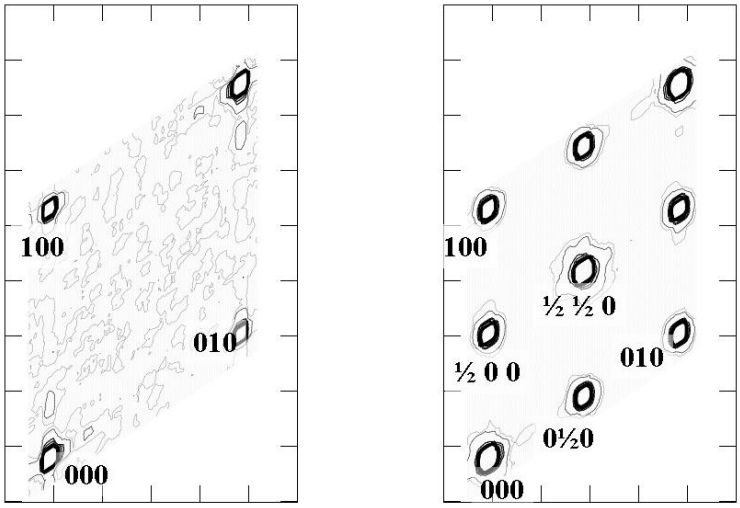

Figure D.2: Diffraction maps obtained by the Fourier transform of the a) disordered *hcp*-binary alloy; b) *hcp*-binary alloy with $D0_{19}$ order.

The intensities of superstructure peaks in case of perfectly ordered $D0_{19}$ structure can be expressed by the equation:

$$I(\vec{k}_M) = N_{e.s.} \left| Y(\vec{k}_M) \right|,$$

where $N_{e.s.}$ is the number of $D0_{19}$-elementary cells and $Y(\vec{k}_M)$ is the structure amplitude of one elementary cell given by

$$Y(\vec{k}_M) = \sum_{\alpha} f_\alpha e^{-i2\pi \vec{k}_M \vec{r}_\alpha}, \tag{D.3}$$

where α denotes the summation over 8 atoms of an elementary $D0_{19}$ cell and f_α is the atomic factor of an atom in the position $\vec{r}_\alpha$. It is easy to show, using the atomic positions with corresponding types of atoms given by Eqs.D.1, that

$$\begin{aligned} I(\vec{k}_M^{1,2}) &= 4(f_B - f_A)^2 N_{e.s.} \\ I(\vec{k}_M^{3}) &= (f_B - f_A)^2 N_{e.s.} \end{aligned},$$

where f_A and f_B are the atomic factors of A and B atoms, respectively. If one puts $f_A = 0$ and $f_B = 1$, then $I(\vec{k}_M^3)/I(\vec{k}_M^{1,2}) = 4$.

References

Rad08. T. Radchenko, V. Tatarenko, H. Zapolsky, D. Blavette, *Journal of Alloys and Compounds*, **452**(1):122 (2008), proceedings of the 12th International IUPAC Conference on High Temperature Materials Chemistry-HTMC XII.